INSTITUTO POTOSINO DE INVESTIGACIÓN CIENTÍFICA Y TECNOLÓGICA, A.C.

POSGRADO EN NANOCIENCIAS Y MATERIALES

Kinetic study of Polydopamine synthesis and its use as a photocatalyst

Tesis que presenta

Juan Carlos García Mayorga

Para obtener el grado de
Doctor en Nanociencias y Materiales

Directores de la Tesis:

Dr. Vladimir Alonso Escobar Barrios

Dr. Haret-Codratian Rosu Barbus

San Luis Potosí, S.L.P., abril de 2023

IPICYT

Constancia de aprobación de la tesis

La tesis "**(Nombre completo de la tesis)**" presentada para obtener el Grado de Doctor(a) en Nanociencias y Materiales fue elaborada por **(Nombre completo del candidato)** y aprobada el **día de mm de año** por los suscritos, designados por el Colegio de Profesores de la División de Materiales Avanzados del Instituto Potosino de Investigación Científica y Tecnológica, A.C.

Dr. Vladimir Alonso Escobar Barrios

Dr. Haret-Codratian Rosu Barbus

Director/Codirectores de la tesis

Dra. Alma Berenice Jasso Salcedo

Miembro del Comité Tutoral

Dr. Vicente Rodríguez González

Miembro del Comité Tutoral

Créditos Institucionales

Esta tesis fue elaborada en el Laboratorio de Polímeros de la División de Materiales Avanzados del Instituto Potosino de Investigación Científica y Tecnológica, A.C., bajo la dirección de Dr. Vladimir Alonso Escobar Barrios y Dr. Haret-Codratian Rosu Barbus.

Durante la realización del trabajo el autor recibió una beca académica del Consejo Nacional de Ciencia y Tecnología (686618) y del Instituto Potosino de Investigación Científica y Tecnológica, A. C.

Agradecimientos

Después de cuatro años y ocho meses mis esfuerzos quedan materializados en este trabajo el cual representa en conjunto mi crecimiento profesional y personal; para lograrlo me he valido, con plena conciencia, de muchas personas y, sin saberlo, de muchas otras. A todas las instituciones y particulares que me ayudaron durante este proceso, aquí mi agradecimiento global. Por otro lado, dos de ellas fueron muy importantes para mí, María Isabel Mayorga Gómez y Vladimir Alonso Escobar Barrios, mi madre y mi asesor. Estoy profundamente agradecido con ustedes. De ninguna manera les cabe culpa alguna por lo que haya de erróneo, de ingenuo o de deforme en las páginas de esta obra, pero sin su ayuda e influencia poco de lo bueno se encontraría en ella.

CONTENTS

TABLES INDEX

FIGURES INDEX

RESUMEN

El estudio de la síntesis y caracterización de polidopamina (PDA) usando dopamina (DA) como monómero e (hidroximetil)aminometano (TRIS) como amortiguador se realizó en esta tesis doctoral. El efecto de la temperatura y la concentración de TRIS en la cinética de polimerización de la DA fueron evaluados; de tal forma que, los parámetros cinéticos fueron calculados para las concentraciones y temperaturas exploradas. Las reacciones llevadas a cabo con 1.5 *mmol* de TRIS exhibieron un incremento sostenido en la constante de velocidad en función de la temperatura. Por ejemplo, la constante de velocidad incrementó de 2.38E-04 a 5.10E-04 cuando la temperatura pasó de 25 a 55 °C; aunque no todas las reacciones siguieron este comportamiento tipo Arrhenius. Además, se estableció la correlación entre las condiciones de síntesis con la morfología, estructura, propiedades térmicas y actividad fotocatalítica de la PDA. Así, la morfología de las partículas de PDA, hacia esferas definidas a mayores temperaturas y concentraciones de TRIS; en tanto que el diámetro y distribución de tamaños se redujeron con el incremento de la temperatura y concentración de TRIS. Por otro lado, a diferencia de lo reportado mayormente en la literatura, la PDA sintetizada mostró una transición endotérmica alrededor de los 130 °C la cual fue asociada con la fusión de zonas regulares en la PDA; la cual corresponde a una estructura de tipo grafítica que fue corroborada por los resultados de espectroscopía infrarroja, Raman y Difracción de Rayos X (XRD). Finalmente, la PDA mostró capacidad de absorción (60% de la concentración inicial) de Rodamina B, que se utilizó como contaminante modelo y cierta capacidad fotocatalítica hacia dicho contaminante. Alcanzando hasta el 15 % de fotodegradación.

ABSTRACT

The study of synthesis and characterization of polydopamine (PDA) using dopamine (DA) as the monomer and (hydroxymethyl)aminomethane (TRIS) as the buffer was carried out during this doctoral thesis. The effect of temperature and TRIS concentration on the kinetics of dopamine polymerization was evaluated. Thus, the kinetic parameters were also calculated based on the explored temperature and concentrations. The reactions with 1.5 *mmol* of TRIS showed a sustained increment of the rate constant with temperature. For instance, the rate increased from 2.38E-04 to 5.10E-04 when the temperature increased from 25 to 55°C, although not all reactions followed this Arrhenius behavior. In addition, the correlation between the synthesis parameters and morphological, structural, thermal properties, and photocatalytic activity of polydopamine was established. Thus, the morphology of the PDA particles changed towards well-defined spheres at higher temperatures and TRIS concentrations. At the same time, the diameter and size distribution were reduced with the increase in temperature and TRIS concentration. On the other hand, unlike what is mostly reported in the literature, the synthesized PDA showed an endothermic transition around 130 °C associated with the melting of the PDA's regular structure, which corresponds to the graphitic-like structure, and that was corroborated by infrared and Raman spectroscopy and X-Ray Diffraction (XRD). Finally, the PDA showed absorption capacity (60% of the initial concentration) of using Rhodamine B as a model pollutant and some photocatalytic capacity towards said contaminant, reaching up to 15 % of photodegradation.

INTRODUCTION

In recent years, the necessity of materials that allow either efficient use of existing energy sources or alternative energies has become a relevant topic and an imperative and inescapable requisite if we want a prosperous and competitive future. In the same way, the objectives proposed by the United Nations (UN) organization to reach in the next 15 years since 2015 in sustainable development and the 64/292 resolution, it is a priority to concentrate all our efforts as the scientific community to warranty the human right to fresh water and its sanitation [1], [2]. The excessive growth of the industry has not only brought us benefits reflected in our daily lives, but it has also represented a terrible environmental impact that has affected the health of all living beings. The primary source of contamination of the aquifer bodies is due to the direct discharge of industrial wastes that contaminate the water due to the presence of pharmaceutical compounds, pesticides, herbicides, textile dyes, resins, and phenolic compounds [3], [4].

The scientific community has used different techniques and processes for proper sanitation, among which the so-called advanced oxidation processes (AOP) stand out. AOPs are efficient methods based on the *in situ* generations of transient oxidizing species (radicals $OH^{\cdot}$) that allow or accelerate degradation or mineralization (total conversion of organic matter into CO_2, H_2O and acidic minerals) from a wide range of organic and/or inorganic substances whose characteristics make them resistant to conventional cleaning treatments [5]. Photocatalysis, one of the AOPs with advantages such as low cost and attractive efficiency, has quickly become an attractive alternative and, consequently, has gained increasing attention from researchers. Photocatalysis is a process through which an electron-hole pair (e^-_{CB} / h^+_{VB}) is generated from the exposure of a photocatalyst to light; this allows altering the speed of the reactions that take place for the generation of oxidizing species such as $OH^{\cdot}$ [6]. Photocatalysts are essentially semiconductors that can be inorganic, such as TiO_2, ZnO, SnO_2, CeO_2, $BiOCl$ [7]–[10] or organic semiconductors with structures such as anthracene, triphenylpyrrolidone, or perylene. There are considerable differences between organic and inorganic semiconductors.

Nevertheless, one of the most relevant is the easy processability for obtaining inorganic semiconductors.

Melanin is a polyphenolic material widely found in all living organisms, from bacteria to mammals. Melanin is found in animals' skin, hair, feathers, scales, and some neural tissues, like the cochlea, retina, and the midbrain nucleus known as *substantia nigra* [11], [12]. There are two main types of melanin, the black or brown insoluble eumelanin, found in human black hair and retina; such eumelanin contains nitrogen and has a high molecular weight compared with pheomelanin, a different kind, which contains sulfur in its structure [12]. Eumelanin has a vital function in providing pigmentation and protecting the skin from phototoxic events due to sunlight irradiance. Melanin has antioxidant and free-radical scavenging behavior, broadband UV-visible absorption, photosensitization, metal ion chelation, and antimicrobial activity [13]. These features make it very interesting to study the possibility of using melanin as an active material for technological applications, such as molecular electronics and photovoltaic devices, since it is considered an organic semiconductor [14]. In recent years, the synthetic melanin denominated as polydopamine (PDA) has acquired much attention in the field of biomedicine [15], electronics [16], bioelectronics [17], environmental remediation [18], and photocatalysis [19]. One of its most remarkable applications is in the remediation of contaminated water, where PDA is used as part of a photocatalyst to increase its photoactivity [19]–[21]; at the same time, it has been used for hydrogen generation [22], removal of herbicides [23], surface modification due to its excellent adhesion properties at almost all surfaces [24], [25], sensors for colorimetry or glucose [26], [27], photothermal therapy to treat cancer [28], and for drug encapsulation and release [29]–[32]. The synthesis and processing versatility of PDA allows for achieving a diverse variety of shapes ranging from hollow or solid spheres or core-shell particles to thin films. It can even be used to decorate other particles [17], [33]. Additionally, thermodynamic and kinetic PDA synthesis studies are critical to establishing parameters like reaction order *(n)*, pre-exponential factor *(A)*, and activation energy *(E_a)*. Such parameters are essential for polymerization control, affecting the material's final properties, and are critical to the technological use of the PDA. In this context, M. Salomäki *et al.* [34] did a thermodynamic study of dopamine oxidation and cyclization dependence on pH and oxidants like transition-metal ions, mainly focused on the early stages of the process. The authors proposed a general mechanism to understand the involved species during PDA polymerization and concluded that the most critical parameter for the process is the *pK* value. In the same way, the use of tuning radicals to control the size of PDA nanoparticles is reported by X. Wang *et al.* [35]. In the latter study, the authors concluded that the polymerization could be inhibited or terminated from the free radical scavengers, while the stable radicals catalyzed the formation of PDA seeds. A comparable study was carried out by M. Wu *et al.* [36], who synthesized PDA through sodium hydroxide and developed a model about relationships between particle size, the molar ratio of DA, and oxidizing agent to control the particle diameter and distribution.

In summary, controlling the PDA polymerization reaction is essential since it controls its yield, particle size, and properties like photothermal effect, UV protection, Band Gap, and free radical scavenging activity [36], [37]. So far, the studies regarding the kinetics of PDA synthesis are few. Usually, the polymerization of DA with different buffers or bases like sodium hydroxide [38], sodium bicarbonate [39], ammonia [40], and phosphate solution [41] is reported, but other relevant kinetics parameters like n, A, and E_a are not provided. In this work, the aforementioned kinetic parameters are determined, their relationship with the structure and properties of PDA is established, and in the same way, its influence in the photocatalytic activity for removal of rhodamine B from water.

CHAPTER I: BACKGROUND

1.1 Water

In 2010 the UN recognized the right to freshwater and water sanitation as an essential human right for the enjoyment of life and other human rights [2]. The right to potable and healthy water access means water free of microorganisms, chemical substances, and radiological hazards that constitute a health risk [42].

Water is a determinate factor in economic, political, and social human development; contaminated water is a latent threat to the population and further challenges enterprises or governments [43]. The Earth's water is almost 1, 386, 000, 000 km^3 corresponding to oceans, glaciers, rivers, lakes, and aquifers; from this quantity, only 0.0072 % is freshwater, and it is available to humans (mainly rivers) [44]. Water is the universal solvent; for such abuse, water receives sewage from hospitals, municipal wastewater (52.7 %), and even chemical, biological, and industrial effluents (not municipal wastewater 32 %) [45].

In 2016, Mexico extracted from the environment almost 21 659 km^3 of water to carry out different services, economic activities, and supply to the population; from these, returned to the environment 6 103 km^3 (28 %), of which 2 387.7 km^3 (39 %) returned as untreated wastewater, 629 km^3 as (10 %) treated wastewater, and 3 086.6 km^3 (51 %) as losses [46]. According to civic groups and CONAGUA, at least 70 % of the freshwater bodies are contaminated. One of the main problems is that wastewater is poured into the water bodies without any previous treatment [43], [47].

In concordance to "Fondo para la Comunicación y la Educación Ambiental A.C.," in 2015, the economic cost caused by not treated wastewater was 57.4 billion pesos, which is equivalent to 0.3 % of the gross domestic product. The projections for 2030 indicate that there will be 9.2 billion cubic meters of wastewater; the demand could be reduced by 40 % if the wastewater is treated and reused [42].

The "grade of pressure" is the percentage that represents the water used concerning the extractable water. It could be very high (90-100 %), high (40-90 %), medium (20-40 %), low (10-20 %), and without interest(<10%). In Mexico, in 2017, it had a low-pressure grade (19.5 %). On the other hand, San Luis Potosí had a percentage of 18.6 % in the same year, and estimations for 2030 indicate that it will be almost 23.4 %, passing from low to medium pressure grade. The metropolitan zones of San Luis Potosí state, in 2017, used 35.8 km^3 of freshwater, which is equivalent to 17.8% of all the water withdrawn from the environment, and in consideration with the national estimation, 39 % (35 800 billion liters) of this water returns to natural sources without any treatment [46].

1.1.1 Water pollution

Currently, almost 8 000 billion people live on the Earth, of which 2 100 million (3 out of 10) do not have access to a water supply, and 844 million with no access to essential drinking water services [48]. According to the Pacific Institute, 2 million tons of industrial and agricultural waste and sewage are generated daily. The United Nations estimate that the amount of wastewater produced annually is around 1 500 km^3, which is six times higher than all the water in the rivers of the Earth [49]. The 80% of whole water used in homes, cities, and industries is returned to the environment (lakes, rivers, and oceans) without any treatment, being this the main cause of contamination of freshwater bodies [50]. At the same time, pollution is associated with the transmission of diseases such as diarrhea, cholera, dysentery, hepatitis A, and typhoid fever. These diseases are responsible for the death of 842 000 persons annually by unhealthy water or insufficient sanitation [48].

The most common areas of water pollution are:

- Agricultural

The agriculture sector represents a 70 % consumption of all water extract from the environment, making it the most polluting freshwater sector as revealed by the Food and Agriculture Organization of the United Nations, which reports that farms are unloading huge quantities of agrochemicals, nutrients, pesticides, salts, sediments, organic carbon, pathogens, and metals as a direct product of irrigation activities. In the same way, there is contamination by livestock feed and veterinary medicines such as antibiotics and growth promotors (hormones). The return of wastewater without any treatment to water bodies negatively impacts human health. For instance, the well-known blue-baby syndrome in which high levels of nitrates in water can cause methemoglobinemia—a potentially fatal illness—in infants [51].

- Sewage and wastewater

After various uses have fouled the community's water supply, it becomes sewage/wastewater; wastewater can be defined as a combination of the water (or liquid) carrying wastes removed from residences, institutions, commercial and industrial establishments, together with such groundwater, and as may be present in surface water and stormwater. It comprises 99.9 % water and 0.1 % solids; carbon compounds such as human waste, vegetable matter, and paper are examples of solids. Nevertheless, pollution by solids is not the main problem for humans and wildlife; just like population growth, so makes the demand for products and medicines and this demand increases the presence of trace organic contaminants such as pharmaceutical and personal care products (PPCPs) that are now widely considered as emerging threats to aquatic animals and ecosystem health [52]. In comparison, organic matter solids represent a risk to the environment by consuming dissolved oxygen (biochemical oxygen demand), which can cause kills and other undesirable effects. The dissolved compounds in water (PPCPs), such as paracetamol, ibuprofen, triclosan, and drugs such as methamphetamine and amphetamine, can also be a potential risk for the environment from their natural action as endocrine disruptors and psychostimulants [53].

- Oil pollution

Although oil spills are considered one of the main causes of water contamination, the reality is a little different; consumers denote the great majority of oil pollution in our seas, including oil and gasoline that drips from millions of cars and trucks every day. Furthermore, almost half of the estimated 1 million tons of oil that makes its way into marine environments yearly comes not from tanker spills but from land-based sources such as factories, farms, and cities. At sea, tanker spills account for 10 percent of the oil in waters around the world, while regular shipping industry operations, through both legal and illegal discharges, contribute about one-third [54].

1.2 Water treatment

Wastewater purification and recycling are essential to ensure our survival, the world, and its wildlife; the scientific community ensures that new technologies solve the problem at a low cost and environmental burden [10]. Physical, chemical, and biological processes have been used for wastewater treatment.

The significant environmental aspect is removing dyestuffs and other organic compounds from the wastewater manufacturing industry. Nonetheless, the conventional biological treatment processes are unsuccessful due to synthetic dyes' recalcitrant character and sewage's high salinity. Otherwise, traditional physical techniques like adsorption on activation carbon, coagulation by chemical agents, ultrafiltration reverse osmosis, and ion exchange on synthetic adsorbent resins are used to remove dye pollutants in water. Nonetheless, these methods successfully transfer organic compounds from water to another phase, which implies further treatments of solid wastes, as well as the regeneration of the adsorbent. It increases the process cost.

Some of the essential factors to consider in wastewater treatment technologies, according to reference [10], are:

- Treatment flexibility.
- Mineralization of parent and intermediate contaminants.
- The final efficiency of wastewater treatment.
- Recycling capacity and potential use of treated water, and
- Cost-effectiveness and eco-friendliness.

Advanced Oxidation Process (AOP, **Figure 1**) turns up as one of the most confidential technologies due to its capacity to complete the oxidation of organic compounds to harmless products such as CO_2 and H_2O, which attracted substantial attention that basic and technological research has focused on it [10]. Since the 1980s, AOPs have been used in wastewater treatment for the degradation of specific pollutants, reduction of organic content, treatment of sludge, and removal of color and odor. The performance of AOPs depends on the generation and utilization of reactive species such as $(OH^\bullet)$. A high reduction potential and rate constant in the order of $10^6 – 10^9$ $M^{-1}s^{-1}$ allows AOPs to degrade most of the organic compounds, including carbon dioxide. Various AOPs have been invented and studied and can be classified mainly into four kinds concerning $OH^\bullet$ radicals' production [55].

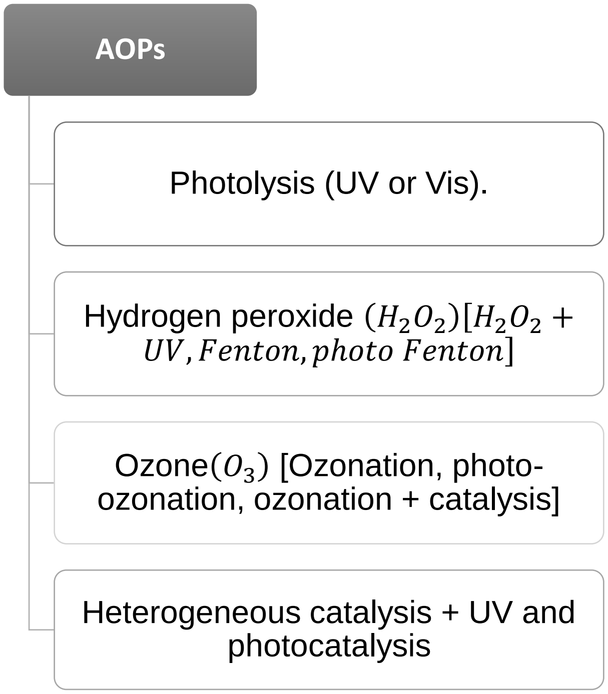

Figure 1. Different Advanced Oxidation Processes [55].

1.2.1 Photocatalysis

According to the authors, R. Saravana et *al.,* the word "photocatalysis" is derived from Greek and is constituted of two parts: 1 - the prefix photo means light, and 2 – catalysis, which means loosen or untie. It describes the process where a substance involves changing the rate of a chemical transformation of a substance without being changed. In general, photocatalysis can be defined as *"a change in the rate of chemical reactions or their generation under the action of light in the presence of substances called photocatalysts that absorb light quanta and is involved in the chemical transformation of the reactants."* [56].

In the same way, R. Saravana et *al.* indicates that two kinds of photocatalysis exist: homo- and heterogeneous processes. Homogeneous photocatalysis mainly uses metal complexes as catalysts (iron, copper, chromium, and vanadium are some of the most transition metal complexes used). The higher oxidation state of metal ion complexes generated hydroxyl radicals under the photon or thermal condition. Consequently, the destruction of organic matter in water is carried out by these hydroxyl radicals. On the other hand, heterogeneous photocatalysis is a method that can be used to degrade various organic pollutants in wastewater. The primary photocatalyst materials include metallic oxides (TiO_2, ZnO, SnO_2, and CeO_2). This process has several advantages over the competing process: complete mineralization, no waste disposal problem, low cost, and the necessity of mild temperature and pressure conditions only. The use of semiconductors in heterogeneous photocatalysis is due to their electronic structure, characterized by a filled valence band (*VB*) and an empty conduction band (*CB*), properties of light absorption, and lifetime excites states. An excellent semiconductor should have 1. Photoactive, 2. Able to utilize visible or near-UV light, 3. Biologically and chemically inert, 4. Photostable (stability toward photo corrosion), 5. Inexpensive, and 6. Nontoxic to be used as a photocatalyst [10].

Photocatalysis mainly involves three steps:

1. Light absorption and photogeneration of e^-_{CB} / h^+_{VB} pairs.
2. Separation of charge carriers.
3. Oxidation and reduction reactions on the surface of the semiconductor.

TiO_2 under UV light is one of the most common photocatalysts in heterogeneous photocatalysis (**Figure 2**). It is based on the adsorption of photons with energy higher than 3.2 *eV* (wavelengths lower than 390 nm) that cause the excitation of electrons on TiO_2 and originate charge separation events. When a semiconductor is irradiated with an energy higher than its bandgap energy, the generation of excited high-energy states of e^-_{CB} / h^+_{VB} pairs occurs; it implies the promotion of an electron in the *CB*, e^-_{CB}, and the formation of a positive hole in the valence band, h^+_{VB} (**Equation 1**)

The h^+_{VB} reacts with organic compounds resulting in their oxidation, producing CO_2 and H_2O as end products (**Equation 2**). The oxidation of organic compounds also can be carried out by the reaction of h^+_{VB} with water to generate hydroxyl radicals ($OH^\bullet$) (**Equation 3**). These $OH^\bullet$ have the second-highest oxidation potential of 2.80 V, slightly lower than the strongest oxidant-fluorine. Due to its electrophilic nature (electron preferring), the $OH^\cdot$ can non-selectively oxidize almost all electron-rich organic molecules, eventually converting them into CO_2 and water (**Equation 4**).

The reaction of dissolved O_2 with the conductive band can form radical anion superoxide, as shown in **Equation 5**. The further reaction can lead to the formation of hydrogen peroxide, which leads to the formation of $OH^\bullet$ [57].

$$TiO_2 + hv(< 387\ nm) \rightarrow e^-_{(CB)} + h^+_{(VB)} \tag{1}$$

$$h^+_{(VB)} + R \rightarrow intermediates \rightarrow CO_2 + H_2O \tag{2}$$

$$h^+_{(VB)} + H_2O \rightarrow OH^\bullet + H^+ \tag{3}$$

$$OH^\bullet + R \rightarrow intermediates \rightarrow CO_2 + H_2O \tag{4}$$

$$e^-_{(CB)} + O_2 \rightarrow O_2^{\bullet -} \tag{5}$$

R represents the organic compound (pollutant).

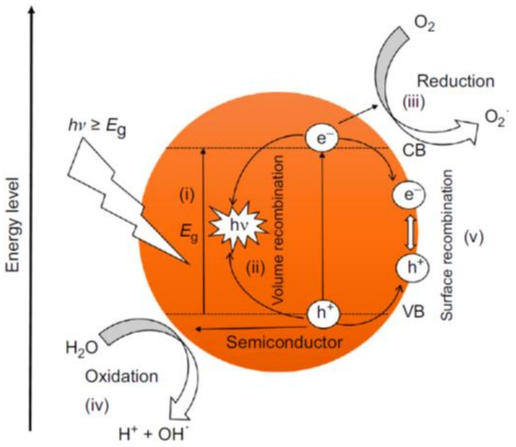

Figure 2. Schematic photocatalytic mechanism representation of semiconductor ($e^-_{(CB)}$ / $h^+_{(VB)}$ pair formation) [55].

The parameters that primarily affect the mineralization rate of an organic compound by photocatalysis method, according to R. Saravana et *al.* are "structure, shape, size, the surface area of the catalyst, reaction temperature, pH, light intensity, amount of catalyst, and concentration of wastewater" [10].

1.2.2 Photocatalytic materials

There are a few basic material requirements for developing high-quality heterogeneous photocatalysts. According to the description in which the generation of several charge carriers depends on the amount of light absorption by the material, the first and most important is the bandgap energy of the semiconductor. It is known that around 42% of the total solar spectrum is visible light; in other words, the visible spectra have an energy range from 2.4 to 3.2 *eV*. If the whole spectrum is captured without scattering, photocatalysts provide desirable energy for different purposes. Then, it is essential to design a semiconductor with bandgap energy in the visible region of the solar spectrum since materials with a band gap located in the UV region are less suitable for photodegradation than those of visible bandgap semiconductors.

The maximum absorption by the semiconductor can be calculated using **Equation 6**.

$$\alpha = \frac{A(hv - E_g)^n}{hv} \qquad \textbf{6}$$

Where A is constant; $n = ½$ for a direct bandgap semiconductor, $n = 2$ for an indirect bandgap semiconductor, and α is the absorption coefficient (α should be equal to 1 for the highest efficiency calculation, neglecting all kinds of losses). Hypothetical efficiency (η_{hyp}) could be calculated by **Equation 7**.

$$\eta_{hyp} = \frac{E_g \int_{E_g}^{\infty} N(E) \cdot dE}{\int_0^{\infty} E \cdot N(E) \cdot dE} \qquad \textbf{7}$$

If we calculate the total hypothetical efficiency, then it would be ~ 47 % at $E_g = 1.2$ *eV*. From this point of view, the bandgap of semiconductors should be between 1.4 and 1.6 *eV* for efficient photocatalysts.

The position of *VB* and *CB* is the second important parameter. The position of *VB* should be set under the oxygen oxidation potential, and *CB* should be set above the hydrogen reduction potential; consequently, water will take place at 1.23 *eV*, and most of the toxic chemicals are dissolved in water. Hence, to produce a large number of oxidant species, the band position of semiconductors should be higher than the energy required for water splitting (**Figure 3**) [55].

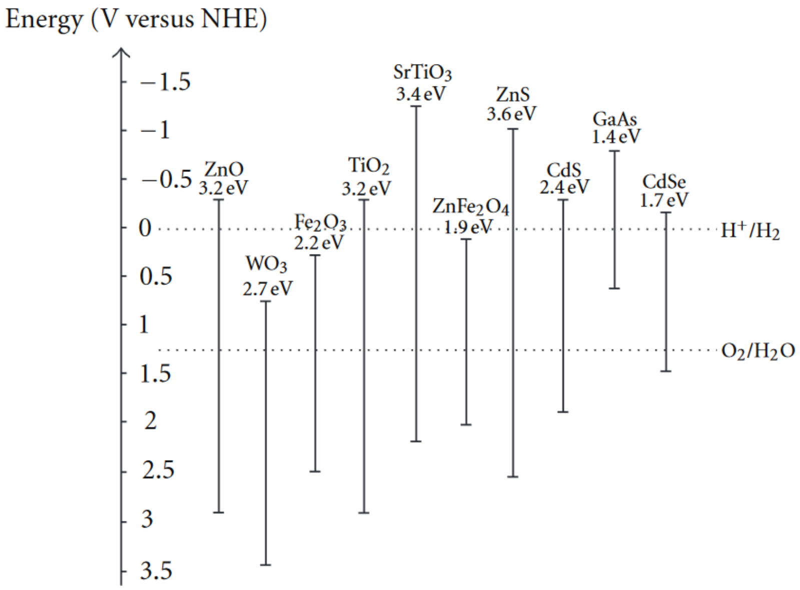

Figure 3. VB and CB positions for several semiconductors in an aqueous media (*pH = 1*) [58].

Intrinsic generation and separation of charge carriers is the third material requirement. This process is necessary for the electrons to be transferred onto the surface of the semiconductor through the diffusion process and takes part in redox reactions to generate oxidant species. The generation of carriers through the diffusion process could be calculated using **Equation 8**.

$$\eta_q = \frac{J}{e \cdot \varphi_0}\left[1 - \frac{e^{(-\alpha W)}}{1+\alpha \cdot L_p}\right] \qquad \mathbf{8}$$

L_p is the diffusion length of the minority carrier, W is the depletion layer width, φ_0 the photon flux, and η_q is the quantum efficiency. The presence of grain boundaries and surface states on the semiconductor is the fourth material requirement. Generation of e^-_{CB} / h^+_{VB} pairs and their reaction with the species of pollutants is essential. Nevertheless, poor photocatalytic performance is due to a low work function of the semiconductor's reversible reaction that losses many carriers. Therefore, surface states existing on the surface of photocatalysts could trap the charge carriers and improve the lifetime.

The fifth material requirement is stability against photo-corrosion and dissolution. When photogenerated carriers are produced, these could collect on the surface of the semiconductor, which is responsible for the photo-corrosion and dissolution of the photocatalyst. Several semiconductors are unstable under irradiation, even though they are stable in the dark. The last material requirement is a highly specific surface for the adsorption of many pollutant molecules; many sites per volume/mass are allowed with nanostructured materials that encourage the reaction and degradation of pollutants [55].

Metal oxide semiconductors are considered the most suitable photocatalyst due to their photo-corrosion resistance and broad bandgap energies. **Table 1** provides the bandgap energies at the corresponding wavelength for well-known semiconductors. The most used material is TiO_2 due to cost/effectiveness, thermally stable, nontoxic, chemically and biologically inert, and can promote the oxidation of organic compounds. Properties like bandgap energy, surface area, crystal composition, particle size distribution, and porosity influence the photocatalytic activity of any semiconductor, such as TiO_2 [57].

Table 1. Different semiconductors and their bandgaps [57].

Semiconductor	Bandgap / *eV*	Wavelength / *nm*
TiO_2 (rutile)	3.0	413
TiO_2 (anatase)	3.2	388
ZnO	3.2	388
ZnS	3.6	335
CdS	2.4	516
Fe_2O_3	2.3	539

1.2.3 Photocatalysis based on organic semiconductors

Recently, intensive work has been done on the photocatalytic degradation of environmentally hazardous pollutants using metal oxides due to their superior photocatalytic performance, non-toxicity, low production cost, and high persistence to photo-corrosion. Nevertheless, inorganic semiconductors have a moderate bandgap of 1.0 – 3.0 *eV*; in other words, they have inefficient light absorption and limited variability although their high charge-carrier mobility. Different methodologies have been adopted to improve these issues in photocatalytic efficiencies, like doping, photosensitization, crystallization, or heterojunction, which usually involve complicated fabrication processes or harsh conditions. On the other hand, organic semiconductors have the advantages of synthetic modularity, structural diversity, and feasibility for precise tuning of photoelectronic and structural properties. Additionally, organic semiconductors, organic conjugated molecules, are characterized by a delocalized π-electron system, which allows them to build blocks for organized nanoscale superstructures. Structural flexibility, large-area, lightweight, and stretchable or flexible fabrication devices by thermal disposition and simple solution processing are essential characteristics of organic semiconductors [59]. For these reasons, organic semiconductors have regained great relevance in the last years in photocatalysis, mainly in photovoltaic cells.

The possible mechanistic pathways to the degradation of a general pollutant have been described by Marin et al. [59] according to **Equations 9** to **15**. In **Equation 9**, the photocatalyst denoted by a P absorbs light of a specific wavelength and gets to the singlet excited state $^1P^*$. This species can participate in electron-transfer reactions of pollutants (Q), giving rise to the oxidized form of the pollutant ($Q^{\bullet +}$) and the reduced form of the photocatalyst ($P^{\bullet -}$). In **Equations 12** and **13**, $^1P^*$ or the triple-state $^3P^*$ formed by an intersystem crossing (ISC) from $^1P^*$ can react with water to produce hydroxyl radicals $OH^{\bullet}$, as well as the radical anion of the photocatalyst $P^{\bullet -}$. $^3P^*$ can also go through an electron-transfer reaction, affording the formation of $Q^{\bullet +}$ and $P^{\bullet -}$, **Equation 14**. In **Equation 15**, the result of singlet oxygen $^1O_2$ is a product of the response of $^3P^*$ with O_2 by an energy transfer process. P-Q complex can sometimes be formed between the ground state of the photocatalyst and the pollutant. Charge separation occurs in the complex to give $Q^{\bullet +}$ and $P^{\bullet -}$ upon the light irradiation (**Equation 16**). An additional pathway implies the reaction of $P^{\bullet -}$ with molecular oxygen to give superoxide radical anion $O_2^{\bullet -}$ [59].

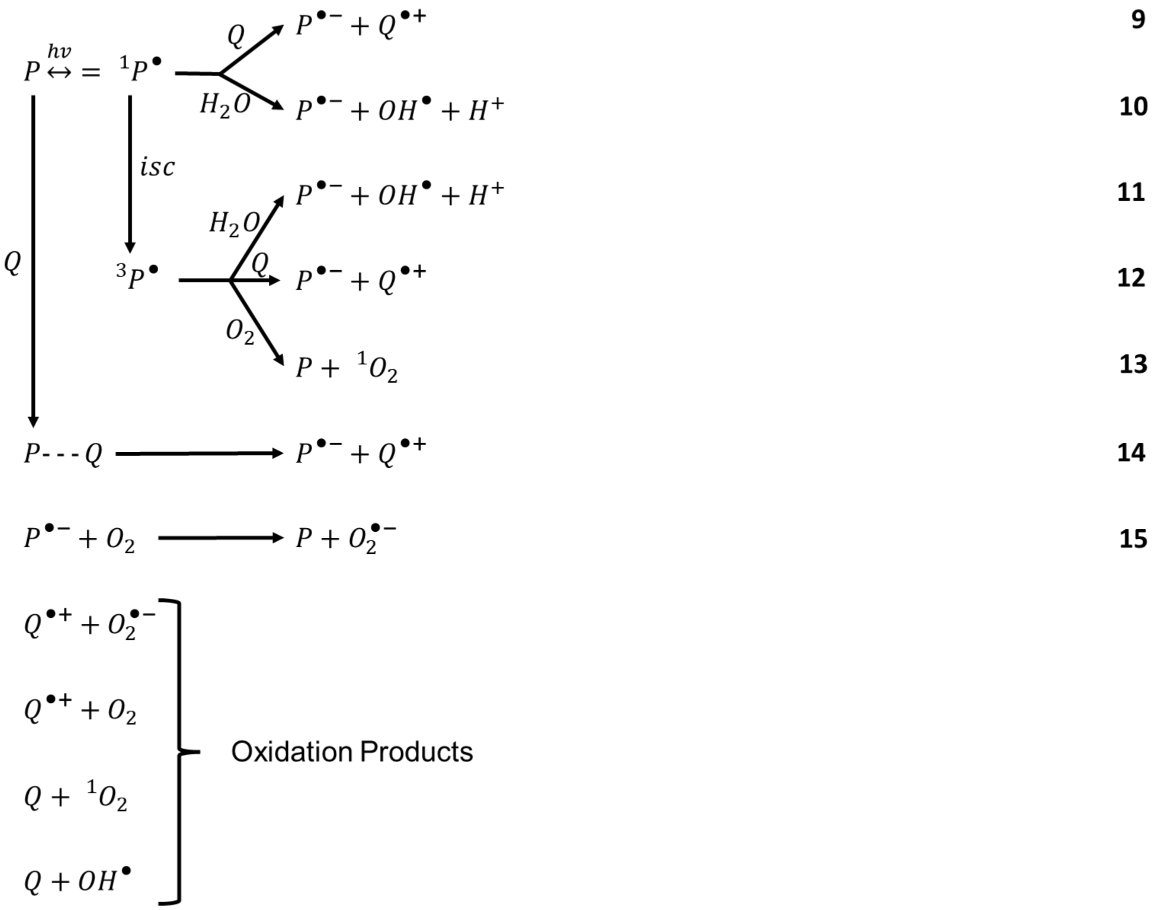

1.3 Eumelanin and polydopamine

In London in 1820, Sir Everard Holmes proposed the hypothesis that melanin is a simple solar filter that only protects us from dangerous ultraviolet rays. To date, the idea is still present, even among dermatologists. However, melanins are pigments with a high molecular weight (biopolymers) and various biological functions; they are found in mammals' skin, hair, eyes, brain, and many internal tissues (e.g., the wide variations in hair coloration in mammals are all the result of the melanin paintbrush [60]). Melanins are synthesized in epidermis melanocytes by tyrosine-catalyzed oxidation of tyrosine [61]. There are two primary forms of melanin; first*, eumelanin* (brown-black pigment) is the predominant form in skin, hair, and eyes. The second, *pheomelanin (yellow-reddish pigment),* contains sulfur in its structure and is synthesized in the presence of cysteine; It is present in red hair and light skin [12], [13]. The technological use of melanin started in 1974 after McGinnes et al. [62]

demonstrated that melanin pellets behave as an electrical switch, which means that this material could act as a disordered organic semiconductor.

On the other hand, polydopamine (PDA), the final oxidation product of dopamine or other catecholamines, is considered like synthetic melanin. Inspired by marine mussel (*Bivalvia Mollusca*) due to its properties of anchoring virtually to all types of material surfaces—even to classically adhesion-resistant polytetrafluoroethylene [63]—, PDA has attracted much attention as a versatile surface modifier. PDA has different functional groups, like catechol, amine, imine, and even carboxylic acid, which lend it control surface properties for various applications as sensors for H_2O_2 [27], glucose [64], or colorimetric detections [26] drug encapsulation and delivery [29]–[32], hydrogen generation [22], environmental remediation [19]–[21], organic solar cells [65], [66], and engineering tissues [67]–[69].

The interest and discovery of new applications for these materials have steadily increased in recent years. It derives from its physical-chemical properties as broadband *UV-Vis* light absorption [13], mixed electronic-ionic conductivity [70], [71], and free radical scavenger [72] in addition to its biodegradability and biocompatibility [73], [74].

1.3.1 Eumelanin synthesis and structure

Figure 4. shows the diagram of the eumelanin synthesis carried out in melanocytes (obtained from reference [75]). On the top, tyrosine is oxidized by tyrosinase (T) in the presence of oxygen, which generates dopaquinone (DQ) as an intermediate product. After that, intramolecular addition of the amino group produces the leucodopachrome specie (or cyclodopa, DAL) that consequently gives rise to dopachrome (DC)—and (3,4-Dihydroxyphenilalanine; DOPA)—due to redox exchange between DAL and DQ. Subsequently, 5,6-Dihydroxyndole (DHI) or 5,6-Dihydroxyndole-2-carboxylic acid (DHICA, lesser extent) derived from DC decomposition; DHICA production is catalyzed by tyrosinase-related protein-2 (TRP2). As the final step, DHI and DHICA are oxidized by T and TRP1 to obtain eumelanin [75], [76].

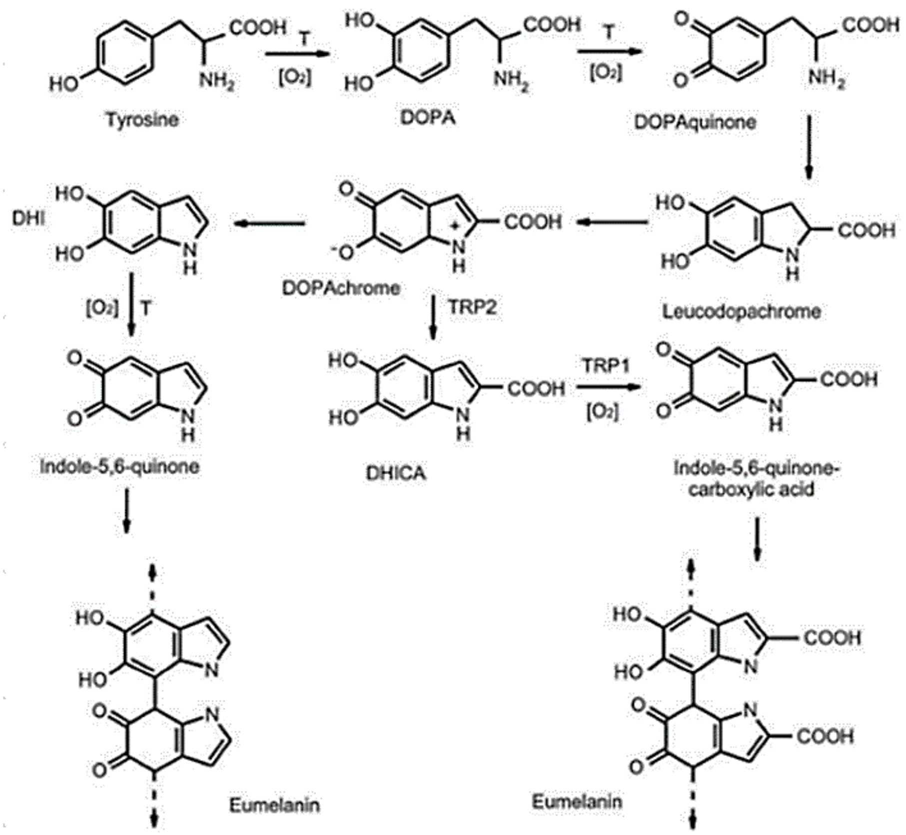

Figure 4. Eumelanin pathways production in melanocytes [75].

These properties of eumelanin are well-defined by the molecular, supramolecular, and aggregate level structure. Nevertheless, despite many decades of research within the organic chemistry, biophysics, materials, and pigment cell communities, there is not yet a conclusive macromolecular structure of eumelanin; derived from the eumelanin insolubility in all solvents and proteins covalently linked to it [77]. Eumelanin cannot be described in terms of a single well-defined structure. It is impossible to provide an accurate picture beyond a statistical description of central units and functional groups.

As mentioned above, eumelanin is mainly built by DHI and DHICA; however, spectroscopic analysis has revealed the presence of redox states and tautomeric forms from these two monomers. **Figure 5** shows the basic monomers constituting the eumelanin; R is referred as *H* or *COOH* in the case of DHI or DHICA. Monomers are covalently bonded by 3, 4, and 7 carbon positions, representing the most probable coupling sites.

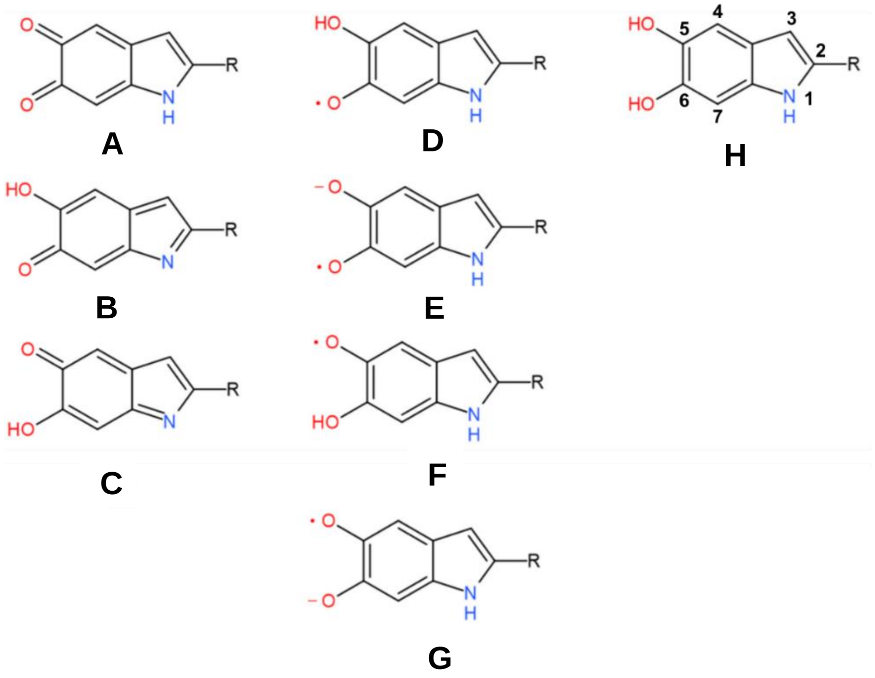

Figure 5. The primary redox states and tautomeric forms of monomers in eumelanin are **A)** indole-quinone (IDQ or IDQCA), **B)** Quinone-methide (QM or QMCA), **C)** Quinone-imine (QI or QICA), **D)** and **E)** Protonated semiquinones, **F)** and **G)** Deprotonated radicals. **H)** 5,6-Dihydroxyndole or 5,6-Dihydroxyndole-2-carboxylic acid (DHI or DHICA) [78].

Figure 6 shows the two most used monomers to explain the PDA structure. **Figure 6A** presents an oligomer formed by four DHI molecules and their different oxidized forms; this cyclic model (Cyclotetramer) has been proposed by Meng and Karixas, obtained through density functional theory (DFT) calculus, and despite explaining the optical absorption of natural melanin and PDA, it has not been experimentally proven [79]. On the other hand, **Figure 6B** illustrates the PDA monomer structure based on spectroscopic and DFT results, the un-cyclic model [61], [80]. In this model, the composition of oligomers is formed by a mixture of indole units with different unsaturation degrees (DHI and its oxidized forms) and open-chain dopamine units (DA) united covalently by carbon atoms in the 4 and 7 positions.

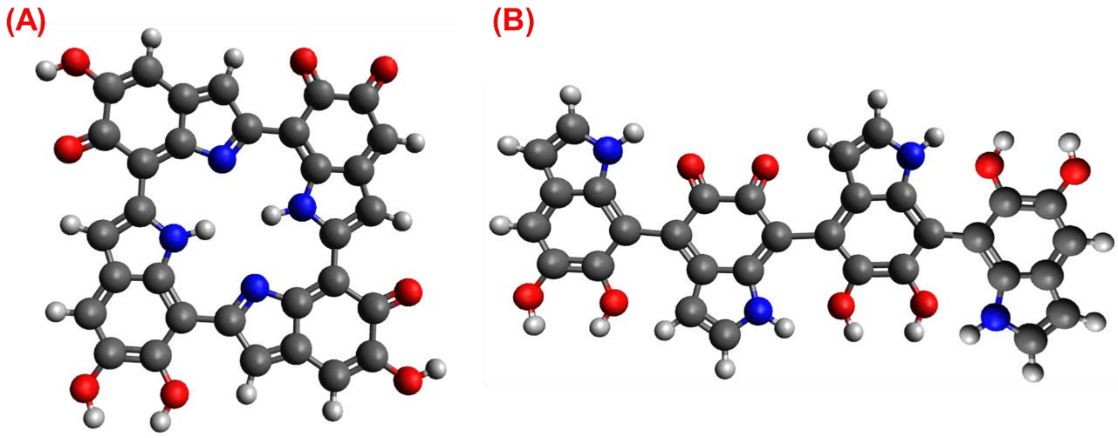

Figure 6. Representation of PDA structure models; **A)** cyclic, **B)** noncyclic. Atoms color: Black, blue, red, and white for Carbon, Nitrogen, Oxygen, and Hydrogen, respectively.

The aggregation of any of these PDA oligomer models constitutes the structure of eumelanin. As shown in **Figure 7**, oligomers formed by melanogenesis possess delocalized *π* – electrons systems that promote interactions between oligomers through *π* – *π* interactions, which allows them to form aggregates (*π* – staking) [61], [81], [82].

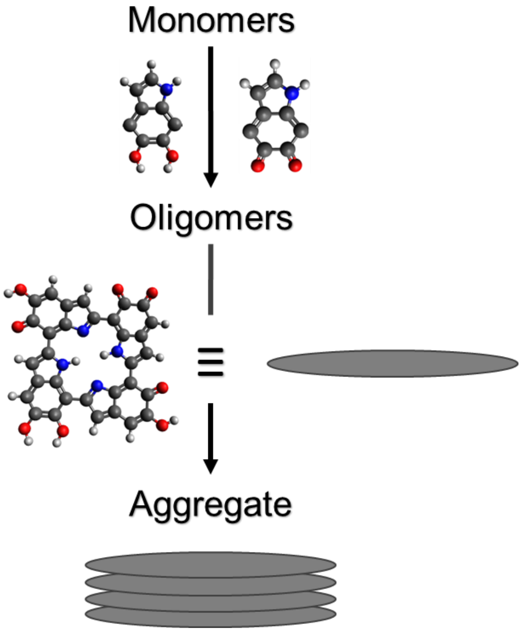

Figure 7. Scheme of the eumelanin build-up.

1.3.2 Eumelanin as photocatalyst

Derived from the extraordinary properties of eumelanin as broadband *UV-Vis* light absorption [13], photocurrent [83], and its *p-type* semiconductor character [84], it has attracted attention to application in the optics and electronics fields as well as in photocatalytic processes. Eumelanin has been used as part of a photocatalytic material derived from the extraction of natural melanin from living organisms or hair from mammalians.

Wanjie Xie et al. realize studies in the degradation of methyl orange and hexavalent chromium ions using a photocatalytic hybrid material based on natural eumelanin isolated from textile scraps like yak hair wastes and TiO_2 nanoparticles synthesized on the eumelanin surface. As we know, TiO_2 displays photocatalytic activity just under *UV* light (*Eg = 3.2 eV*). Nonetheless, the authors report a synergistic effect of both materials that show photocatalytic activity under visible light. They also report the interaction between the catechol groups of eumelanin and Ti to form *C-O-Ti* bonds with TiO_2 nanoparticles and eumelanin to narrow the bandgap and improve the efficiency of the hybrids to remove pollutants [85]. On the other hand, Esmail A. et al. use another hybrid material based on pyrolyzed human hair with TiO_2 deposited on the surface of the fibers. The material was tested in the photodegradation of methyl blue under *UV* and visible light, where it showed better performance compared to just hair fibers or TiO_2. According to the authors, the improved activity of the photocatalyst is caused by the strong interaction between TiO_2 and HHDM (Human-Hair Derived Microfibers), the formation of the *Ti-O-C* bond (ameliorated with thermic treatment at 300 °*C*), and the high porosity of the fibers [86]. The use of eumelanin has been little studied; the difficulty of synthesis implying expensive synthesis cost could explain this.

1.3.3 Polydopamine synthesis and structure

PDA has been considered like synthetic melanin displaying many striking properties of this naturally occurring material in optics [79], electronics [87], electrical [88], and medicine [74]. Functional groups such as catechol and amine are other valuable features in PDA that allow it to perform extraordinary adhesion properties to generate diverse materials such as drug delivery, microfluidic systems, and water treatment devices. Despite these advances, there is no systematic examination of PDA's polymerization mechanism, properties, and broad applications in different research fields.

Under alkaline conditions (pH>7.5), dopamine monomer can be oxidized and spontaneously self-polymerized with oxygen as the oxidant. This method, solution oxidation, is so mild without any complicated instrumentation or harsh reaction condition; this makes it the most widely used protocol for producing PDA.

There have been significant attempts to explain PDA polymerization and structure. During the first moments of the PDA polymerization, according to the literature [39], [89], spontaneous auto-oxidation of dopamine accompanying intramolecular cyclization takes place, where alkali medium ($pH \geq 7.5$) and dissolved oxygen are the key factors of the process; **Figure 8** summarizes this process (Illustration taken from reference [63]). Firstly, the catechol moiety of DA loses an e^- and H^+ to become dopamine-semiquinone (DSQ), to oxidize again later, giving the dopamine-quinone (DmQ). Secondly, DmQ undergoes intramolecular cyclization and oxidation to form leucodopamine-chrome (LDmC), which consequently gives rise to dopamine-chrome (DmC), which can re-arrange to DHI. In addition, in analogy with the eumelanin, the hierarchical structure of PDA has been proposed; oligomers of DA, DHI, or IDQ (oxidized form of DHI) species covalently bounded (*C*-*C*) formed the first stage.

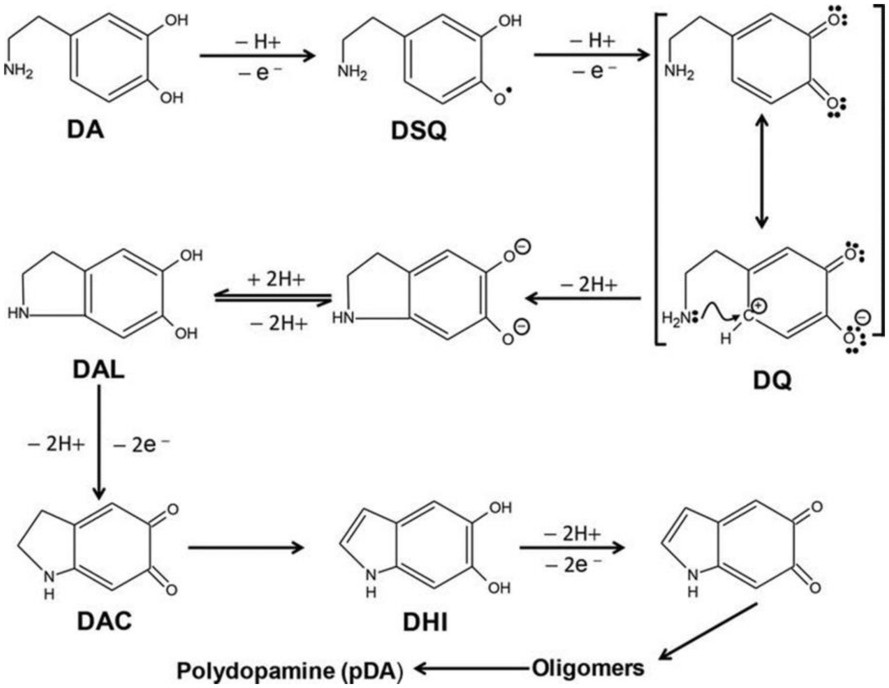

Figure 8. Chemical route of the DA auto-oxidation [89].

According to Messersmith, the structure of PDA is mainly built by DHI and its oxidized forms; however, monomer-precursor species (DA) also conform to the PDA oligomers. These species are covalently linked and flat-form structures ranging from four to six monomers, forming cyclic and noncyclic oligomers. **Figure 9** shows the model of a tetramer of PDA build-up by four monomers, from right to left: DA, DHI, IDQ, and DHI. These oligomers interact by *π* - *π* systems and build stacks that give rise to three-dimensional arrangements as in natural melanin [16], [90]—in analogy to eumelanin, **Figure 7**.

On the other hand, research has indicated that during the self-oxidation of DA, species like pyrrole carboxylic acids or catechol-containing carboxylates can be developed due to the oxidative destruction of the phenyl ring of the indole structures. These can be found as part of the structure of PDA, mainly when L-DOPA is used as a precursor [91]. Despite these attempts, PDA's exact structure is not well defined yet.

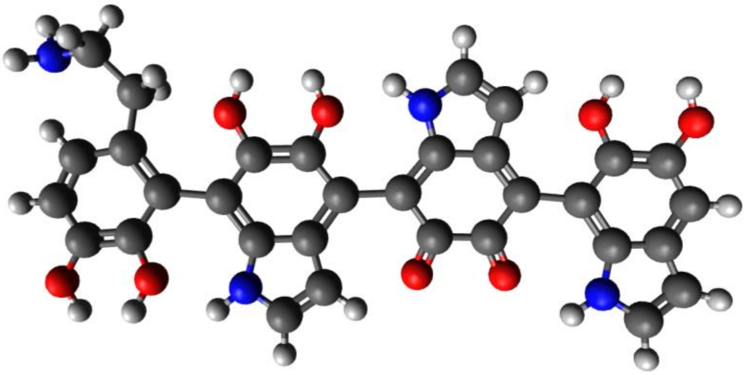

Figure 9. Model of un-cyclic PDA oligomer.

1.3.4 Polydopamine as photocatalyst.

Unlike natural melanin, PDA has been used with many other materials in designing and testing new materials with improved photocatalytic activity. Jiu-Ju Feng et al. synthesized a *Core-Shell* material based on metallic silver and PDA for neutral red photodegradation. The authors take advantage of the great affinity of dopamine and catechol moiety for metallic ions and, in a single step, reduce the Ag^+ ions to metallic silver. At the same time, DA is oxidized and self-polymerized to generate a shell of PDA. The material was tested under UV light (254 *nm*) and showed photocatalytic activity compared to bare PDA and silver nanoparticles. According to these authors, photocatalytic activity exhibited by the photocatalyst is derived from a surface plasmon resonance effect caused by the silver core, which is enhanced by the synergistic effect of the PDA shell caused, in part, by the existence of $\pi - \pi^*$ transitions on PDA. Firstly, neutral red can be absorbed by the PDA shell easily. Secondly, under UV light, the PDA shell can prolong the recombination rate of photoinduced e^-_{CB} / h^+_{VB} pairs [92].

In the same way, Wen-Xin Mao et al. has obtained a *Core-Shell* based on TiO_2 and PDA with photoactivity under visible light to the degradation of rhodamine B. They reported a direct effect of the PDA-shell thickness on the photocatalytic activity since the results show an enhanced degradation of Rhodamine B (RhB) whit a shell thickness of 1 nm compared with bare TiO_2, 2, and 4.5 *nm*. While the detailed interaction mechanism between TiO_2 and PDA is still unavailable, authors reported that PDA could act as an effective agent to modify the surface of TiO_2, which improves the photocatalytic properties of TiO_2 [93]. Xiaoquin Huang et al. also designed a kind of *Core@Shell* material for the photodegradation of methyl blue. Unlike other jobs, the material was based on a hollow core of *BiOCl* with a shell of PDA, and it displays enhanced photocatalytic activity with a 50 *nm* thickness shell. The suggested reason to explain the improved photocatalytic performance in comparison to bare *BiOCl* is 1) The PDA shell provides high specific surface areas and efficient mass transfer for the photocatalytic reaction; 2) PDA serves as a photosensitizer to extend the light absorption range of the catalyst to the visible light region and 3) The *BiOCl-PDA* heterojunction improves the charge separation and interfacial charge transfer to enhance the photocatalytic activity and durability [94]. Likewise, *Core-Shell* materials and other authors also design different photocatalysts based on PDA and semiconductors. Xiaosong Zhou et al. synthesized PDA microspheres with TiO_2 nanoparticles deposited on the surface address to the methyl orange photodegradation under visible light. In concordance with Feng's results, the authors argue an enhancement in photoactivity derived from the PDA absorption of visible light that induces the $\pi - \pi^*$ transition; this means that excited-state electrons from the highest occupied molecular orbital (HOMO) move to the lowest unoccupied molecular orbital (LUMO), then the conduction band of TiO_2 (*CB*) has a similar energy level to the LUMO of PDA and undergoes chemical bond interactions—synergic effect—the electrons are injected in the *CB* to react with water and oxygen molecules to produce hydroxyl and superoxide radicals and carried out the photodegradation of the pollutant. [87]. Yuan Zou et al. used two routes to obtain a photocatalytic material based on PDA particles patched with cadmium sulfur nanoparticles to photodegrade methyl blue under visible light irradiation. Pre- and post-doping was the two ways used in this work for the synthesis of the photocatalyst; as it is known, the catechol group of dopamine molecule has an excellent affinity for metallic ions, which allows a pre-doping technique with subsequent use of these ions trapped on the surface of formed PDA. After PDA formation by DA self-oxidation, catechol groups remain active, which can be profitable for a post-doping process on PDA particles. According to the results, the improving photocatalytic activity is derived from methyl blue, a typical cationic dye that PDA can quickly absorb due to the electrostatic and *π - π* stacking interactions. The photodegradation of methyl blue is then carried out by oxidation in the holes and hydroxyl radicals generated on *CdS*. A relevant fact reported is PDA's contribution to inhibiting the self-photo-corrosion of *CdS* in water [21].

As mentioned above, using PDA increases the materials' photoactivity. Nonetheless, there are yet various questions about the exact effect of PDA on allowing a high photocatalytic activity; the main characteristics exploited are properties such as BandGap, *UV-Vis* light absorption, and specific surface area. These can be modified since the synthesis of PDA implies the importance of studying these properties for using PDA as a photocatalyst.

CHAPTER II: PROBLEM STATEMENT, HYPOTHESIS, OBJECTIVES, AND EXPERIMENTAL

2.1 Justification

In the last 15 years, the research on PDA as a novel material with technological applications has grown exponentially due to its versatility and properties. Nonetheless, there are few studies about the chemical kinetics of dopamine polymerization, which is essential to obtain data such as activation energy, reaction order, and rate constant. It is crucial since this information can facilitate understanding the mechanism implied in dopamine polymerization. In addition, establishing relationships between the synthesis conditions and the final properties of the material will allow the design of PDA materials for specific applications (e.g., the design of materials for the removal of contaminants present in the water). Thus, this doctoral thesis will contribute to the knowledge regarding the PDA.

2.2 Hypothesis

Buffer concentration and temperature in polydopamine synthesis determine the polymerization kinetics. In turn, it influences its physicochemical properties to give a material with photocatalytic activity for the photodegradation of dye pollutants dissolved in water.

2.3 Objectives

2.3.1 General

Determine the kinetics of polydopamine polymerization and correlate it with its final properties to obtain a material with the right features to be used in RhB removal.

2.3.2 Particular

1. Establish the kinetics of dopamine polymerization to obtain polydopamine under different temperatures and tris(hydroxymethyl)aminomethane concentrations.

2. Identify and correlate the synthesis conditions with the final properties of the polydopamine.

3. Evaluate the materials obtained to identify if they have photocatalytic activity and if the synthesis conditions (final properties like particle size, functional groups, or crystallinity) influence this, utilizing rhodamine B as a model pollutant.

4. Identify the main mechanism of polydopamine to the photodegradation of dye pollutants in aqueous media.

2.4 Experimental procedure

2.4.1 Materials and reagents

Dopamine hydrochloride (98 %) and Tris(hydroxymethyl)aminomethane (named TRIS, ≥ 99.8 %) were purchased from Sigma Aldrich. All the chemicals were used as received, i.e., without further purification. The solutions were prepared with deionized water (18.2 *MΩ cm*).

2.4.2 Synthesis of PDA

Briefly, 300 mg of dopamine hydrochloride (DA) was dissolved in a ball flask with 150 *ml* of deionized water (13 *mM*), **Figure 10**. The solution was stirred using a magnetic bar; meanwhile, three different quantities, 1.5 *mmol* (*pH* = 8.50 at 25 *°C*), 4.5 *mmol* (*pH* = 8.98 at 25 *°C*), and 7.5 *mmol* (*pH* = 9.50 at 25 *°C*) of TRIS were added at 25, 40, and 55 *°C*. After 24 hours, the solution was centrifuged at 6000 *rpm* for 20 minutes and washed several times with deionized water to remove synthesis residues. The sediment was dried at 80 *°C* for 6 hours.

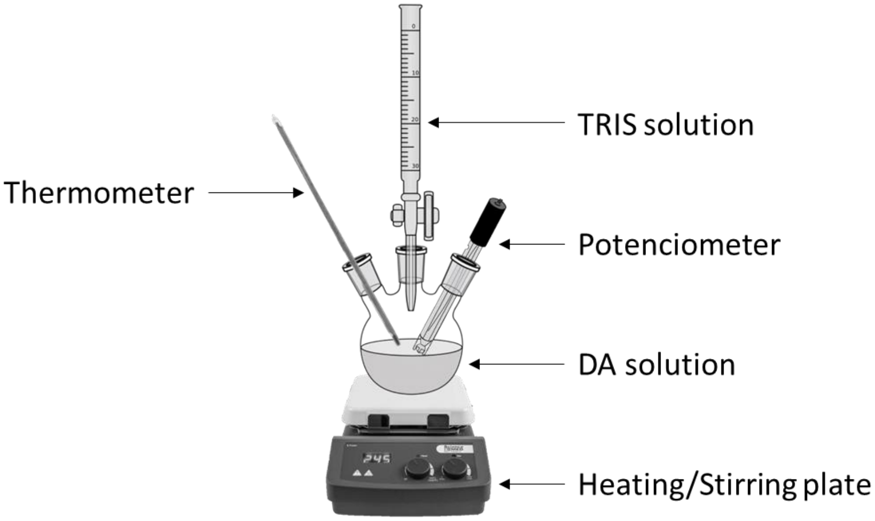

Figure 10. The system used for the PDA synthesis.

2.4.2.1 *Kinetic analysis of the PDA synthesis*

The polymerization reaction was monitored by UV-Vis spectrometry in a quartz cell with a *UV-Vis-NIR* spectrometer, CARY 5000 (Agilent, USA). The aliquots were taken at 0, 1, 2.5, 5, 15, 45, 90, 180, 360, 600, and 1400 minutes; such aliquots were analyzed in the range of 250 to 350 *nm*, where the maximum absorbance of DA was located at 280 *nm*. For a correct measure of the absorbance, the aliquots were diluted with a factor of 20. The *UV-Vis* spectrum of PDA suspension was carried out at 1400 minutes from 200 to 500 *nm*.

2.4.3 Characterization of PDA

2.4.3.1 *Morphology and particle size*

The morphology of synthesized material was observed by Scanning Electron Microscopy in a Dual Beam Helios Nanolab 600 (FEI, USA) operated at 8.00 *kV*, a work distance of 5.0 *mm*, and a secondary electron detector; the samples were supported on carbon tape. The diameters of the particles were measured using the software ImageJ. The used micrographs were taken at 25 000 x with measurements of 80 particles.

2.4.3.2 *Thermal characterization*

The thermal transitions were obtained by Differential Scanning Calorimetry (DSC) using a Q200 calorimeter (TA Instruments, USA) with a heating rate of 10 *°C/min* from -50 to 250 *°C* under a nitrogen atmosphere. The Thermogravimetric Analysis (TGA) was conducted using Q500 equipment (TA Instruments, USA) with a heating rate of 10 *°C/min* from room temperature to 700 *°C* under a nitrogen atmosphere.

2.4.3.3 *Spectroscopic analysis*

For such analysis, the Fourier Transform Infra-Red (FTIR) was obtained with a spectrophotometer Nicolet iS10 (Thermo Scientific, USA) using the ATR mode with 256 counts and 4 cm^{-1} resolution, from 550 to 4 000 cm^{-1} wavenumber range. At the same time, the Raman spectroscopy was carried out using a Micro Raman (Renishaw, UK), laser excitation at 532 *nm*, and a Raman shift range from 500 to 2000 cm^{-1}. All spectra were processed to establish the same baseline.

2.4.3.4 X-Ray diffraction

XRD spectra were collected on an X-Ray diffractometer D8 Advance (Bruker, USA) using *Cu K α* radiation with a diffraction angular range from 5° to 60° in 2θ.

2.4.4 Absorption and photocatalytic test

The adsorption properties were evaluated in a glass reactor with RhB as a model pollutant. The initial concentration of RhB was 10 *mg/L*, and a concentration of 0.6 *g/L* of material was used. Aliquots were taken each hour for 8 hours and were analyzed by UV-Vis spectroscopy with a quartz cell in a *UV-Vis-NIR* spectrometer, CARY 5000 (Agilent, USA).

The photocatalytic activity assays were carried out under the same conditions for an hour in darkness, and then the reaction was carried out under stirring and visible light. The source light was a fluorescent mercury lamp of 8 *watts*, and the distance between the source and the solution surface was 82 *mm*.

The photocatalytic reaction was carried out under the same conditions and with PDA obtained at 25 *°C* and 1.5 *mmol* of TRIS to determine PDA's photocatalytic mechanism. Methanol and silver nitrate solutions (adjusted with 2 *mmol*) were used as holes and electron scavengers.

CHAPTER III: PDA SYNTHESIS

Thermodynamic and kinetic PDA synthesis studies are critical to establishing parameters like reaction order (*n*), pre-exponential factor (*A*), and activation energy (E_a). Such parameters are essential for polymerization control, affecting the material's final properties, and are critical to the technological use of the PDA. In this context, M. Salomäki *et al.* [34] did a thermodynamic study of dopamine oxidation and cyclization dependence from *pH* and oxidants like transition-metal ions, mainly focused on the early stages of the process. The authors proposed a general mechanism to understand the involved species during PDA polymerization and concluded that the most critical parameter for the process is the *pK* value. In the same way, the use of tuning radicals to control the size of PDA nanoparticles is reported by X. Wang *et al.* [35]. In the latter study, the authors concluded that the polymerization could be inhibited or terminated from the free radical scavengers, while the stable radicals catalyzed the formation of PDA seeds. A comparable study was carried out by M. Wu *et al.* [36], who synthesized PDA through sodium hydroxide and developed a model about relationships between particle size, the molar ratio of DA, and oxidizing agent to control the particle diameter and distribution. In addition, V. Ball *et al.* [95] studied the film deposition kinetics influenced by *pH* and DA concentration; their effect on thickness, morphology, roughness, and surface energy expressing the relationship between maximal thickness and kinetic constant to obtain thickness higher than 45 *nm*.

In summary, controlling the PDA polymerization reaction is essential since it controls its yield, particle size, and properties like photothermal effect, UV protection, and free radical scavenging activity [36], [37]. So far, the studies regarding the kinetics of PDA synthesis are few. Usually, the polymerization rate is reported, but other relevant kinetics parameters like *n*, *A*, and E_a are not provided. In this work, the aforementioned kinetic parameters are determined, and their relationship with the structure and properties of PDA is established.

3.1 Synthesis of polydopamine

UV-Vis spectroscopy determined the dopamine concentration at every condition over time to evaluate its consumption kinetics. **Figure 11A** shows the *UV-Vis* spectra of dopamine solution at different reaction times with 1.5 *mmol* of TRIS. The maximum peak absorption is observed at 284 *nm*, which corresponds to the absorption by the aromatic ring in DA [96]. The spectra of the other reactions follow a similar trend; Consequently, we show only the spectra at 1.5 *mmol* tris and 25 *°C*. It is worth mentioning that PDA is a material with broadband monotonic absorption without a specific absorption wavelength. Thus, the spectrum of PDA is characterized by an exponential increase in absorbance toward the ultraviolet spectrum [97]; see **Figure 11B**. Different points of view have been put forth to explain the origin of PDA's broadband absorption. For instance, according to R. Micillo *et al.* [98], the broad spectra of PDA in *UV-Vis* could be related to the 5,6-dihydroxindole (DHI) based oligomers of the material and its delocalized π – electrons systems. Nevertheless, another accepted theory argues that absorption in the ultraviolet region is due to dopamine transformation into dopachrome and dopaindol. At the same time, the presence of monomers (DA) in the PDA structure could generate absorption from visible to infrared wavelengths, which results from the subsequent self-polymerization process [16], [99].

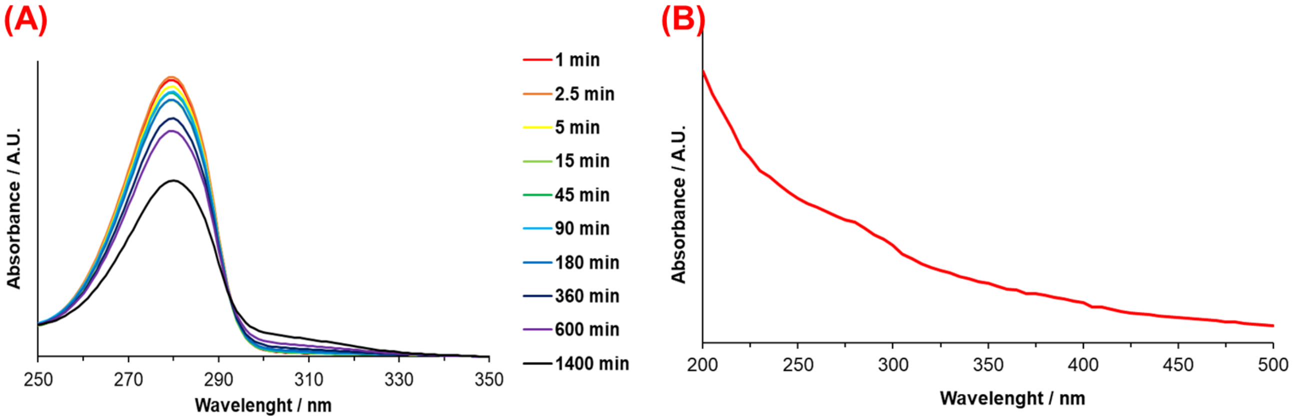

Figure 11. A) UV-Vis spectra of the DA solution at different reaction times with 1.5 *mmol* of TRIS and 25 *°C*. **B)** PDA spectrum in water solution.

Regarding the color of the solution, from **Figure 12; A), B),** and **C),** it is clear that it changed according to the reaction extent and depending on its initial reaction temperature. A color change from pale yellow to dark brown indicates the self-oxidation of DA to obtain PDA. Temperature accelerates such oxidation, so a darker solution for the highest temperature (*55 °C*) is observed earlier than the reactions at 25 and 40 *°C* (**Figure 13**). Thus, the influence of temperature on the reaction rate is evident, and an Arrhenius-type behavior is expected.

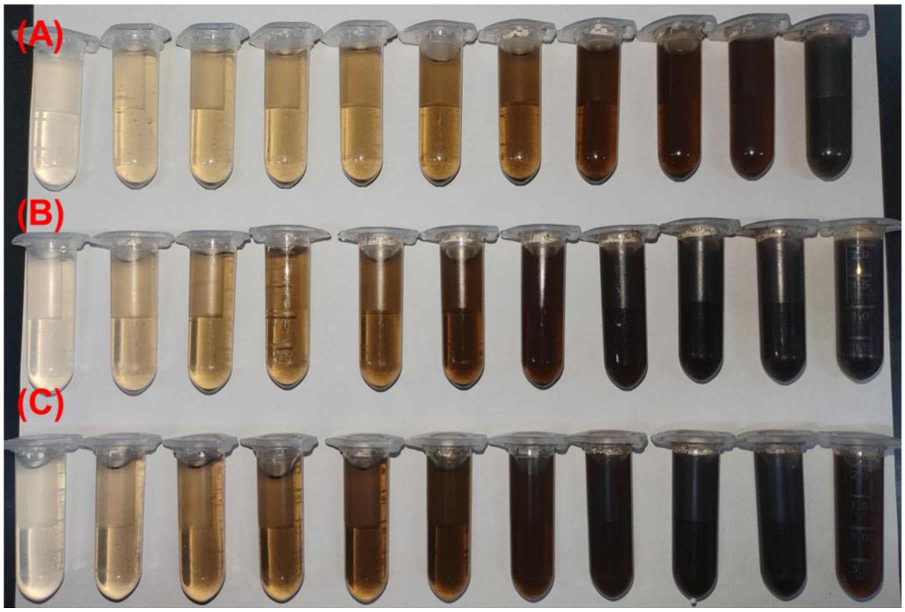

Figure 12. Reaction solution color change with 1.5 *mmol* TRIS, **A)** at 25 °C, **B)** at 40 °C, and **C)** at 55 *°C*.

3.1.1 Polymerization kinetics

Figure 13 shows the DA concentration profile over time for every synthesis condition. The mathematical model used to adjust the data exhibited an exponential decrease. Regarding the general expression, *reagents → products*, **Equations 16** and **17** display the reaction of DA conversion to PDA and the rate law, respectively.

$$DA \xrightarrow{pH > 7.5} PDA \tag{16}$$

$$-\frac{d[DA]}{dt} = -r_{[DA]} = k[DA]^n \tag{17}$$

Applying natural logarithms to **Equation 17**, the mathematical equation corresponds to a linear equation **(Equation 18)**, where the slope corresponds to the reaction order *n* and the intercept *b* corresponds to *Ln(k),* from which the rate constant can be obtained.

$$Ln\left(-r_{[DA]}\right) = nLn([DA]) + Ln(k) \tag{18}$$

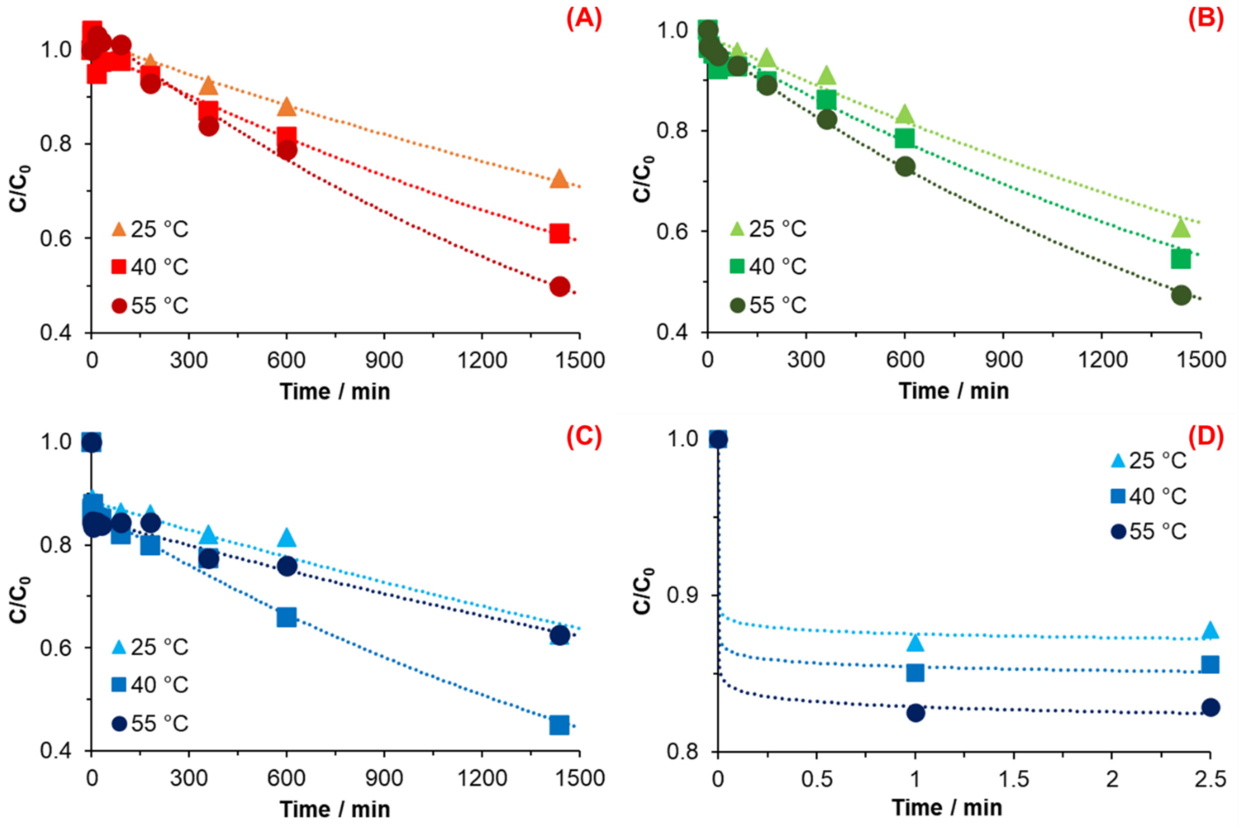

Figure 13. Change of dopamine concentration against time and exponential decline fitting for **A)** 1.5 *mmol* TRIS, **B)** 4.5 *mmol* TRIS, **C)** 7.5 *mmol* TRIS, and **D)** Zoom of the reaction onset at 7.5 *mmol* TRIS.

Table. 2 summarizes the values of the rate constant and reaction order from each temperature and TRIS concentration used.

Table 2. Reaction order and rate constants for every reaction condition.

T / °C	$n_{1.5}$	$k_{1.5}$ / *min*$^{-1}$	$n_{4.5}$	$k_{4.5}$ / *min*$^{-1}$	$n_{7.5}$	$k_{7.5}$ / *min*$^{-1}$
25	1.00	2.38E-04	0.98	2.53E-04	0.92	1.50E-04
40	0.97	3.26E-04	0.98	3.28E-04	0.98	3.97E-04
55	0.98	5.10E-04	1.00	4.65E-04	0.97	1.78E-04

The synthesis of PDA with 1.5 *mmol* showed an increase in the reaction rate (**Figure 13A**) as the temperature was increased, as was expected (**Table 2**). This behavior indicates that the reaction, under such conditions, follows typical behavior in terms of kinetics and the mechanism as proposed by Della Vecchia *et al.* [100]. Chemical kinetics, specifically the theory of collisions, indicates that the kinetic energy of the molecules also increases when temperature increases in a chemical reaction. Consequently, the molecules have more energy to react and form products due to more collisions caused by the temperature increase [101], which exhibit an increment of 0.37 and 1.14 times when the temperature increases to 40 and 55 *°C*, respectively, concerning the rate constant at 25 *°C*.

The reaction order of the synthesis carried out with 1.5 *mmol* of TRIS was $n \sim 1$ for every temperature. It means that the reaction of PDA formation depends linearly on the DA concentration. In other words, the reaction order of PDA synthesis implies the exponential decrease of DA concentration as a function of time, while the reaction rate decrease linearly as a function of concentration.

Figure 13B displays the relationship of DA concentration vs. time at 25, 40, and 50 *°C* with 4.5 *mmol* of TRIS; the calculated values of the reaction order and rate constant for every reaction temperature were $n \sim 1$ and k = 2.53E-04, 3.28E-04, and 4.65E-04 min^{-1}, respectively. In the same way, reactions carried out at 4.5 *mmol* TRIS show similar behavior concerning 1.5 *mmol* when the temperature increases; it represents an increment of the k as the temperature increases.

A TRIS concentration effect can be noticed when the rate constants of 1.5 and 4.5 *mmol* TRIS are compared. TRIS molecule possesses three *OH* groups which are ionized in solution; a higher concentration of OH^- ions means that the Michael addition is accelerated [102]. Michael's addition is an essential step in the DA auto-oxidation for the formation of DmQ, where the catechol moiety of DA is oxidized, losing an e^- and H^+ with the participation of O_2. However, this increase in the k value derived from hydroxyl ions concentration is limited to 25 and 40 *°C* since 55 *°C* is smaller than the k calculated with 1.5 *mmol* at the same temperature.

As mentioned by M. Wu *et al.* [36], the synthesis of nanoparticles of PDA implies two stages. The first is the formation of PDA seeds, which grow during the second stage. Variables like temperature, pH, oxidants, and concentration of DA during its polymerization affect both stages. Polymerization of DA is accelerated by a high initial concentration of OH^- ions. In parallel to an increment in temperature, its effect leads to a higher nucleation rate of PDA particles and, thus, to forming more seeds [100], [103]. However, DA as a precursor for the PDA synthesis is consumed rapidly, and when more nuclei are formed, DA becomes unavailable for the particle growth stage. We assume that due to a slower growth stage of PDA particles, the observed k at 55*°C* with 4.5 *mmol* TRIS could be lower than k with 1.5 *mmol* TRIS at the same temperature.

Figures 13 C and **D** illustrate the change in DA concentration over time for reactions with 7.5 *mmol* TRIS. **Figure 13D** displays the change in DA concentration at 0, 1, and 2.5 minutes where a sudden decrease in DA concentration is observed as the TRIS solution is added. This reduction conveys an increment in TRIS concentration and temperature, which is correlated with the formation of seeds during the first stage of PDA polymerization. **Figure 14** shows the percent decrease in DA at the first instant after TRIS addition for all concentrations and temperatures to estimate the oxidized DA and consumed for PDA nuclei. As is exhibited, for the reaction with 1.5 *mmol* TRIS, there is no sudden consumption of DA in the nuclei formation stage at the measurement's first time. However, for reactions at 4.5 *mmol* TRIS, one can notice a reduction of 2 % in the DA concentration at 25 *°C*, which increases to 3.4 % for the reaction at 55 *°C*; likewise, at 7.5 *mmol* TRIS, the DA concentration reduces by 11.7, 13.5, and 15.8 % for 25, 40 and 55 *°C*, respectively. As mentioned before, OH^- ions and temperature accelerate the DA oxidation, which promotes the formation of DQ, an essential step for the PDA seeds formation; from these results, it is also observed that an increment in TRIS concentration is more relevant for nuclei construction than an increment in temperature. At 25 °*C*, the consumption of DA was 0, 2.00, and 11.72 % as the hydroxyl ions increased, an effect also observed for 40 and 55 °*C*, where the percentage of DA decrease was from 0 to 3.41 and 13.46 %, and from 0.61 to 3.44 and 15.74 %, respectively. In contrast to TRIS concentration, the lower effect of temperature could be explained as the dependence on dissolved oxygen, which is essential for the auto-oxidation of DA [104].

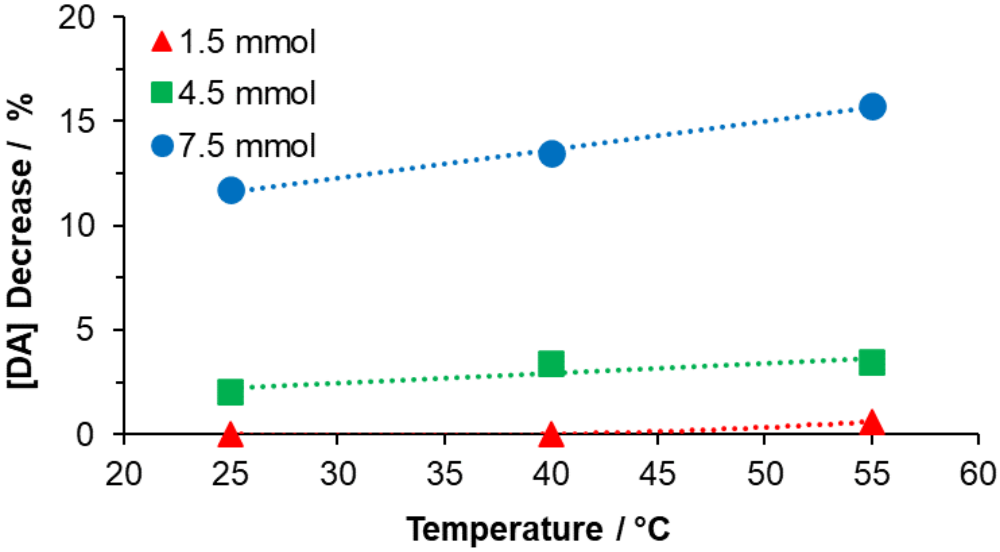

Figure 14. Effect of the TRIS solution on DA consumption in the solution immediately after its addition (one minute after).

From the results observed for DA polymerization with 7.5 *mmol* of TRIS was supposed that the reaction has two different rate constants. The first is associated with the sudden decrease of DA at the first moments of the reaction, and the second is related to the subsequent reduction of DA. Due to the high-speed consumption of DA, it was not possible to determine the rate constant at the first moments. At the same time, the reaction order was assumed to be of superior order, which explains the decrease in DA concentration over time. From the profiles obtained with 7.5 *mmol* TRIS shown in **Figure 13D**, the second rate constant, the reaction rate at 55 °*C*, is lower than that at 40 °*C* and is similar to that of 25 °*C*. The computing values for reaction order and rate constants at 25, 40, and 55 °*C* were n ~ 1; and k = 1.50E-04, 3.97E-04, and 1.78E-04 min^{-1}, respectively. When the temperature rises to 40

°*C*, the rate constant increases 1.64 times in relationship with *k* at 25 °*C*, corresponding with an Arrhenius behavior and an increment of OH^- concentration.

Nevertheless, the rate constant decreases when the temperature increases to 55 °*C*. According to Wang X. *et al.* [35], using free radical scavengers (*i.e.,* edavorone) has an inhibition or termination effect during the DA polymerization, resulting in a decrement in particle size and yield. This effect occurs due to a reduction process promoted by edavorone during the oxidation of DA to DSQ species formation. It serves as an *H* - atoms donor to DSQ, which generates stable compounds. When the reaction is carried out at high temperatures, it implies the dissociation of water molecules, changing the concentration of H^+ and OH^- ions; in parallel, the generated species during DA oxidation with dissolved oxygen like H_2O_2 and $HO_2^{\bullet}$ (Salomäki, M. *et al.* [34]) also could be a source of H^+*.* Herein, we speculate that very high OH^- ions concentrations (TRIS) affect the chemical kinetics of PDA polymerization, causing the inhibition/termination of the growth stage of PDA particles; thus, a lower *k* at 55 °*C* is obtained. In other words, when rate constants at 55 °*C* at different TRIS concentrations (**Table 2**) are compared, it is observed that reversibility in the DQ formation and inhibition/termination effects are more substantial when temperature and TRIS concentration increase, affecting the particle size, rate constant and yield—similar results were reported by X. Wang et al. where higher pH values (> 9.55) gave lower yields.

According to chemical kinetics principles, most chemical rate constants increase as the temperature rises, and the Arrhenius equation (**Equation 19***)* expresses this relationship.

$$k = Ae^{-E_a/RT} \qquad \textbf{19}$$

The Arrhenius parameters, activation energy (E_a), and pre-exponential factor (*A*) were calculated from the plot of *Ln(k)* against *1/T* that gives a straight line ($y = mx + b$) where the slope (*m*) is $m = -E_a / R$, while $b = Ln(A)$ provides the pre-exponential factor, see **Table 3.** The E_a is the minimum kinetic energy that reactants must have to generate products. Thus, 20.6 $kJ\ mol^{-1}$ is the E_a computed for the reaction at 1.5 *mmol* while, for 4.5 *mmol*, it decreases to 16.48 $kJ\ mol^{-1}$. This effect means that a high *pH* (concentration of OH^-) reduces the activation energy—four-fifths compared to 1.5 *mmol*—needed to carry out the reaction of DA polymerization. In addition, the calculated E_a at 7.5 *mmol* TRIS, just for 25 and 40 *°C*, is 50.27 $kJ\ mol^{-1}$. High activation energy values imply a strong dependence of the rate constant on temperature, a result supported by the above-calculated rate constants. Moreover, in the case of 40 and 55 *°C*, the obtained E_a = - 45.5 $kJ\ mol^{-1}$ describes the rate decrease as the temperature increases.

Table 3. Activation energy and pre-exponential factor computed from rate constants.

	1.5 mmol	***4.5 mmol***	***7.5 mmol***
E_a / $kJ\ mol^{-1}$	20.60	16.48	50.27
A / min^{-1}	0.94	0.19	96, 374

Figure 15 shows the plot E_a vs. *Ln(A)*; as is observed, *A* for DA polymerization increases linearly with E_a. This relationship is explained by Brønsted acid sites (or active sites) in catalysts [105], [106]. According to these works, an increase in active centers corresponds to a higher value of A; also, for statistical and thermodynamic reasons, these active sites should be more numerous with decreasing energy. Additionally, they are less effective with lower energy. In other words, low energy in the active centers is accompanied by a high value of E_a.

Above all, this linear relationship between E_a and *Ln(A)* could be explained by DA polymerization in the growth stage. DA monomers react on the surface of previously formed PDA particles, where active sites like catechol moiety (acid site) and secondary amine (basic site) can affect the auto-oxidation and polymerization of DA.

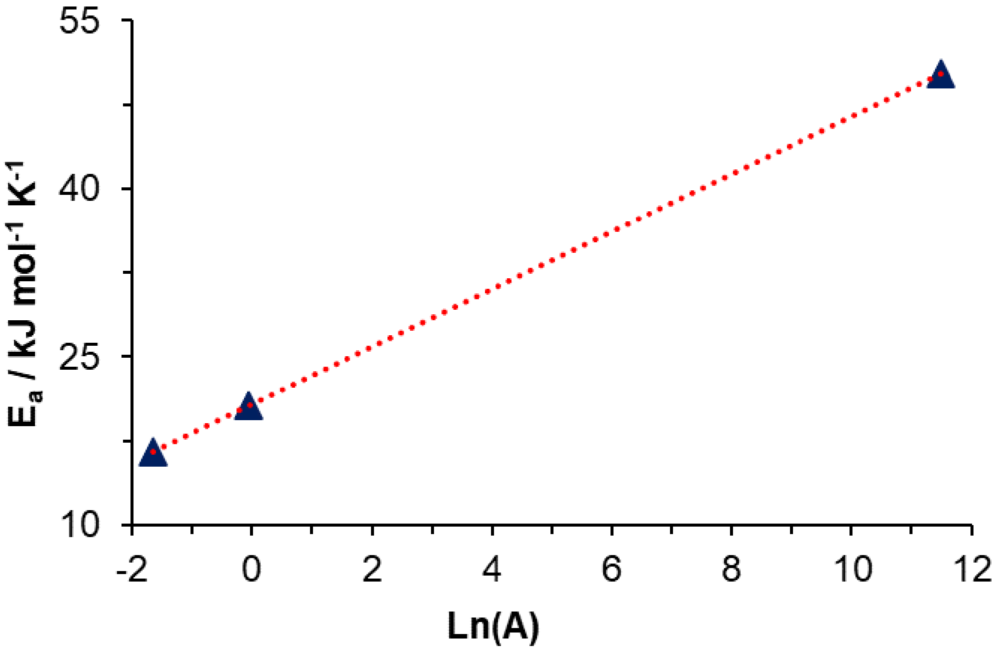

Figure 15. E_a vs. *Ln(A)* for reactions at 25, 40, and 55 *°C*.

3.1 Morphology and particle size

Figure 16 shows the micrographs for every PDA sample obtained by scanning electron microscopy and its corresponding particle diameter distribution (**Table 4**). The results for 1.5 TRIS concentration at 40 and 55 *°C* (**Figure 16; B** and **C**) display an average radius of 170.8 and 358.8 *nm* with broad particle distributions and standard deviations (SD) of 255.6 and 181.7, respectively. These materials, obtained at 40 and 55 *°C*, show a variety of particle sizes composed of separated and agglomerated particles, in contrast with the material obtained at 25 *°C* (**Figure 16A**) that displays seemingly small regular fused particles forming large agglomerates. Agglomerates observed at 25 *°C* could be formed by seeds that grow and fuse as the reaction advances. However, when the temperature increases, well-defined and bigger particles appear.

The Ostwald ripening process explains a wide distribution of diameter particles at 40 and 55 *°C* [107]. This process occurs when small particles are dissolved; the DA monomers from the surface of the smaller particles migrate to larger ones, resulting in bigger particles and wide distribution due to the higher surface energy of smaller particles; according to the Gibbs-Thompson relationship, these tend to dissolve.

Table 4*.* Diameter and SD of particle size.

Material		***Diameter / nm***	***SD***
1.5 mmol	***25 °C***	---	---
	40 °C	438.4	255.6
	55 °C	358.8	181.7
4.5 mmol	***25 °C***	661.2	148.0
	40 °C	424.6	40.9
	55 °C	173.3	11.3
7.5 mmol	***25 °C***	564.6	29.1
	40 °C	276.4	18.6
	55 °C	334.3	16.9

The micrographs at 4.5 *mmol* TRIS (**Figure 16; D**, **E**, and **F** for 25, 40, and 55 *°C*, respectively) show well-defined spherical particles with a narrow distribution (**Table. 4**). A more spherical morphology is observed as a result of a higher concentration of TRIS than reactions at 1.5 *mmol* TRIS. Additionally, the temperature also affects the size distribution and average diameter.

Results from 7.5 *mmol* TRIS concentration at various temperatures (**Figure 16; G**, **H**, and **I**) also show well-defined particles with average diameters of 564.6, 276.4, and 334.3 *nm* and SD of 29.1, 18.6, and 16.9 *nm*, respectively. In the same way, the effect of higher TRIS concentration gives better-defined particles. However, the diameter of PDA particles is not correlated with temperature since an increment from 25 to 40 *°C* represents a decrement from 564.6 to 276.4 nm. Nevertheless, when the temperature increases to 55 *°C*, the average size increases to 334 nm. In order to explain the change in particle size, the rate constant has a better fit. Although the temperature affects the rate constant, the inhibition/termination effect on PDA polymerization affects the rate constant and particle size, as mentioned before.

In summary, the polymerization of PDA strongly depends on TRIS concentration and temperature; higher concentrations of TRIS encourage well-defined spherical particles and affect the particle size and distribution, an equally promoted effect by temperature from the rate constant.

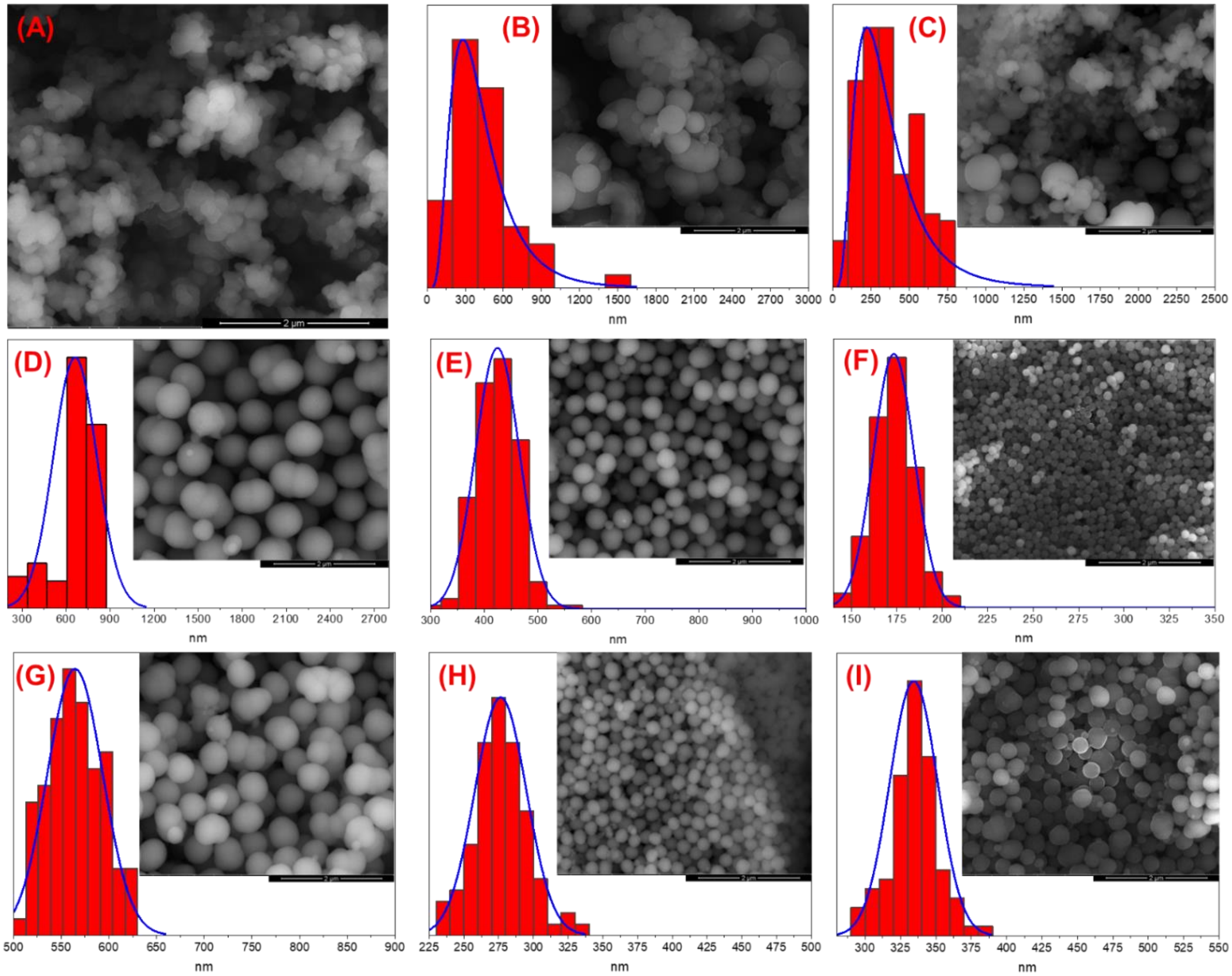

Figure 16. Micrographics of PDA synthesized at different conditions and particle diameter distribution; **A)** 1.5 *mmol*, 25 *°C*, **B)** 1.5 *mmol*, 40 *°C*, **C)** 1.5 *mmol*, 55 *°C*, **D)** 4.5 *mmol*, 25 *°C*, **E)** 4.5 *mmol*, 40 *°C*, **F)** 4.5 *mmol*, 55 *°C*, **G)** 7.5 *mmol*, 25 *°C*, **H)** 7.5 *mmol*, 40 *°C* and, **I)** 7.5 *mmol*, 55 *°C*. The bar represents 2 *µm*.

3.2 Thermal analysis

Thermogravimetric analysis of DA (**Figure 17A**) shows thermal stability up to 210 *°C*; after this point, dopamine degradation begins. Two main thermal stages are observed; the first is from 210 to 330 *°C*, where the degradation of catechol moiety is carried out, and the second is from 330 to 465 *°C*, associated with the decomposition of the alkyl spacer and the amide group [108]. The residue was 18.7% which corresponds to calcinated DA.

In the case of PDA, **Figure 17B** shows the TGA thermograms of PDA synthesized with 1.5, 4.5, and 7.5 *mmol* TRIS. All the materials show similar and multistep weight loss associated with chemical heterogeneity. Four steps in the thermal degradation of PDA are identified; the first one is related to the evaporation of weakly bound water due to high PDA hygroscopicity [45], observed from 25 to 100 *°C*. The second one—between 100 and 240 *°C*—corresponds to the release of intramolecular, strongly-bonded water [109]. The third step associated with the decomposition of aliphatic components [110] presented in PDA originated from DA molecules non-oxidized during the polymerization. Finally, with a final average mass retention of 56.2 %, the last step from 420 to 700 *°C* matches with aromatic compounds degradation like catechol or the o-benzoquinone moieties that decompose in this temperature range [47].

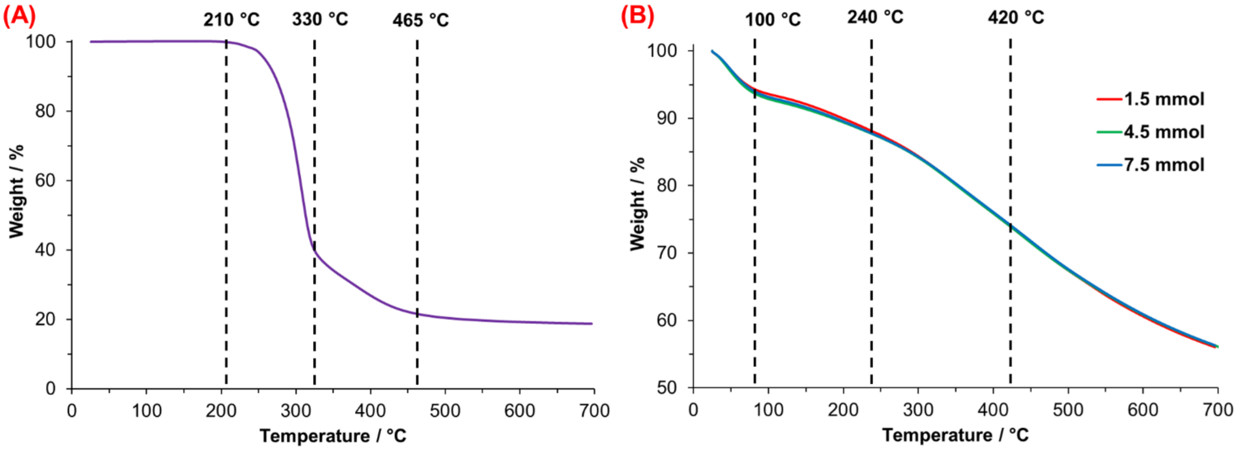

Figure 17. Thermogravimetric analysis of **A)** Dopamine hydrochloride (DA•HCl) and **B)** synthesized PDA at 25 *°C*.

Table 5 summarizes the loss in weight of PDA computed for each material at the final temperature of the four-step degradation process. The weight loss at 100 *°C* oscillates between 6.30 and 7.12 %, with differences of 0.31 %; this was the highest difference value of the four steps losses associated with the high material hygroscopicity. Molecular water trapped between PDA microstructure from the synthesis medium needs more heat to be released; the average weight loss of this process was 5.57 %, with narrow differences (variation of 0.17 %). The average weight loss of 25.8 % at 420 *°C* is 0.19 %, similar to the variation at 700 *°C* (0.13 %). Low differences and similar behavior of PDAs after 240 *°C* could be associated with the similar chemical composition of PDA synthesized under different conditions.

The literature about natural and synthetic melanin postulates that these materials do not have a defined structure, considering them amorphous materials [68], [111]–[113]. On the other hand, E. Coy *et al.* [114] have reported contradictory results for synthesized PDA characterized by Raman spectroscopy without any thermal treatment, which shows characteristics related to carbonized PDA particles; this material displays regular zones that indicate nanocrystalline graphite-like structure [115]. In addition, according to polymers science [116], [117], characteristic endothermic peaks observed by DSC are associated with the fusion of crystalline regions present in the microstructure of polymers [118]. The crystalline fraction can be computed by the quotient of the melting enthalpy (heat associated with the fusion process) measured and the melting enthalpy of the completely crystalline material.

The first authors who proposed the relationship between the endothermic process of natural and synthetic melanin and a phase transition based on the granule nucleus organization were Simonovic B. *et al.* [119]. The DSC thermograms of PDA are shown in **Figure 18**. A broad endothermic peak with a maximum is observed between 98 and 146 *°C*; this first-order transition is linked with the melting process of PDA. As mentioned above, the chemical composition of PDA consists of layers (oligomers) composed of 3 - 4 units of mainly 5,6-dyhydroxindole and DA molecules covalently bonded. Simultaneously, these layers interact by $\pi - \pi$ systems, giving rise to ordered short-range regions. These arrangements, known in polymer science as lamellae crystals, suggest the presence of crystalline areas in PDA, which are destroyed by heating, explaining the transition observed by using the DSC.

The thermograms show the effect of synthesis conditions through the shape—narrow or broad—of the endothermal peak (melting temperature) and melting enthalpy. Such thermograms indicate different melting temperatures due to crystallite imperfections and non-uniformity in their size. For instance, Yu, X. *et al.* [120] reported dark domains of graphite-like nanostructures with short-range (2-3 layers) and large-range (~40 layers) on calcinated PDA particles using High-Resolution Transmission Microscopy.

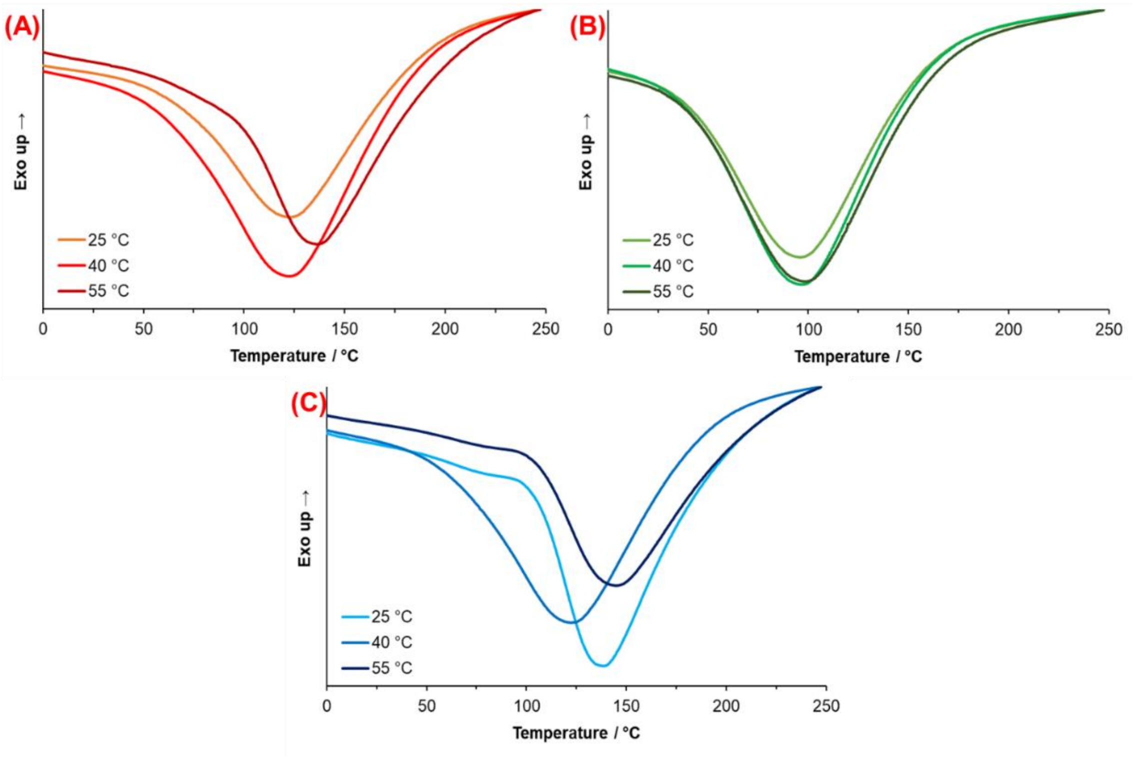

Figure 18. Thermograms obtained from PDA synthesized at **A)** 1.5 *mmol*, **B)** 4.5 *mmol*, and **C)** 7.5 *mmol* for each temperature.

Table 5. Thermal characteristics of PDA observed by TGA and DSC.

Material		*Weight loss / %*				*DSC results*	
		25 - 100 °C	*100 - 240 °C*	*240 - 420 °C*	*420 - 700 °C*	*Melting Peak / °C*	*Enthalpy / J g^{-1}*
1.5 mmol	***25 °C***	6.42	12.13	26.04	43.92	125.0	304.5
	40 °C	6.82	12.34	25.60	43.66	124.5	340.9
	55 °C	6.39	12.00	25.79	43.93	137.2	346.6
4.5 mmol	***25 °C***	6.30	12.05	26.03	43.89	98.1	308.2
	40 °C	7.12	12.39	25.82	43.89	99.1	412.5
	55 °C	6.97	12.44	25.62	43.67	100.8	297.9
7.5 mmol	***25 °C***	6.42	12.13	26.04	43.92	139.2	307.5
	40 °C	6.39	12.00	25.79	43.93	123.9	338.9
	55 °C	6.82	12.34	25.60	43.66	145.7	280.2

Figure 18 illustrates the PDA thermograms synthesized with 1.5, 4.5, and 7.5 *mmol* TRIS at the three temperatures. Thermograms from synthesis at 4.5 *mmol* TRIS (**Figure 18B**) show similar melting enthalpies compared with 1.5 and 7.5 *mmol* TRIS, but the melting points are lower (between 27 and 35 *°C*, **Table 7**). These results indicate that *pH* (TRIS concentration) and temperature have an essential effect on the conformation of PDA microstructure with an accentuated effect at 4.5 *mmol* TRIS concentration.

The associated enthalpy for each material is also listed in **Table 7**. It is worth mentioning that no data exists in the literature about melting enthalpy for crystalline PDA. Thus, it is impossible to calculate the crystalline fraction of these materials. However, if it is assumed that the PDA with the higher enthalpy value has the highest crystalline fraction (100%), obtained with 4.5 *mmol* TRIS at 40*°C*, then 7.5 *mmol* TRIS at 55 *°C* produces the PDA with the lower crystalline fraction, 67.98 %.

On the other hand, a minimum effect of TRIS concentration on the melting enthalpies for 1.5, 4.5, and 7.5 *mmol* at 25 *°C* is noticed. When the temperature increases to 40 and 55 *°C*, the effect of TRIS concentration is substantial; for instance, at 1.5 *mmol*, the temperature favors the formation of crystalline fractions in PDA, while the crystalline fractions at 40 *°C* are higher than those at 25 *°C*, at 4.5 and 7.5 *mmol*. But at such TRIS concentration and 55 *°C*, the crystalline fraction is reduced at lower temperatures. It is assumed that this effect relates to the chemical kinetics of PDA synthesis; at low TRIS concentration, the effect of temperature is directly proportional to the crystalline fraction. On the contrary, this relationship changes when TRIS concentration increases to 7.5 *mmol*, which modifies the rate constant, **Figure 19A**. According to Yu, X. et al. [57], there are more stacking layers on the shell than in the inner of PDA particles, which could be affected by the inhibition/termination or Ostwald ripening process on the surface of particles during the growth stage.

A correlation between the endothermal transition and inner water molecules in the microstructure also can be established in the 100 - 240 *°C* range, where the melting of crystalline regions of PDA led to water molecules—from reaction media—being released. Nonetheless, the enthalpy associated with this process is much lower than the related melting enthalpy [109], [119].

Figure 19B illustrates the correlation between the synthesis and melting temperature, where most crystalline regions disappear; this also depends on crystallite defects or size. Results for 4.5 *mmol* TRIS show a minimum effect of the temperature on the melting point; that means greater homogeneity of the crystalline regions or a reduced number of crystal defects. When the polymer is heated, the chains move gradually as temperature increases and the crystalline domains are fused. The movement of chains depends on many aspects, like mainchain symmetry and flexibility, polarity, tacticity, type/size of side groups, and residual monomer/solvent [121]. As mentioned above, PDA is constituted by oligomers, which are made up of 2-8 monomers [90], [120], such as DHI and DA, in the beginning. It is relevant due to the rigidity of the DHI compared to DA molecules; DHI has two aromatic rings, which reduce the flexibility, while the DA has a catechol moiety and an aliphatic branch which makes its movement less restrictive. In the same way, oligomers with more monomers (e.g., 8 DHI molecules) mean a more restricted motion than smaller oligomers (e.g., 4 DHI). Results at 1.5 and 7.5 *mmol* show a considerable difference in melting temperatures but with similar tendencies; This is ascribed to different ratios of DHI/DA monomers and polymerized degree of oligomers (2-8 units) derived from synthesis conditions.

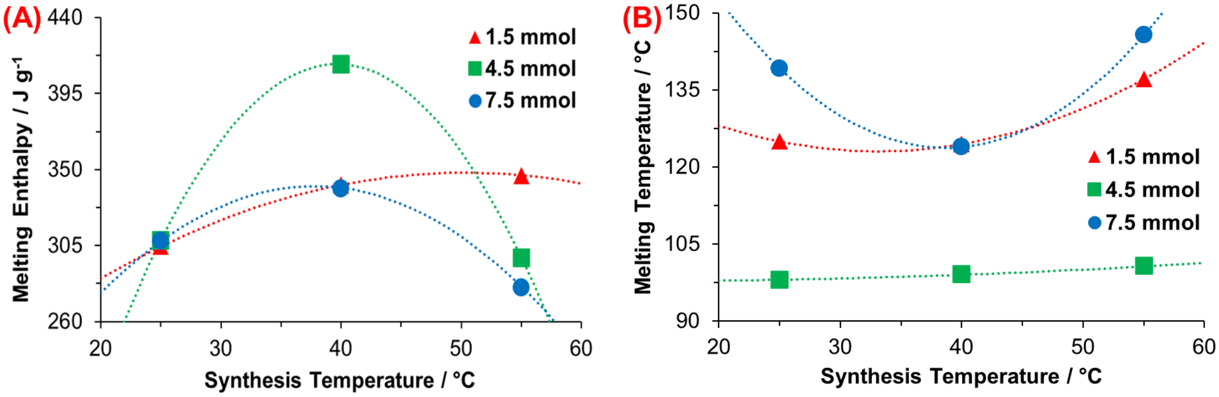

Figure 19. Relationship between the synthesis temperature and **A)** melting enthalpy and **B)** melting temperature.

3.3 Spectroscopic analysis

Infrared and Raman spectroscopies were carried out for the structural characterization to understand the effect of synthesis conditions on PDA and its influence on thermal properties and photocatalytic performance. **Figure 20** illustrates the FTIR spectra of PDA obtained at 1.5, 4.5, and 7.5 *mmol* TRIS. Firstly, the broad peak between 3200-3700 cm^{-1} is associated with the stretching of the $O - H$ and $N - H$ groups; $O - H$ is related to the catechol moiety, while $N - H$ is attributed to amine groups of 5,6-dihydroxindole and dopamine molecules in the PDA structure [63], [96]. Overlap vibrations of the benzene ring ($C = C$) and stretching vibrations of amine group bands are present at ~1573 cm^{-1}. Primary amines ($N - H$) have signals at 1550-1650 and 1050-1100 cm^{-1}, whereas secondary amines ($C - N$) is at 1500-1550 and 1100-1200 cm^{-1}. Different amines are related to the presence of DHI or DA molecules; DA has primary amines, while DHI has secondary amines. Bands between 1460 and 1340 cm^{-1} are attributed to the bending vibration of aliphatic groups ($- CH_2 -$, $C - H$) [122], [123], coming from the aliphatic branch of DA. Finally, the stretching vibration of the phenolic groups ($C - OH$) band is observed between 1230-1290 cm^{-1} [124].

Table 6 lists the ratio between primary and secondary amine intensities [125]. A ratio below unity is observed for all materials; it specifies a higher quantity of secondary amine groups, indicating a conformation based mainly on DHI monomers. The 4.5 *mmol* TRIS concentration displays the highest ratios of 1075 / 1150 cm^{-1}. A subtler difference is observed in the 1600 / 1525 cm^{-1} ratio, possibly due to the benzene ring's overlapping bands ($C = C$, 1560-1630 cm^{-1}) and amine groups. These results—in comparison with the other two concentrations—demonstrate a higher presence of DA monomers in PDA, which supports the DSC results where the aliphatic branch needs less energy to begin the movement—higher flexibility—compared to the aromatic structure of DHI—more rigid—[126], [127], which means lower melting temperatures.

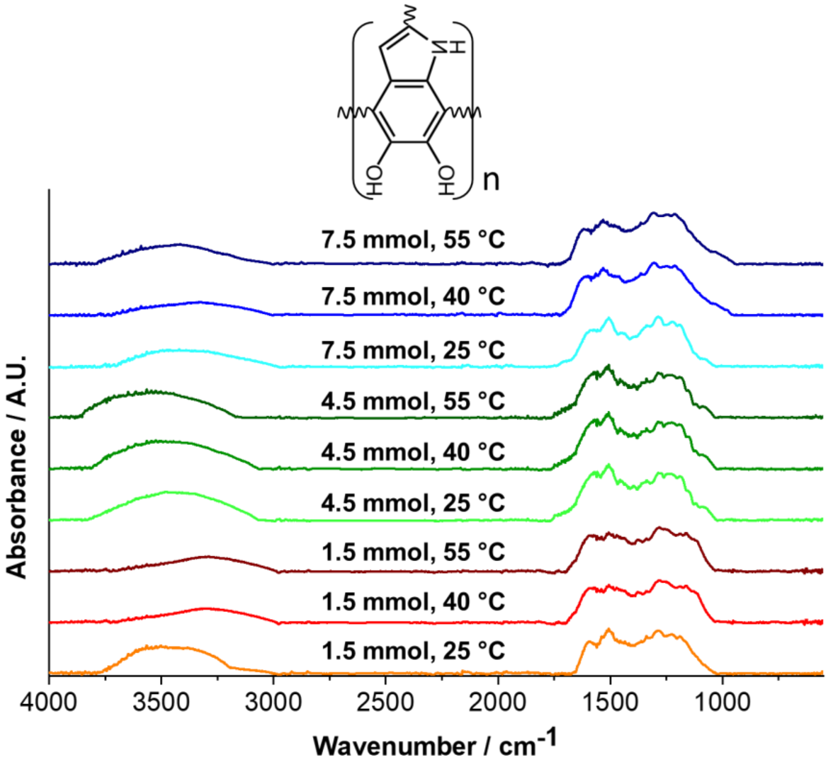

Figure 20. FT-IR spectra of PDA at each synthesis condition.

Table 6. Intensities ratio of secondary to primary amine bands measured by FT-IR.

Material		**Intensity ratio (*NH_2 / NH*)**	
		1600 / 1525	**1075 / 1150**
1.5 mmol	***25 °C***	0.72	0.24
	40 °C	0.91	0.18
	55 °C	0.92	0.23
4.5 mmol	***25 °C***	0.85	0.31
	40 °C	0.87	0.32
	55 °C	0.86	0.30
7.5 mmol	***25 °C***	0.74	0.20
	40 °C	0.84	0.20
	55 °C	0.79	0.24

On the other hand, the higher presence of secondary amine in materials obtained at 1.5 and 7.5 *mmol* TRIS is associated with favoring DA cyclization (DHI monomers). It contributes to a more rigid structure observed through the differences and higher values of melting temperatures—DSC results.

In addition, **Figure 21** displays the Raman spectra of synthesized PDA. Two distinct bands, D (amorphous band—sp^3 and H) and G (graphitic band—sp^2), are shown in all samples. The first one, the *D-band* at ~1374 cm^{-1}, and the second one, the *G-band* at ~1579 cm^{-1}, originated from linear stretching of $C-C$ bonds inside the rings and in-plane stretching of the aromatic rings [115], [128], respectively. The intensity ratio (I_D / I_G) is utilized to identify the degree of defects in a material where a low ratio indicates a low number of defects; consequently, the material presents a more graphitic structure with an sp^2 phase. The I_D / I_G ratio for 1.5 and 7.5 *mmol* TRIS displays similar values. These were below the unity meaning the predominance of the graphite-like structure (sp^2 bonds) associated with the $\pi - \pi$ stacking layers model as has been proposed for PDA. On the other hand, higher values of the I_D / I_G ratio at 4.5 *mmol* reveal a lower graphite-like arrangement.

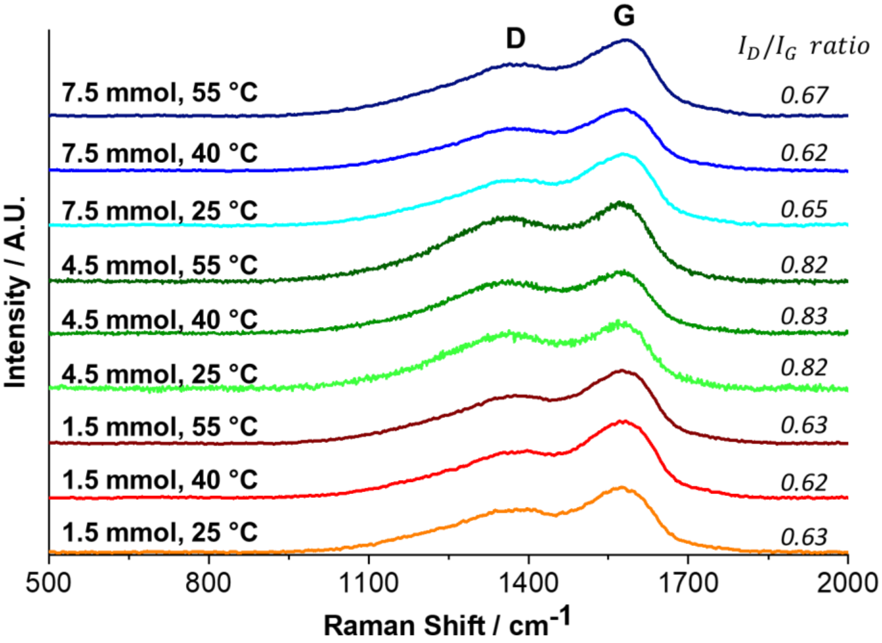

Figure 21. Raman spectra of PDA at each synthesis condition.

Notwithstanding, a specific analysis of the position of the *G-band* indicates a gradual blue shift, **Figure 22**. According to Li, H. *et al.* [113], the change of the *G-band* (toward blue) is associated with carbonized PDA, where the amorphous carbon structure of PDA is converted to nanocrystalline graphite. The PDA synthesized here was not carbonized, but a relationship was established between the synthesis temperature and the blue shift. Thus, it is assumed that the synthesis temperature can also affect the PDA structure.

In particular, the low positions of the *G-bands* and the high I_D / I_G ratio for materials obtained at 4.5 *mmol* TRIS concentration compared with the other two concentrations could be explained due to the presence of DA monomers. Monomers constituted by DHI molecules are planar structures with $\pi - \pi$ bonds (sp^2 hybridization), allowing monomers to stack in a graphitic-like structure. Nevertheless, when DA molecules are part of oligomers, the presence of $\pi - \pi$ bonds are reduced, and sp^3 hybridization (characteristic hybridization of amorphous carbon material) increases [129].

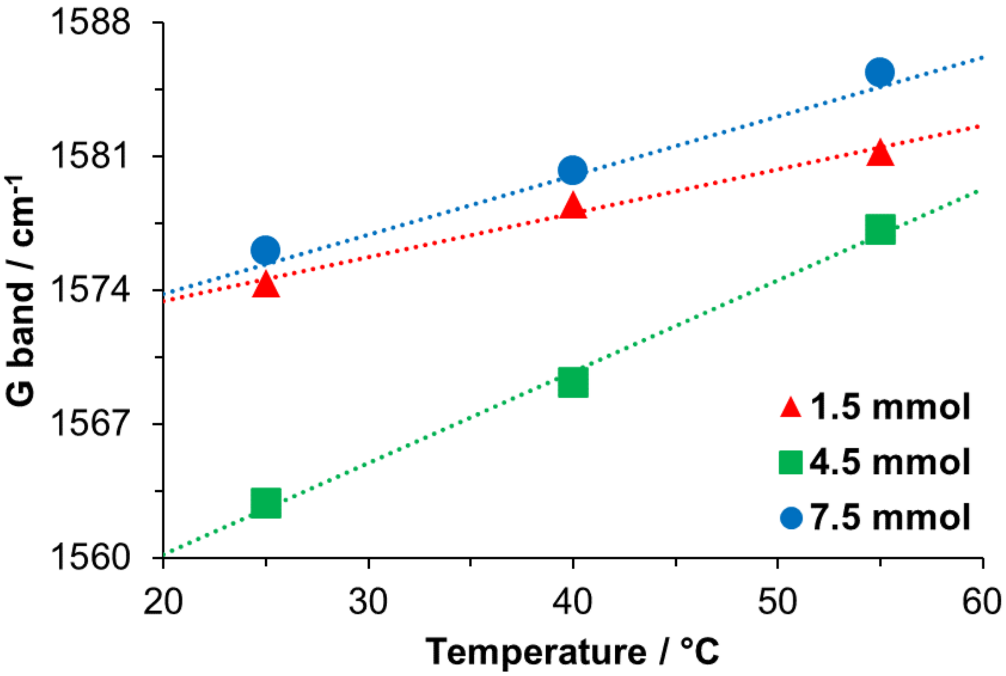

Figure 22. Relationship between the temperature of the reaction and the G band position.

3.4 X-ray diffraction analysis

The X-Ray diffraction analysis was used to carry out a microstructural analysis of PDA, see **Figure 23**. PDA is a material composed of oligomers which in turn are mainly composed of DHI molecules that make up graphitic-like structures by $\pi - \pi$ stacked. The peak center of XRD spectra is located between 21.6° and 23.4° (*2θ*), with variation in the distance of the layers between 3.4 and 4.1 *Å*, which could be mainly associated with the synthesis media molecules trapped between them [90], [114], [130].

The center peak of PDA spectra for all materials was located at 23.1° ± 0.1 (*2θ*), which indicates a typical graphitic-like structure and suggests a *d-spacing* of ~3.4 *Å*. No effect from the synthesis conditions is observed for the XRD spectra; it can be associated with the reaction media since the water was used as the solvent.

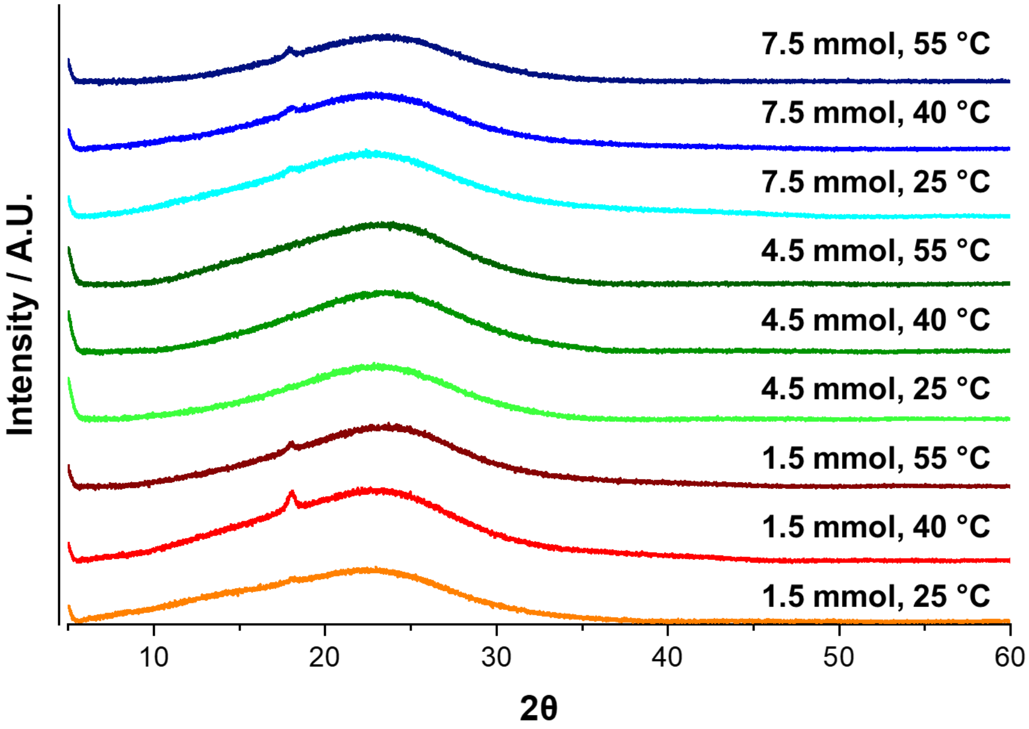

Figure 23. X-Ray diffraction spectra of PDA for each synthesis condition.

Figure 24 shows the two most used monomers to explain the PDA structure and its stacking as a graphitic-like structure. **Figure 24A** presents an oligomer formed by four DHI molecules and their different oxidized forms; this cyclic model (Cyclotetramer) proposed by Meng and Karixas has been obtained through density functional theory (DFT) calculations, and despite explaining the optical absorption of natural melanin and PDA, it has not been experimentally proven [79]. On the other hand, **Figure 24B** illustrates the PDA monomer structure based on spectroscopic and DFT results, which is the Liebscher model [131]. In this model, the composition of oligomers is formed by a mixture of indole units with different unsaturation degrees (DHI and its oxidized forms) and open-chain dopamine units (DA) united covalently by carbon atoms in the 4 and 7 positions; related results that support the presence of PDA chains of this kind were also reported by P. Delparastan et al. [132], where in addition the interactions between chains have been identified as reversible non-covalent interactions.

According to the obtained results from the thermal and spectroscopic analysis, the presence of DA units in the PDA chains has been inferred; consequently, the noncyclic model adjusts and describes the observed properties of the PDA (**Figure 24A**). Finally, **Figure 24B** shows the stacking structure of PDA chains with a *d-spacing* of ~3.4 *Å* supported by the $\pi - \pi$ interactions.

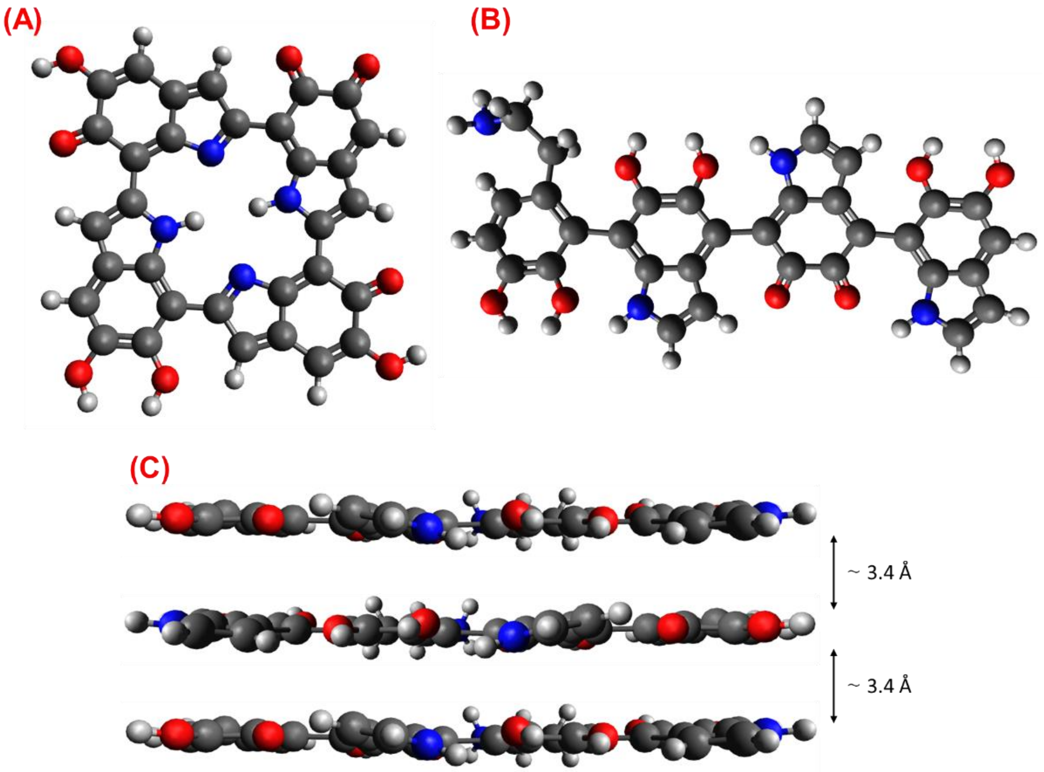

Figure 24. Representation of monomer proposed by **A)** Meng and Karixas, **B)** Liebscher, and **C)** Three-layer stacked model for PDA. Atoms color: Black, blue, red, and white for Carbon, Nitrogen, Oxygen, and Hydrogen, respectively.

CHAPTER IV: PROPERTIES OF THE PDA FOR THE REMOVAL OF CONTAMINANTS IN WATER

4.1 Photocatalytic activity evaluation of polydopamine

Environmental pollution has increased due to human progress and the increment of economic activities. One of the most dangerous impacts is the contamination of freshwater by dyes [133] due to their high toxicity and potentially carcinogenic effect. Thus they are related to environmental degradation and diseases in humans and animals [134]. Consequently, several materials have been developed to increase their capacity to remove pollutants from the environment; PDAs have played a significant role in designing materials with improved properties for this purpose [20], [135], [136].

Despite the use and study of PDA in composite materials, the effect of the synthesis conditions on the properties of PDA for removing dyes in water has been little studied. In response to this situation, the removal capability of PDAs in relationship with their synthesis conditions has been studied.

Figure 25A displays the obtained UV-Vis spectra of RhB to calculate its concentration at different times—every hour. As it shows, the absorbance decrease as time passes, which indicates the removal of RhB from water. **Figure 25B** shows the lineal fitting for different RhB concentrations; the curve equation was obtained to calculate the RhB concentration with an R^2 of 0.9935.

Figure 26 shows the profiles of photolysis, adsorption, and PDA photoactivity under visible light for RhB with the PDA synthesized with 1.5 *mmol* TRIS. The RhB is shown in the red line; it began to decrease at 180 minutes of irradiation to reach 7.60 % of RhB removal at 360 minutes, which is a low percentage.

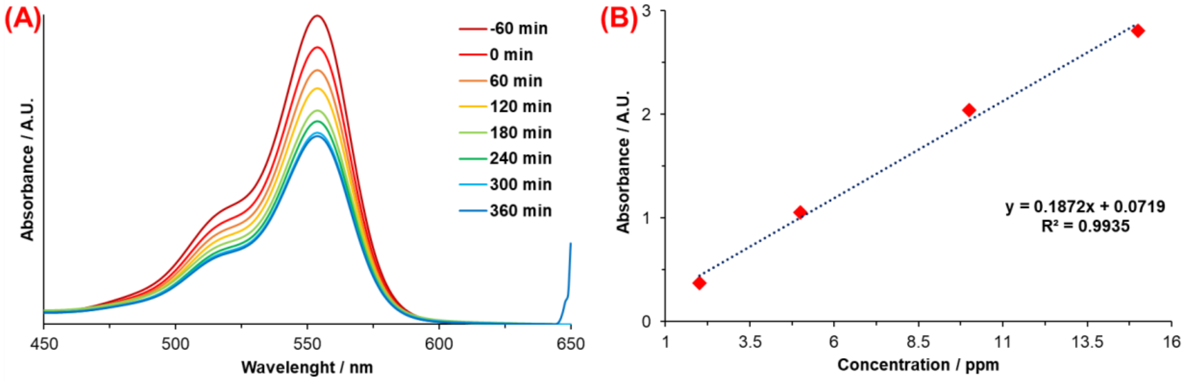

Figure 25. A) UV-Vis spectra of RhB concentration at different times for PDA obtained at 1.5 *mmol* TRIS and 25 *°C* irradiated with visible light and **B)** Calibration curve used to calculate the RhB concentration.

Figure 26A displays the results obtained for the PDA synthesized with 1.5 *mmol* TRIS and 25 *°C*. The yellow curve corresponds to the RhB sorption by PDA, which reached 25.96 % after 7 hours (**Table 7**), while the photodegradation of RhB reached after six hours (with one hour in darkness)—in green color—a percentage of 15.13 %. These results confirm the semiconductor character of PDA since, under visible light, this material can generate e^-_{CB} / h^+_{VB} pairs, which gives oxidative species that cause RhB degradation.

On the other hand, **Figures 26 B** and **C** show the profiles of RhB removal through the photolysis, PDA adsorption, and photocatalytic process with the PDA sample obtained with 1.5 *mmol* Tris and temperatures of 40 and 55 *°C*, respectively.

The removal percentage by adsorption was 14.83 % and 51.09 % (**Table 7**) for PDA obtained at 40 and 55 *°C*, respectively. For PDA with 1.5 *mmol* and 40 *°C*, the removal percentage increased to 21.63 % after visible light irradiation, which means removal of 6.80 % due to its photoactivity. Nonetheless, for PDA with 1.5 *mmol* and 55 *°C*, after visible irradiation, the removal percentage changed from 52.03 % to 51.09 %, which means that PDA obtained at these conditions has no photocatalytic activity.

Table 7. RhB removal under visible light with different PDA samples.

Material		***Adsorption / %***	***Visible light / %***	***RhB removal by photoactivity (% Vis - % Ads)***
1.5 mmol	***25 °C***	25.96	41.09	15.13 ± 1.38
	40 °C	14.83	21.63	6.80 ± 1.38
	55 °C	52.03	51.09	-0.94 ± 1.38
4.5 mmol	***25 °C***	19.57	18.82	-0.75 ± 1.38
	40 °C	47.80	44.17	-3.63 ± 1.38
	55 °C	30.22	28.45	-1.77 ± 1.38
7.5 mmol	***25 °C***	22.55	24.44	1.89 ± 1.38
	40 °C	59.35	58.41	-0.94 ± 1.38
	55 °C	61.84	58.63	-3.21 ± 1.38

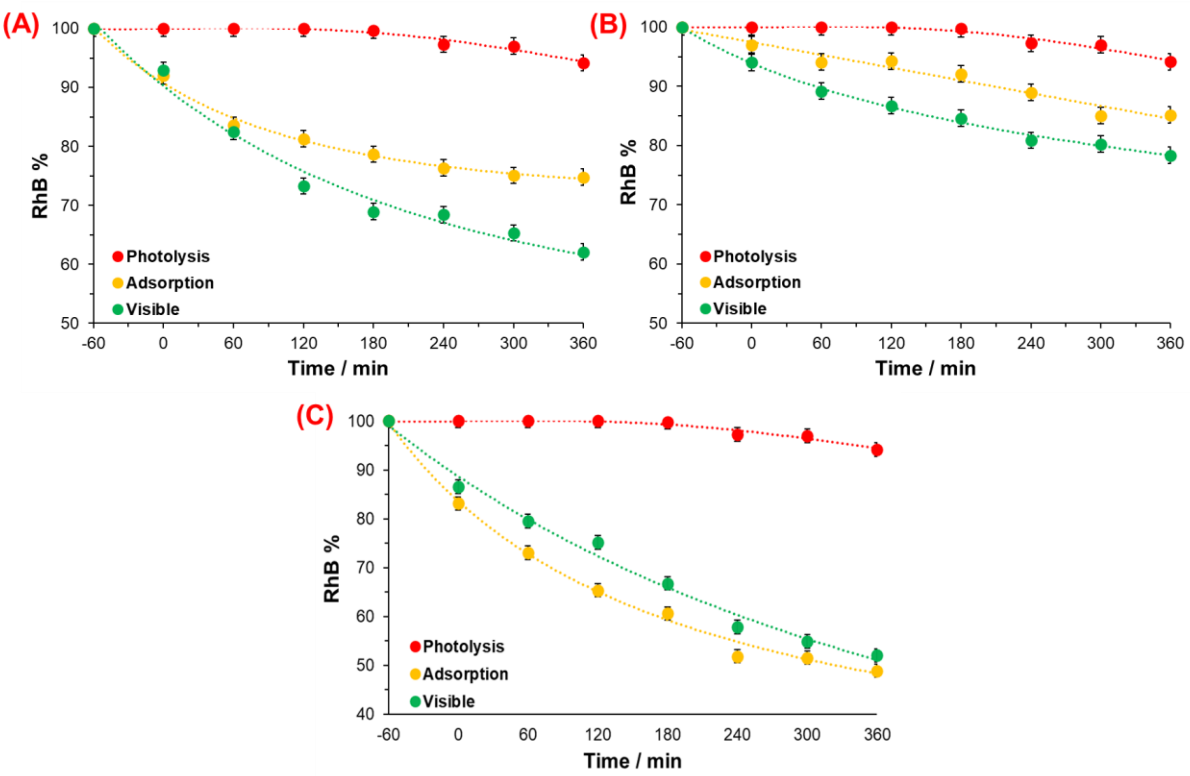

Figure 26. Removals profiles of RhB by photolysis, adsorption, and under visible light for materials obtained at 1.5 *mmol* Tris to **A)** 25, **B)** 40, and **C)** 55 *°C*.

The adsorption of RhB by PDA can be explained due to electrostatic interaction; both PDA and RhB are zwitterionic compounds [63], [137]. It implies that PDA and RhB molecules—in solution and depending on *pH*—have positive and negative charge regions, PDA from catechol moiety and secondary amine, and RhB from the carboxylic acid and ammonium cation (**Figure 27**). The adsorption and photocatalytic tests were carried out at a *pH* = 7; hence the global charge of RhB was positive [137] while PDA was negative [138]. In other words, the electrostatic interactions between the positive ammonium cation of RhB and the dissociation and deprotonation/protonation of amine and catechol groups in PDA could explain the sorption of RhB on PDA.

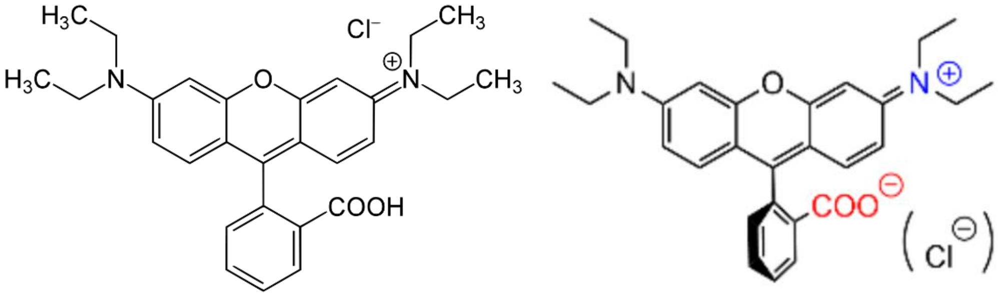

Figure 27. A) RhB molecule and **B)** prevalent charge states in RhB. The positively charged moieties are highlighted in blue, while the negatively charged are in red [137].

The different percentages of adsorption among the materials obtained at 1.5 *mmol* and three different temperatures could be explained due to the contribution of various factors. Firstly, the particle size. When the particle size is reduced, the superficial area increase, which means that more functional groups in PDA (catechol or amines) can interact with molecules of RhB and be adsorbed.

Secondly, the main functional groups of PDA. As was demonstrated above, the different synthesis conditions of DA polymerization influence the PDA composition since DA, DHI, or IDQ can constitute it; this implies that the number of catechol moieties and primary and secondary amines vary according to the synthesis conditions and, consequently the interactions with RhB molecules also change since, for instance, a secondary amine has a more nucleophilicity/basicity character than a primary amine [139], [140].

Thirdly, the $\pi - \pi$ interactions. As has been demonstrated, PDA has aromatic structures that give rise to $\pi - \pi$ systems due to carbon hybridization sp^2; in the same way, RhB molecules possess aromatic rings that contain $\pi - \pi$ systems, which can interact with each other to favor the adsorption process.

And fourthly, the crystallinity. The diffusive process through the PDA can be different in function of the crystallinity degree since RhB molecules can find a free and easy path in an amorphous structure than in a crystalline structure where the $\pi - \pi$ stacking layers are compacted and complicate the diffusion process of the molecules across the structure.

In consequence, from the results of adsorption with PDA synthesized with 1.5 *mmol* TRIS and different temperatures, the highest percentage of RhB remotion was reached with PDA obtained at 55 *°C* since this material has the smallest particle size (**Figure. 16**), moreover, the ratio intensities of NH_2/NH imply the higher presence of secondary amines in it (**Table. 6**), despite that it presents the highest enthalpy which is associated with high crystallinity, which implies regions with more compacted regions that, it seems, inhibited the photocatalytic process.

In the 1970s, McGinnes *et al*. published many works about melanin and its amorphous semiconductor character [62], [141]; since then, the scientific interest and technological applications for melanin have been increasing, at the same time, it has led to making discoveries such as the synthetic melanin or PDA. The semiconductor character of PDA allows it to have an optical band gap (E_g), like the inorganic semiconductors, where these have a VB and a CB. Analogous, organic semiconductors have two bands, HOMO and LUMO, as described in **Section 1.2.3**. According to the literature, the E_g reported for melanin is between 1.10 and 3.40 eV [13], [14], [21], [71], [83], [142] while for PDA is between 0.88 and 2.7 *eV* [71], [143]–[147]. These values of E_g mean that the energy needed to photogenerate the e^-_{CB} / h^+_{VB} pairs are contained in wavelengths from 360 to 1130 nm for melanin and from 460 to 1410 nm for PDA.

Figure 28 displays the spectrum of UV-Vis solid spectroscopy realized for PDA at 1.5 *mmol* and 25 *°C*; from the plot, *F(R)* represents the “remission” as a function of the reflectance, and energy (*eV*) is the photon's energy. E_g can be obtained when the linear fit of the straight part of the graph is extrapolated towards 0, i.e., the value of E_g is estimated at the intersection with the abscissa axis [148]. **Table 8** shows the obtained E_g for every PDA material obtained by this method. The E_g values were between 1.09 and 1.31 *eV*, meaning that all of them could have photoactivity under visible light irradiation; in other words, the energy of visible light is enough to photogenerate e^-_{CB} / h^+_{VB} pairs in PDA.

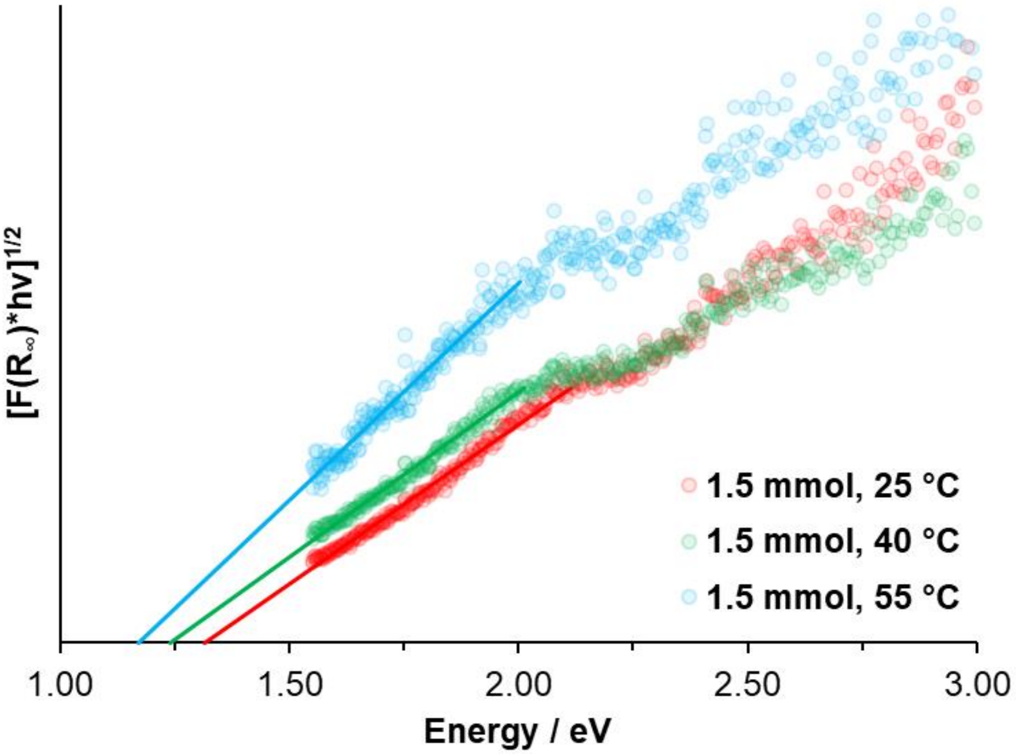

Figure 28. Band gap measurements of PDA synthesized at 1.5 *mmol* TRIS and 25, 40, and 55 *°C* by Kubelka-Munk transformed reflectance spectra.

Table 8. Calculated Band gaps for the different PDA materials.

Material		***E_g / eV***
1.5 mmol	***25 °C***	1.31
	40 °C	1.24
	55 °C	1.17
4.5 mmol	***25 °C***	1.12
	40 °C	1.26
	55 °C	1.12
7.5 mmol	***25 °C***	1.22
	40 °C	1.09
	55 °C	1.09

According to L. Miglaccio *et al*. [22], PDA photogenerate electrons react with O_2 content in the solution to form superoxide species ($O_2^{\bullet -}$) that subsequently react with the medium to form peroxide (H_2O_2). The first part of this process (generation of $O_2^{\bullet -}$) was described in **Equation 5** (**Section 1.2.1**); it requires a reduction potential of -0.33 *eV* [149], [150] to be carried out, which means that the LUMO potential of PDA must be above the reduction potential of $O_2^{\bullet -}$. Several works in literature have reported the experimental values of the HOMO and LUMO of PDA where the LUMO potential is located at -1.4 *eV* [144], [151], [152] which is enough to the photogeneration of $O_2^{\bullet -}$ species. Consequently, these radicals generated by PDA react with RhB molecules and would be responsible for their degradation.

As mentioned above, the exact structure of PDA is still unknown; nevertheless, one can guess which components of PDA must be involved in the mechanism of dye degradation.

Up to now, it is well known that PDA is constituted by chains (**Figure 24**) containing DHI and DA monomers, as well as oxidized forms of DHI like IDQ and DSQ. It is important because the different chemical composition of PDA is relevant from the point of view of its optical and electronic properties. Studies about these properties in PDA are still few; however, the study done by A. Pullman *et al*. [153] and D. S. Galvão *et al*. [154] reported, utilizing the Hückel theory, variation of E_g and LUMO values depending if IDQ, DHI, DSQ, dimers, trimers, and hexamers of IDQ conform the melanin; the computed values showed significant differences in E_g and LUMO of melanin with the different monomers that constitute it. As well as, Mohammad-Shiri *et al*. [155] reported, using DFT, the E_g and LUMO of DA to be 5.27 and -0.37 *eV*, respectively. P. Meredith *et al*. [156] reported, utilizing DFT, that DHI, DHICA, IDQ, and QI monomers have E_g of 3.61, 3.04, 2.02, and 1.12 *eV*, respectively; moreover, other work also reported the variation of E_g of DHI according with its oxidation degree—missing hydrogen atom position—, e.g., DHI has an E_g of 3.48 *eV* and DHI without hydrogen atoms in 5 and 6 positions (IDQ), has an E_g of 1.07 *eV* [157]. Y. Zou *et al*. [158] reported, through DFT, the E_g values of DHI and IDQ dimers to be 4.48 and 2.19 *eV*, respectively; in the same way, reported the LUMO values to be located at -0.53 and -3.43 *eV*, respectively. Above all, it is essential to mention that all calculus and values reported by the authors mentioned above were realized on a single monomer or, conversely, by oligomers made up of a single monomer due to the complexity of the calculations that imply different constituent monomers in oligomers.

From **Figure 26** and **Table 7**, PDA with 1.5 *mmol* TRIS and 25 *°C* have the highest photocatalytic activity since the RhB remotion increased to 15.13 % when the solution was irradiated with visible light. The photoactivity of PDA decreases according to the synthesis temperature at which the material was obtained; when PDA synthesized at 40 *°C* was evaluated, the increment of RhB removal under visible light was 6.80 %, while the PDA at 55 *°C* did not present photoactivity. It was not possible to make measurements of the HOMO and LUMO of the materials evaluated here; however, based on the obtained results and literature about E_g and LUMO computed values, herein it is speculated that the reduction in photoactivity of PDA synthesized at 40 and 55 *°C* is due to the different monomers that constitute the PDA since the LUMO is affected by its heterogeneity. If the LUMO in PDA is located below -0.33 *eV*—the reduction potential to $O_2^{\bullet -}$ photogeneration—oxidizing species will not be generated, which consequently causes RhB degradation will not take place. This assumption is based on the LUMO values reported in the literature (**Table 9**); as is observed, just DA and DHI dimer LUMO values are above the reduction potential of the $O_2{}^{\bullet -}$. On the other hand, the LUMO of DA is high enough for the $O_2{}^{\bullet -}$ photogeneration. Nonetheless, its E_g is located at 5.27 *eV*, meaning visible light energy does not have enough energy to photogenerate e^-_{CB} / h^+_{VB} pairs.

Table 9. LUMO values reported in the literature. For reference [143] and [153], the used value of β was -0.87 *eV* [159].

Monomer	***LUMO / eV***	***Reference***
DA	-0.370	[155]
IDQ	0.163	[153]
SQ	-0.049	[154]
IDQ dimer	-0.044	[154]
IDQ trimer	-0.045	[154]
IDQ hexamer	-0.045	[154]
DHI	0.861	[154]
DHI dimer	-0.530	[158]
IDQ dimer	-3.430	[158]
PDA	-1.400	[144], [151], [152]

Figure 28 displays the plots of the RhB removal by PDA synthesized at 4.5 and 7.5 *mmol* TRIS and different temperatures (25, 40, and 55 *°C*). The profiles of RhB remotion of the adsorption process and photocatalytic activity under visible light have a very similar performance during all reaction times. This similarity could be explained due to minimal or no photocatalytic activity by PDA since oxidizing species are not generated. Consequently, the RhB molecules are not degraded, just adsorbed. The RhB remotion by PDA adsorption was 19.57, 47.80, and 30.22 %, with obtained PDA at 25, 40, and 55*°C* and 4.5 *mmol* TRIS, respectively, as long as the removal percentage with PDA irradiated under visible light was 18.82, 44.17 and 28.45 %.

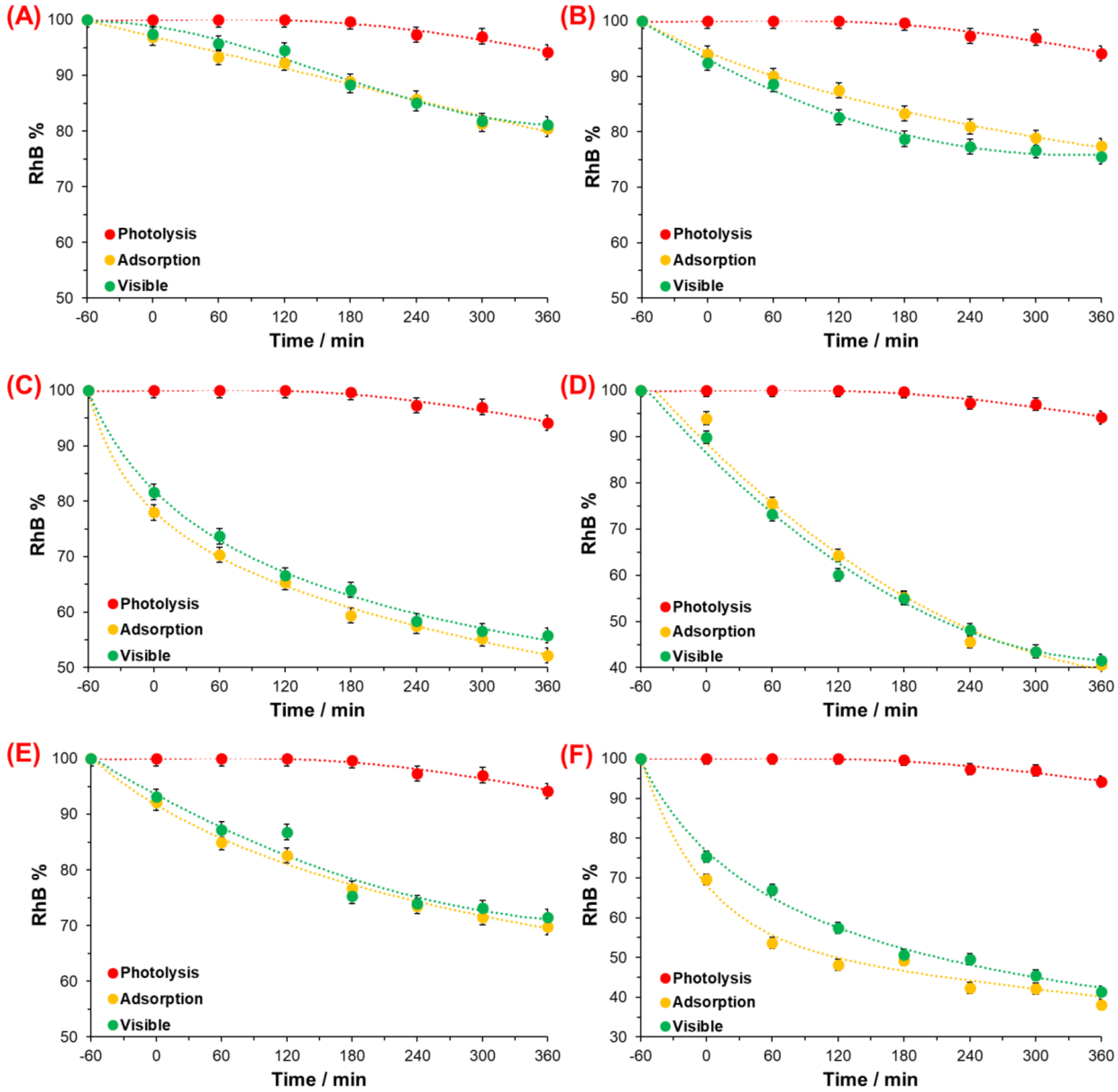

Figure 29. Removals profiles of RhB by photolysis, adsorption, and under visible light for materials obtained at 4.5 *mmol* TRIS to ***A)*** 25, ***C)*** 40, and ***E)*** 55 °*C*; and at 7.5 *mmol* TRIS to ***B)*** 25, ***D)*** 40, and ***F)*** 55 °*C*.

On the other hand, materials obtained with 7.5 *mmol* TRIS and 25, 40, and 55 °*C* also display similar profiles during RhB removal to finish with a very close percentage; 22.55, 59.35, and 61.84 % was the removal capability by adsorption process of these materials, respectively. When the reaction was carried out under visible light, the RhB removal after 6 hours was 24.44, 58.41, and 58.63 % for PDA synthesized at 25, 40, and 55 °*C*, respectively.

From the adsorption results obtained from all evaluated materials, it is problematic to establish a clear correlation between its adsorption capacity and properties. As mentioned above, four factors influence the adsorption capacity of PDA; from these, $\pi - \pi$ interactions seem to have a higher effect due to the sp^2 hybridization of PDA and RhB. The *G-band* (graphitic band) position from Raman results showed that some PDA materials have a gradual blue shift; this shift is influenced by the synthesis condition and is associated with a more graphitic structure of PDA due to the presence of sp^2 hybridization. For PDAs obtained at 1.5 *mmol* Tris at 55 *°C* and 7.5 *mmol* TRIS at 40 and 55 *°C*, the *G-band* was located at 1581.2, 1580.3, and 1585.4, respectively. These positions, which were the highest, matched with the highest RhB removal percentages, which were 51.09, 59.35, and 61.84 %, respectively. These matches indicate that the $\pi - \pi$ systems in PDA and RhB are relevant in removing pollutants from water.

PDAs obtained with 4.5 and 7.5 *mmol* TRIS (25, 40, and 55 *°C*) showed no photocatalytic activity. The adsorption profiles in darkness and under visible irradiation were almost identical, which means that during visible irradiation, just was carried out the RhB adsorption. As was discussed above, it could be associated with the LUMO position; even though the computed E_g for all materials (**Table 8**) is low enough that the visible light energy photogenerates the e^-_{CB} / h^+_{VB} pairs in the PDA. If the LUMO potential is not above the reduction potential of $O_2/O_2^{\bullet -}$, the species responsible for the RhB degradation will not be generated. Consequently, only the adsorption process will be carried out, as observed in **Figure 29**.

4.2 Polydopamine photoactivity mechanism

As has been described in **Section 1.2.1**, when an organic or inorganic semiconductor is irradiated with photons, and these have enough energy—equal to or greater than its band gap energy—photocatalytic reactions are started for the photogeneration of h^+_{VB} and e^-_{CB}. It implies the promotion of an electron from the valence band to the conduction band due to electrons' adsorption of phonon energy, as equation 1 indicates. Consequently, if the charge separation is maintained, the electron and hole may travel to the semiconductor surface, where they participate in redox reactions with sorbed species (equations 2-5) [160]. On the one hand, the photogenerated h^+_{VB} could react directly with the sorbed pollutant causing its degradation (**Equation 2**), or can be used in the photogeneration of $OH^\bullet$ radicals as shown in equation 3; at the same time, these $OH^\bullet$ radicals could react with the pollutant to degrade it (**Equation 4**). On the other hand, photogenerated e^-_{CB} can produce $O_2^{\bullet -}$ radicals (according to **Equation 5**) that subsequently react with the pollutant and degrade it [161].

Tests in the presence of scavengers were conducted to understand the photocatalytic mechanism through which PDA generates oxidant species, and RhB is removed from the water. **Figure 30** displays the profiles of RhB removal in the presence of PDA obtained at 1.5 *mmol* TRIS and 25 *°C* due to its photoactivity. The photocatalytic reaction was carried out in the presence of scavengers such as methanol and silver nitrate to trap the photogenerated holes and electrons, respectively. As shown in the RhB removal profiles, using either of the scavengers causes an increment in the removal percentage.

Methanol (CH_3OH) was used as a scavenger to identify if the photocatalytic degradation is carried out mainly by holes due to the possible following two reaction routes:

1. The methanol molecules could be sorbed on the surface of the semiconductor, and these can react with the photogenerated h^+_{VB}, which oxidizes and promotes methanol degradation, **Equation 20**.
2. Methanol molecules in the aqueous media react with the photogenerated free $OH^\bullet$ radicals (from **Equation 3**), **Equation 21** [162].

$$h_{VB}^{+} + CH_3OH \rightarrow CH_2OH^{\bullet} + H^{+} \qquad \textbf{20}$$

$$CH_3OH + OH^{\bullet} \rightarrow CH_2OH^{\bullet} + H_2O \qquad \textbf{21}$$

On the other hand, silver nitrate was used to identify if the mechanism is carried out mainly by the photogenerated electrons due to the reaction between e_{CB}^{-} and Ag^{+}, according to **Equation 22**.

$$Ag^{+} + e_{CB}^{-} \rightarrow Ag^{0} \qquad \textbf{22}$$

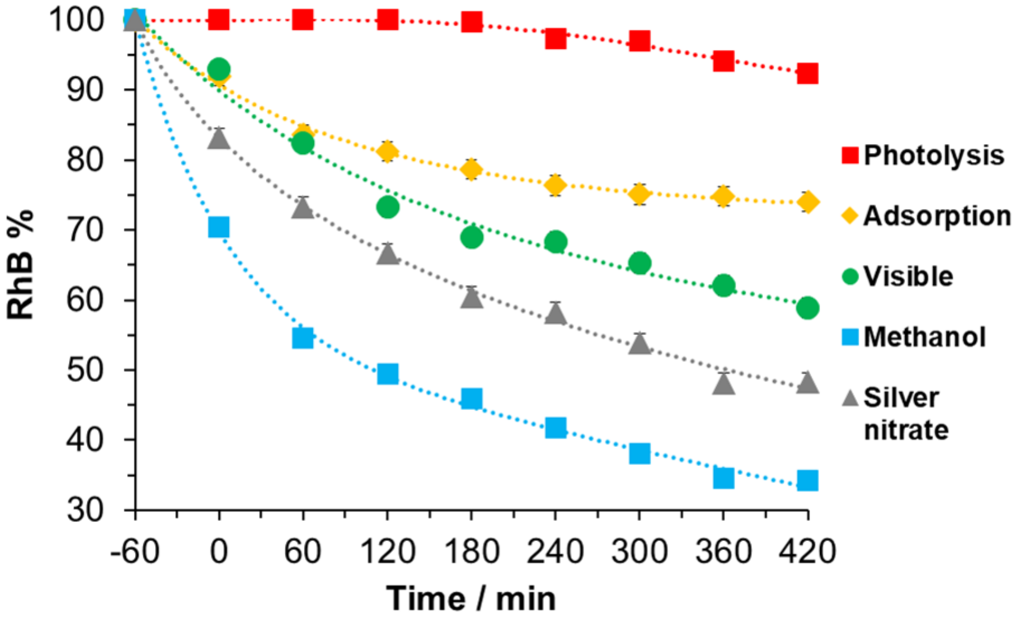

Figure 30. Removals profiles of RhB by photoactivity under visible light in the presence of holes and electrons scavengers for PDA obtained with 1.5 *mmol* TRIS and 25 *°C*.

From RhB removal profiles, PDA reaches 25.96 % by adsorption, and this removal increased by 15.13 % when the reaction was carried out under visible light. When methanol and silver nitrate were utilized as scavengers, the total removal after 7 hours of irradiation was 65.78 and 51.20 % (an increment of 24.69 and 10.11 % in comparison without scavengers), respectively. It indicates that the photogenerated electrons are the primary mechanism through which PDA removes RhB from water. The methanol effect was associated with a faster and higher RhB removal since the concentration decreased to 34.22 % during visible light irradiation. Methanol is a well-known hole and free hydroxyl radicals scavenger; this effect suggests that when methanol molecules react with holes (**Equation 20**) or $OH^{\bullet}$ radicals (**Equation 21**), the lifetime of e^{-}_{CB} photogenerated is extended (less recombination rate). These electrons have more time to react with dissolved molecular oxygen—a good electron scavenger—according to **Equation 5** in **Section 1.2.1**, producing superoxide radicals ($O_2^{\bullet -}$), which subsequently react with RhB molecules to be degraded.

On the other hand, the silver nitrate (Ag^{+}) effect is described by **Equation 22**; it implies that in the presence of Ag^{+} cations, electrons react with these to form metallic silver. In other words, the photogenerated e^{-}_{CB} is consumed to generate Ag^{0} instead of O_2•⁻, which should inhibit the RhB degradation. Nevertheless, the profile of the PDA reaction in the presence of silver nitrate displays an increment in the RhB removal, reaching 51.20 % after visible irradiation (10 % more removal than without scavenger).

The literature reports PDA's metal ions chelation properties since its structure contains catechol moieties interacting with cations like Cu^{2+}, Fe^{2+}, Fe^{3+}, Mn^{2+}, Zn^{2+}, etc. [103], [163]. In the same way, PDA's ability to spontaneously reduce silver cations is reported [164]–[166]. Ag^{+} interacts with these catechols groups through electrostatic interactions and is reduced by them; hydroxyl groups in catechol moieties are oxidized to form quinone, generating two e^{-} and two H^{+}, as shown in **Figure 8**, and these electrons are used to reduce the cations to metallic silver. It is assumed that this phenomenon is carried out during adsorption time in darkness before visible light irradiation, which creates particles of metallic silver on the PDA surface. Consequently, when the solution is irradiated with visible light, PDA photo-generates e^{-}_{CB} / h^{+}_{VB} pairs where electrons (e^{-} and e^{-}_{CB}) are used to reduce more Ag^{+} to elemental metal, which in turn reduces the recombination time of the photogenerated e^{-}_{CB} / h^{+}_{VB} [167] since the metallic silver deposited on the PDA surface acts as a trap to new photoexcited electrons due to the metallic bond of silver. This effect of high entrapment of electrons could explain the RhB remotion from the solution when Ag^{+} was used as a scavenger.

XRD analysis was carried out to bear out the presence of metallic silver on the PDA. **Figure 29** presents the PDA spectra after photocatalytic evaluation. The XRD pattern shows a peak at 23.1° 2θ associated with the PDA structure and five well-defined peaks located at 38.04°, 44.20°, 64.39°, 77.32°, and 81.50° in 2θ that correspond to (111), (200), (220), (220), (311), and (222), respectively [168]. These were indexed with the Bragg reflection numbers corresponding to the face-centered cubic structure of silver, confirming the reduction of silver cations on PDA.

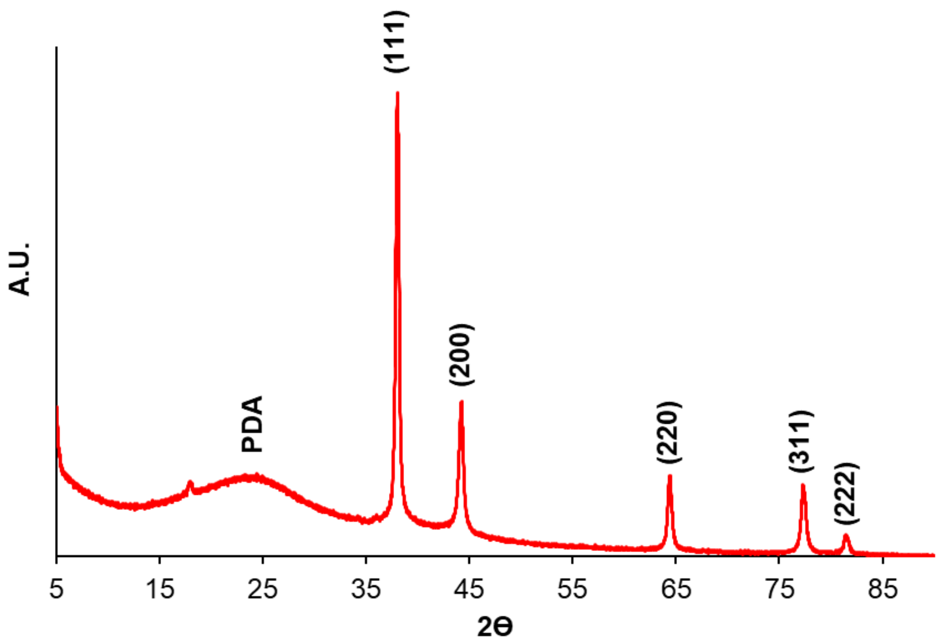

Figure 31. XRD spectra of PDA after visible light irradiation in RhB-AgNO$_3$ solution.

In summary, using PDA as a photocatalyst for RhB removal follows a mechanism where photogenerated electrons are responsible for RhB degradation since these electrons reduce the dissolved oxygen to form superoxide radicals, which could form peroxide (**Equation 23** [161]). Peroxide would be responsible for RhB molecule degradation.

$$e_{CB}^{-} + O_2^{\bullet -} + 2H^{+} \rightarrow H_2O_2 \qquad \textbf{23}$$

CONCLUSIONS

Based on the obtained results and their discussion, several conclusions can be stated as follows:

1 The synthesis of polydopamine carried out at temperatures higher/equal to 55 °C and TRIS concentrations equal to 7.5 *mmol* may inhibit the reaction, decreasing the yield of the reaction.
2 The temperature and TRIS concentration define the polydopamine particles' morphology and size.
3 The ratio of primary to secondary intensities of polydopamine observed by infrared spectroscopy allows to identify if the material is mainly constituted by dopamine or dihydroxyindole monomers. It is possible to establish if the synthesized polydopamine is primarily formed by dopamine or dihydroxyindole moieties by the primary to secondary amines ratio evaluated by infrared spectroscopy.
4 Unlike what is reported in the literature, the synthesized polydopamine exhibits melting of regular zones (crystallinity). Thus, the synthesis conditions affect the monomer stacking during the polymerization, giving regular zones into the polydopamine.
5 The synthesis temperature and TRIS concentration affect the polydopamine adsorption capacity of rhodamine B, where the $\pi - \pi$ interactions play an essential role.
6 Low temperatures and TRIS concentrations in polydopamine synthesis promote the obtention of materials with photocatalytic activity under visible light.

SCIENTIFIC PRODUCTS

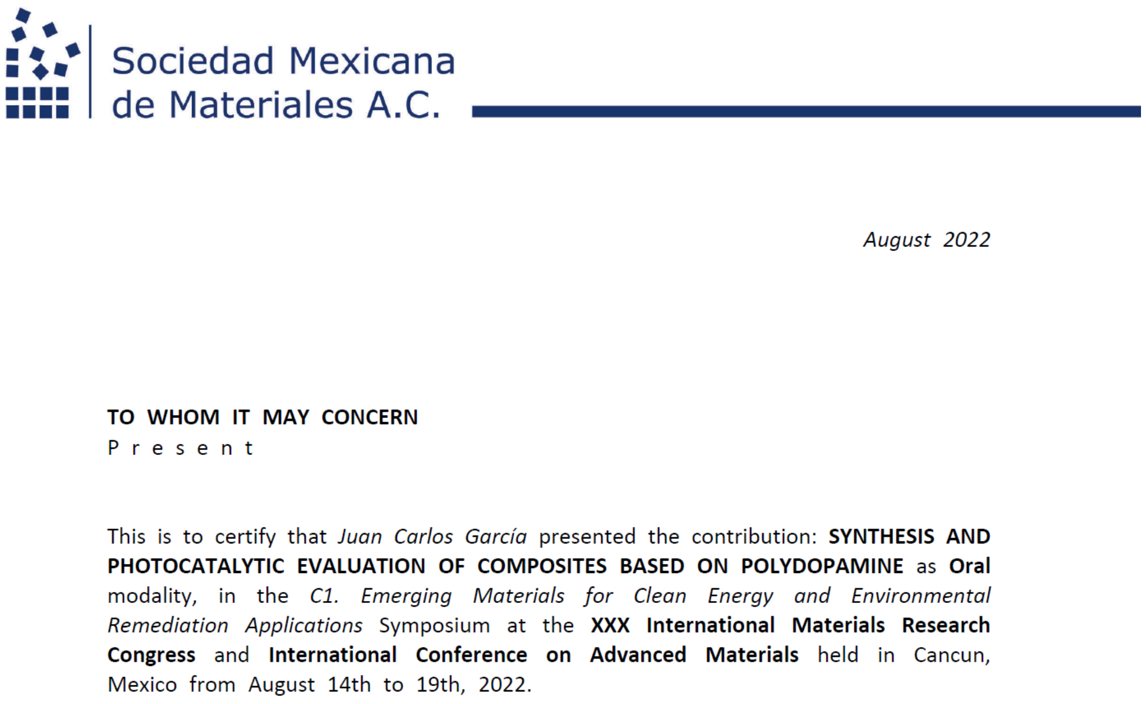

Sociedad Mexicana
de Materiales A.C.

August 2022

TO WHOM IT MAY CONCERN
Present

This is to certify that *Juan Carlos García* presented the contribution: **SYNTHESIS AND PHOTOCATALYTIC EVALUATION OF COMPOSITES BASED ON POLYDOPAMINE** as **Oral** modality, in the *C1. Emerging Materials for Clean Energy and Environmental Remediation Applications* Symposium at the **XXX International Materials Research Congress** and **International Conference on Advanced Materials** held in Cancun, Mexico from August 14th to 19th, 2022.

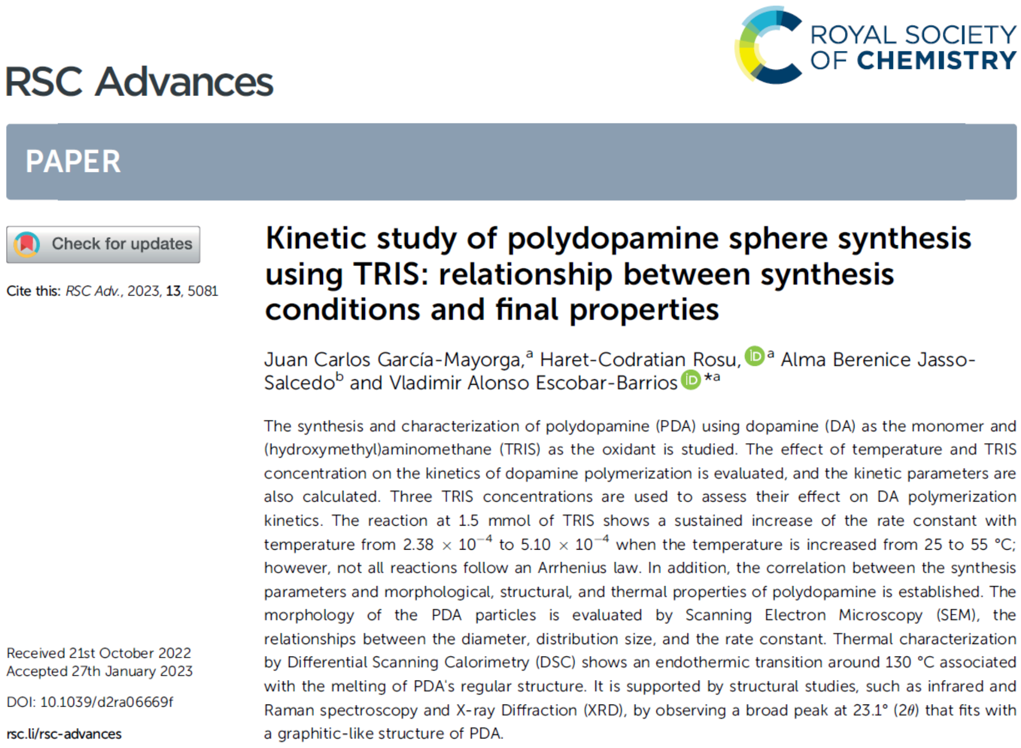

RSC Advances

ROYAL SOCIETY OF CHEMISTRY

PAPER

Check for updates

Cite this: *RSC Adv.*, 2023, **13**, 5081

Kinetic study of polydopamine sphere synthesis using TRIS: relationship between synthesis conditions and final properties

Juan Carlos García-Mayorga,[a] Haret-Codratian Rosu,[a] Alma Berenice Jasso-Salcedo[b] and Vladimir Alonso Escobar-Barrios*[a]

The synthesis and characterization of polydopamine (PDA) using dopamine (DA) as the monomer and (hydroxymethyl)aminomethane (TRIS) as the oxidant is studied. The effect of temperature and TRIS concentration on the kinetics of dopamine polymerization is evaluated, and the kinetic parameters are also calculated. Three TRIS concentrations are used to assess their effect on DA polymerization kinetics. The reaction at 1.5 mmol of TRIS shows a sustained increase of the rate constant with temperature from 2.38×10^{-4} to 5.10×10^{-4} when the temperature is increased from 25 to 55 °C; however, not all reactions follow an Arrhenius law. In addition, the correlation between the synthesis parameters and morphological, structural, and thermal properties of polydopamine is established. The morphology of the PDA particles is evaluated by Scanning Electron Microscopy (SEM), the relationships between the diameter, distribution size, and the rate constant. Thermal characterization by Differential Scanning Calorimetry (DSC) shows an endothermic transition around 130 °C associated with the melting of PDA's regular structure. It is supported by structural studies, such as infrared and Raman spectroscopy and X-ray Diffraction (XRD), by observing a broad peak at 23.1° (2θ) that fits with a graphitic-like structure of PDA.

Received 21st October 2022
Accepted 27th January 2023

DOI: 10.1039/d2ra06669f

rsc.li/rsc-advances

THANKS TO INSTITUTIONAL SUPPORTERS

This thesis was carried out in “Laboratorio de Polímeros” in “Instituto Potosino de Investigación Científica y Tecnológica S.A.” under the supervision of Dr. Vladimir Alonso Escobar Barrios.

During the realization of this thesis, the author received a scholarship from “Consejo Nacional de Ciencia y Tecnología” No. 686618.

Thanks to the technician Ana Iris Peña Maldonado and Beatriz Adriana Rivera Escoto of “Laboratorio Nacional de Investigaciones en Nanociencias y Nanotecnología (LINAN)” for the support with Scanning Electron Microscopy and X-Ray Diffraction.

The authors thank the “Laboratorio de Nuevos Materiales y Catálisis Heterogénea Ambiental (LANOCAT)” of the Advanced Materials Division of the IPICYT A.C. for facilitating the use of their facilities.

BIBLIOGRAPHY

[1] ‘Objetivos de Desarrollo Sostenible | PNUD’. https://www.undp.org/content/undp/es/home/sustainable-development-goals.html (accessed Mar. 31, 2020).

[2] ONU, ‘Resolución 64/292. El derecho humano al agua y al saneamiento’, *Asamblea General de las Naciones Unidas*, vol. 660, pp. 9–11, 2010, [Online]. Available: http://www.un.org/ga/search/view_doc.asp?symbol=A/RES/64/292&Lang=S

[3] W. Duan, F. Meng, H. Cui, Y. Lin, G. Wang, and J. Wu, ‘Ecotoxicity of phenol and cresols to aquatic organisms: A review’, *Ecotoxicol Environ Saf*, vol. 157, no. March, pp. 441–456, 2018, doi: 10.1016/j.ecoenv.2018.03.089.

[4] A. I. Stefanakis and J. A. Becker, ‘A Review of Emerging Contaminants in Water’, no. December 2015, pp. 55–80, 2017, doi: 10.4018/978-1-4666-9559-7.ch003.

[5] C. G. Joseph, G. Li Puma, A. Bono, and D. Krishnaiah, ‘Sonophotocatalysis in advanced oxidation process: A short review’, *Ultrason Sonochem*, vol. 16, no. 5, pp. 583–589, 2009, doi: 10.1016/j.ultsonch.2009.02.002.

[6] R. Ameta, M. S. Solanki, S. Benjamin, and S. C. Ameta, *Advanced oxidation processes for waste water treatment*. 2018. doi: 10.1016/B978-0-12-810499-6.00006-1.

[7] T. T. T. Dang, S. T. T. Le, D. Channei, W. Khanitchaidecha, and A. Nakaruk, ‘Photodegradation mechanisms of phenol in the photocatalytic process’, *Research on Chemical Intermediates*, vol. 42, no. 6, pp. 5961–5974, 2016, doi: 10.1007/s11164-015-2417-3.

[8] A. B. Jasso-Salcedo, G. Palestino, and V. A. Escobar-Barrios, ‘Effect of Ag, pH, and time on the preparation of Ag-functionalized zinc oxide nanoagglomerates as photocatalysts’, *J Catal*, vol. 318, pp. 170–178, 2014, doi: 10.1016/j.jcat.2014.06.008.

[9] Y. Song *et al.*, ‘Multifunctional bismuth oxychloride/mesoporous silica composites for photocatalysis, antibacterial test, and simultaneous stripping

analysis of heavy metals', *ACS Omega*, vol. 3, no. 1, pp. 973–981, 2018, doi: 10.1021/acsomega.7b01590.

[10] R. Saravanan, F. Gracia, and A. Stephen, 'Basic Principles , Mechanism , and Challenges of Photocatalysis', pp. 19–41, 2017, doi: 10.1007/978-3-319-62446-4.

[11] F. Solano, 'Melanin and melanin-related polymers as materials with biomedical and biotechnological applications—Cuttlefish ink and mussel foot proteins as inspired biomolecules', *Int J Mol Sci*, vol. 18, no. 7, 2017, doi: 10.3390/ijms18071561.

[12] S. Ito and K. Wakamatsu, 'Quantitative Analysis of Eumelanin and Pheomelanin in Humans, Mice, and Other Animals: a Comparative Review', *Pigment Cell Res*, vol. 16, pp. 523–531, 2003, doi: https://doi.org/10.1034/j.1600-0749.2003.00072.x.

[13] T. Ligonzo *et al.*, 'Electrical and optical properties of natural and synthetic melanin biopolymer', *J Non Cryst Solids*, vol. 355, no. 22–23, pp. 1221–1226, 2009, doi: 10.1016/j.jnoncrysol.2009.05.014.

[14] M. Abbas *et al.*, 'Structural, electrical, electronic and optical properties of melanin films', *European Physical Journal E*, vol. 28, no. 3, pp. 285–291, 2009, doi: 10.1140/epje/i2008-10437-9.

[15] A. Postma, Y. Yan, Y. Wang, A. N. Zelikin, E. Tjipto, and F. Caruso, 'Self-Polymerization of Dopamine as a Versatile and Robust Technique to Prepare Polymer Capsules', *Chemistry of Materials*, vol. 21, no. 14, pp. 3042–3044, 2009, doi: 10.1021/cm901293e.

[16] Y. Liu, K. Ai, and L. Lu, 'Polydopamine and Its Derivative Materials: Synthesis and Promising Applications in Energy, Environmental, and Biomedical Fields', *Chem Rev*, vol. 114, no. 9, pp. 5057–5115, 2014, doi: 10.1021/cr400407a.

[17] M. Ambrico *et al.*, 'From commercial tyrosine polymers to a tailored polydopamine platform: Concepts, issues and challenges en route to melanin-based bioelectronics', *J Mater Chem C Mater*, vol. 3, no. 25, pp. 6413–6423, 2015, doi: 10.1039/c5tc00570a.

[18] G. Siciliano *et al.*, ‘Polydopamine-Coated Magnetic Iron Oxide Nanoparticles: From Design to Applications’, *Nanomaterials*, vol. 12, no. 7. MDPI, Apr. 01, 2022. doi: 10.3390/nano12071145.

[19] X. Sun, L. Yan, R. Xu, M. Xu, and Y. Zhu, ‘Surface modification of TiO2 with polydopamine and its effect on photocatalytic degradation mechanism’, *Colloids Surf A Physicochem Eng Asp*, vol. 570, no. March, pp. 199–209, 2019, doi: 10.1016/j.colsurfa.2019.03.018.

[20] A. Mehdinia, S. Heydari, and A. Jabbari, ‘Synthesis and characterization of reduced graphene oxide-Fe3O4@polydopamine and application for adsorption of lead ions: Isotherm and kinetic studies’, *Mater Chem Phys*, vol. 239, p. 121964, Jan. 2020, doi: 10.1016/j.matchemphys.2019.121964.

[21] Y. Zou *et al.*, ‘Synthetic Melanin Hybrid Patchy Nanoparticle Photocatalysts’, *Journal of Physical Chemistry C*, vol. 123, no. 9, pp. 5345–5352, 2019, doi: 10.1021/acs.jpcc.8b10469.

[22] L. Migliaccio, M. Gryszel, V. Derek, A. Pezzella, and E. D. Głowacki, ‘Aqueous photo(electro)catalysis with eumelanin thin films’, *Mater Horiz*, vol. 5, no. 5, pp. 984–990, 2018, doi: 10.1039/c8mh00715b.

[23] J. He, Y. Lu, T. Zhao, and Y. Li, ‘Preparation of polydopamine-coated, graphene oxide/Fe3O4- imprinted nanoparticles for selective removal of sulfonylurea herbicides in cereals’, *J Sci Food Agric*, vol. 100, no. 10, pp. 3822–3831, Aug. 2020, doi: 10.1002/jsfa.10419.

[24] J. Dai *et al.*, ‘Surface modification of polypropylene with porous polyacrylamide/polydopamine composite coating’, *Mater Lett*, vol. 266, p. 127487, May 2020, doi: 10.1016/j.matlet.2020.127487.

[25] L. Jia *et al.*, ‘Polydopamine-assisted surface modification for orthopaedic implants’, *Journal of Orthopaedic Translation*, vol. 17. Elsevier (Singapore) Pte Ltd, pp. 82–95, Apr. 01, 2019. doi: 10.1016/j.jot.2019.04.001.

[26] H. Ma *et al.*, ‘Anchoring of Prussian blue nanoparticles on polydopamine nanospheres as an efficient peroxidase mimetic for colorimetric sensing’, *Colloids Surf A Physicochem Eng Asp*, vol. 577, pp. 622–629, Sep. 2019, doi: 10.1016/j.colsurfa.2019.06.035.

[27] A. Sukeri, A. Arjunan, and M. Bertotti, ‘New strategy to fabricate a polydopamine functionalized self-supported nanoporous gold film electrode for electrochemical sensing applications’, *Electrochem commun*, vol. 110, p. 106622, Jan. 2020, doi: 10.1016/j.elecom.2019.106622.

[28] Z. Jin *et al.*, ‘Preparation of doxorubicin-loaded porous iron Oxide@ polydopamine nanocomposites for MR imaging and synergistic photothermal–chemotherapy of cancer’, *Colloids Surf B Biointerfaces*, vol. 208, Dec. 2021, doi: 10.1016/j.colsurfb.2021.112107.

[29] L. Li, C. Xie, and X. Xiao, ‘Polydopamine modified TiO2 nanotube arrays as a local drug delivery system for ibuprofen’, *J Drug Deliv Sci Technol*, vol. 56, p. 101537, Apr. 2020, doi: 10.1016/j.jddst.2020.101537.

[30] U. T. Uthappa *et al.*, ‘Facile green synthetic approach of bio inspired polydopamine coated diatoms as a drug vehicle for controlled drug release and active catalyst for dye degradation’, *Microporous and Mesoporous Materials*, vol. 288, p. 109572, Nov. 2019, doi: 10.1016/j.micromeso.2019.109572.

[31] X. Zhu, H. Feng, R. Chen, Q. Liao, D. Ye, and B. Zhang, ‘Core-shell structured Pd catalyst layer encapsulated by polydopamine for a gas-liquid-solid microreactor’, *Appl Surf Sci*, vol. 487, pp. 416–425, Sep. 2019, doi: 10.1016/j.apsusc.2019.05.024.

[32] K. Zhu, H. Xu, C. Chen, X. Ren, A. Alsaedi, and T. Hayat, ‘Encapsulation of Fe0-dominated Fe3O4/Fe0/Fe3C nanoparticles into carbonized polydopamine nanospheres for catalytic degradation of tetracycline via persulfate activation’, *Chemical Engineering Journal*, vol. 372, pp. 304–311, Sep. 2019, doi: 10.1016/j.cej.2019.04.157.

[33] C. C. Ho and S. J. Ding, ‘Structure, properties and applications of mussel-inspired polydopamine’, *J Biomed Nanotechnol*, vol. 10, no. 10, pp. 3063–3084, 2014, doi: 10.1166/jbn.2014.1888.

[34] M. Salomäki, L. Marttila, H. Kivelä, T. Ouvinen, and J. Lukkari, ‘Effects of pH and Oxidants on the First Steps of Polydopamine Formation: A

Thermodynamic Approach', *Journal of Physical Chemistry B*, vol. 122, no. 24, pp. 6314–6327, 2018, doi: 10.1021/acs.jpcb.8b02304.

[35] X. Wang, Z. Chen, P. Yang, J. Hu, Z. Wang, and Y. Li, 'Size control synthesis of melanin-like polydopamine nanoparticles by tuning radicals', *Polym Chem*, vol. 10, no. 30, pp. 4194–4200, 2019, doi: 10.1039/c9py00517j.

[36] M. Wu, T. Wang, L. Müller, and F. A. Müller, 'Adjustable synthesis of polydopamine nanospheres and their nucleation and growth', *Colloids Surf A Physicochem Eng Asp*, vol. 603, no. April, p. 125196, 2020, doi: 10.1016/j.colsurfa.2020.125196.

[37] Y. Wang *et al.*, 'Effects of Melanin on Optical Behavior of Polymer: From Natural Pigment to Materials Applications', *ACS Appl Mater Interfaces*, vol. 10, no. 15, pp. 13100–13106, 2018, doi: 10.1021/acsami.8b02658.

[38] C. C. Ho and S. J. Ding, 'The pH-controlled nanoparticles size of polydopamine for anti-cancer drug delivery', *J Mater Sci Mater Med*, vol. 24, no. 10, pp. 2381–2390, Oct. 2013, doi: 10.1007/s10856-013-4994-2.

[39] N. F. della Vecchia, R. Avolio, M. Alfè, M. E. Errico, A. Napolitano, and M. D'Ischia, 'Building-block diversity in polydopamine underpins a multifunctional eumelanin-type platform tunable through a quinone control point', *Adv Funct Mater*, vol. 23, no. 10, pp. 1331–1340, Mar. 2013, doi: 10.1002/adfm.201202127.

[40] M. Zhang, L. Zhang, Y. Chen, L. Li, Z. Su, and C. Wang, 'Precise synthesis of unique polydopamine/mesoporous calcium phosphate hollow Janus nanoparticles for imaging-guided chemo-photothermal synergistic therapy', *Chem Sci*, vol. 8, no. 12, pp. 8067–8077, 2017, doi: 10.1039/c7sc03521g.

[41] M. Mohammad, F. Ahmadpoor, S. A. Shojaosadati, and E. Vasheghani-Farahani, 'Highly efficient porous magnetic polydopamine/copper phosphate with three-dimensional hierarchical nanoflower morphology as a selective platform for recombinant proteins separation', *Colloids Surf B Biointerfaces*, vol. 209, Jan. 2022, doi: 10.1016/j.colsurfb.2021.112149.

[42] 'Contaminación en México – Agua.org.mx'. https://agua.org.mx/agua-contaminacion-en-mexico/ (accessed Oct. 04, 2018).

[43] V. Sánchez, ‘Agua contaminada, una amenaza latente en México’, *Ambiente*, 2016. http://www.conacytprensa.mx/index.php/ciencia/ambiente/11179-agua-contaminada-una-amenaza-latente-en-mexico (accessed Oct. 04, 2018).

[44] ‘How Much Water is There on Earth?’ https://www.usgs.gov/special-topic/water-science-school/science/how-much-water-there-earth?qt-science_center_objects=0#qt-science_center_objects (accessed Jun. 30, 2020).

[45] S. García Liñan, ‘Contaminación del agua’, *Opinion*, 2015. http://www.elfinanciero.com.mx/opinion/salvador-garcia-linan/contaminacion-del-agua (accessed Oct. 04, 2018).

[46] G. Amaral *et al.*, ‘Estadísticas del agua en México, 2018’, *Journal of Petrology*, vol. 369, no. 1, pp. 1689–1699, 2013, doi: 10.1017/CBO9781107415324.004.

[47] I. Lira, ‘70% del agua dulce en México está contaminada, y el Gobierno deja impunes a las industrias, alertan’, *Sección México*, 2017. http://www.sinembargo.mx/14-07-2017/3260802 (accessed Oct. 04, 2018).

[48] ‘Día Mundial del Agua: Las cifras siguen siendo alarmantes’. https://www.lavanguardia.com/natural/20190322/461164578761/dia-mundial-agua-2019-cifras.html (accessed Jul. 12, 2020).

[49] N. Ross, ‘World water quality facts and statistics’, *Annual Water Review*, vol. 35, no. Who 2002, p. 109, 2008.

[50] ‘From Waste to Resource - Shifting Paradigms for Smarter Wastewater Interventions in Latin America and the Caribbean’, *From Waste to Resource - Shifting Paradigms for Smarter Wastewater Interventions in Latin America and the Caribbean*, 2019, doi: 10.1596/33385.

[51] Fao & Iwmi, ‘Water pollution from agriculture: a global review Executive summary’, *FAO and IWMI*, p. 35, 2017, [Online]. Available: http://www.fao.org/3/a-i7754e.pdf

[52] S. D. Melvin and F. D. L. Leusch, ‘Removal of trace organic contaminants from domestic wastewater: A meta-analysis comparison of sewage treatment technologies’, *Environ Int*, vol. 92–93, pp. 183–188, 2016, doi: 10.1016/j.envint.2016.03.031.

[53] S. L. Prabu, T. N. K. Suriyaprakash, and J. A. Kumar, ‘Wastewater treatment technologies: A review’, *Pharma Times*, vol. 43, no. 5, pp. 9–13, 2011.

[54] ‘Water Pollution Facts, Types, Causes and Effects of Water Pollution | NRDC’. https://www.nrdc.org/stories/water-pollution-everything-you-need-know#categories (accessed Jul. 15, 2020).

[55] R. C. Pawar and C. S. Lee, *Heterogeneous Nanocomposite-Photocatalysis for Water Purification*. 2015. doi: 10.1016/C2014-0-02650-0.

[56] J. Hagen, *Industrial Catalysis: A Practical Approach*. 2005, 2005. Accessed: Mar. 13, 2023. [Online]. Available: 10.1002/3527607684

[57] Y. Wang, J. Niu, Z. Zhang, and X. Long, ‘Sono-photocatalytic degradation of organic pollutants in water’, *Progress in Chemistry*, vol. 20, no. 10, pp. 1621–1627, 2008.

[58] Y. Zhang, M. K. Ram, E. K. Stefanakos, and D. Y. Goswami, ‘Synthesis, characterization, and applications of ZnO nanowires’, *Journal of Nanomaterials*, vol. 2012. 2012. doi: 10.1155/2012/624520.

[59] Y. Chen, W. Li, L. Li, and L. Wang, ‘Progress in organic photocatalysts’, *Rare Metals*, vol. 37, no. 1, pp. 1–12, 2018, doi: 10.1007/s12598-017-0953-2.

[60] A. Solis. Herrera, *Melanin, the Master Molecule*. Bentham Science Publishers, 2018.

[61] M. D’Ischia, A. Napolitano, A. Pezzella, P. Meredith, and T. Sarna, ‘Chemical and structural diversity in eumelanins: Unexplored bio-optoelectronic materials’, *Angewandte Chemie - International Edition*, vol. 48, no. 22, pp. 3914–3921, 2009, doi: 10.1002/anie.200803786.

[62] J. Mcginness, P. Corry, and P. Proctor, ‘Amorphous semiconductor switching in melanins’, *Science (1979)*, vol. 183, no. 4127, pp. 853–855, 1974, doi: 10.1126/science.183.4127.853.

[63] C. C. Ho and S. J. Ding, ‘Structure, properties and applications of mussel-inspired polydopamine’, *Journal of Biomedical Nanotechnology*, vol. 10, no. 10. American Scientific Publishers, pp. 3063–3084, 2014. doi: 10.1166/jbn.2014.1888.

[64] J. Li and L. Yan, ‘Fabrication of Polydopamine Coating and Its Application in Glucose Sensor’, *J Nanosci Nanotechnol*, vol. 18, no. 3, pp. 1606–1610, 2017, doi: 10.1166/jnn.2018.14243.

[65] C. Hou, H. Yu, and C. Huang, ‘ZnO:Bio-inspired polydopamine functionalized Ti3C2Tx composite electron transport layers for highly efficient polymer solar cells’, *J Alloys Compd*, vol. 900, Apr. 2022, doi: 10.1016/j.jallcom.2021.163381.

[66] H. Guo *et al.*, ‘Enhanced performance of Si/PEDOT: PSS heterojunction solar cells via multi-walled carbons coated with polydopamine’, *Opt Mater (Amst)*, vol. 120, Oct. 2021, doi: 10.1016/j.optmat.2021.111375.

[67] M. Savioli Lopes, A. L. Jardini, and R. Maciel Filho, ‘Poly (lactic acid) production for tissue engineering applications’, in *Procedia Engineering*, 2012, vol. 42, pp. 1402–1413. doi: 10.1016/j.proeng.2012.07.534.

[68] A. P. Tiwari *et al.*, ‘Polydopamine-based Implantable Multifunctional Nanocarpet for Highly Efficient Photothermal-chemo Therapy’, *Sci Rep*, vol. 9, no. 1, Dec. 2019, doi: 10.1038/s41598-019-39457-y.

[69] C. J. Houk, F. O. Beltran, and M. A. Grunlan, ‘Suitability of EtO sterilization for polydopamine-coated, self-fitting bone scaffolds’, *Polym Degrad Stab*, vol. 194, Dec. 2021, doi: 10.1016/j.polymdegradstab.2021.109763.

[70] I. R. Gentle *et al.*, ‘Role of semiconductivity and ion transport in the electrical conduction of melanin’, *Proceedings of the National Academy of Sciences*, vol. 109, no. 23, pp. 8943–8947, 2012, doi: 10.1073/pnas.1119948109.

[71] V. Capozzi *et al.*, ‘Optical and photoelectronic properties of melanin’, *Thin Solid Films*, vol. 511–512, pp. 362–366, 2006, doi: 10.1016/j.tsf.2005.12.065.

[72] O. Radicals, ‘Free radical scavenging properties of melanin interaction of eu- and pheo-melanin models with reducing and oxidising radicals’, vol. 26, no. 98, pp. 518–525, 1999.

[73] K. Patel and R. Kumar, ‘Vancomycin Grafted Polydopamine Coated Silver Nanoparticles for Enhanced Antibacterial Action Against Vancomycin-Resistant Bacteria E. Faecalis.’, *ChemistrySelect*, vol. 5, no. 15, pp. 4701–4707, 2020, doi: 10.1002/slct.202000200.

[74] Z. Wang *et al.*, ‘Protein-Affinitive Polydopamine Nanoparticles as an Efficient Surface Modification Strategy for Versatile Porous Scaffolds Enhancing Tissue Regeneration’, *Particle and Particle Systems Characterization*, vol. 33, no. 2, pp. 89–100, 2016, doi: 10.1002/ppsc.201500187.

[75] P. M. Plonka and M. Grabacka, ‘Melanin synthesis in microorganisms — biotechnological and medical aspects *’, 2006. [Online]. Available: www.actabp.pl

[76] S. Ito, ‘A chemist’s view of melanogenesis’, *Oigment Cell Research*, vol. 16, pp. 230–236, 2003, doi: https://doi.org/10.1034/j.1600-0749.2003.00037.x.

[77] U. Degli, N. Federico, and C. Organica, *Melanins and Melanogenesis*.

[78] Z. v. Bedran *et al.*, ‘Water-Activated Semiquinone Formation and Carboxylic Acid Dissociation in Melanin Revealed by Infrared Spectroscopy’, *Polymers (Basel)*, vol. 13, no. 24, Dec. 2021, doi: 10.3390/polym13244403.

[79] S. Meng and E. Kaxiras, ‘Theoretical models of eumelanin protomolecules and their optical properties’, *Biophys J*, vol. 94, no. 6, pp. 2095–2105, Mar. 2008, doi: 10.1529/biophysj.107.121087.

[80] A. Pezzella, D. Vogna, and G. Prota, ‘Synthesis of optically active tetrameric melanin intermediates by oxidation of the melanogenic precursor 5,6-dihydroxyindole-2-carboxylic acid under biomimetic conditions’, *Tetrahedron Asymmetry*, vol. 14, no. 9, pp. 1133–1140, May 2003, doi: 10.1016/S0957-4166(03)00156-3.

[81] M. D’Ischia, A. Napolitano, V. Ball, C. T. Chen, and M. J. Buehler, ‘Polydopamine and eumelanin: From structure-property relationships to a unified tailoring strategy’, *Acc Chem Res*, vol. 47, no. 12, pp. 3541–3550, 2014, doi: 10.1021/ar500273y.

[82] S. Parisi *et al.*, ‘Supplementing π-systems: eumelanin and graphene-like integration towards highly conductive materials for the mammalian cell culture bio-interface’, *J Mater Chem B*, vol. 3, no. 25, pp. 5070–5079, 2015, doi: 10.1039/c5tb00343a.

[83] E. Vahidzadeh, A. P. Kalra, and K. Shankar, ‘Melanin-based electronics: From proton conductors to photovoltaics and beyond’, *Biosens Bioelectron*, vol. 122, no. July, pp. 127–139, 2018, doi: 10.1016/j.bios.2018.09.026.

[84] C. Lee *et al.*, ‘Semiconducting Synthetic Melanin-Based Organic/Inorganic Hybrid Photoanodes for Solar Water Oxidation’, *ChemSusChem*, vol. 11, no. 19, pp. 3534–3541, 2018, doi: 10.1002/cssc.201801135.

[85] W. Xie, E. Pakdel, Y. Liang, D. Liu, L. Sun, and X. Wang, ‘Natural melanin/TiO2 hybrids for simultaneous removal of dyes and heavy metal ions under visible light’, *J Photochem Photobiol A Chem*, vol. 389, no. December 2019, p. 112292, 2020, doi: 10.1016/j.jphotochem.2019.112292.

[86] E. A. M. Basheer and H. A. Abdulbari, ‘Visible Light TiO2 Photocatalyst Composite Based on Carbon Microfiber Derived from Human Hair’, *ChemistrySelect*, vol. 3, no. 41, pp. 11687–11695, 2018, doi: 10.1002/slct.201801161.

[87] X. Zhou *et al.*, ‘Dramatic visible light photocatalytic degradation due to the synergetic effects of TiO2 and PDA nanospheres’, *RSC Adv*, vol. 6, no. 69, pp. 64446–64449, 2016, doi: 10.1039/c6ra10292a.

[88] P. Meredith and T. Sarna, ‘The physical and chemical properties of eumelanin’, *Pigment Cell Res*, vol. 19, pp. 572–594, 2006.

[89] R. Lakshminarayanan, S. Madhavi, and C. P. C. Sim, ‘Oxidative Polymerization of Dopamine: A High-Definition Multifunctional Coatings for Electrospun Nanofibers - An Overview’, in *Dopamine - Health and Disease*, InTech, 2018. doi: 10.5772/intechopen.81036.

[90] D. R. Dreyer, D. J. Miller, B. D. Freeman, D. R. Paul, and C. W. Bielawski, ‘Elucidating the structure of poly(dopamine)’, *Langmuir*, vol. 28, no. 15, pp. 6428–6435, 2012, doi: 10.1021/la204831b.

[91] J. Liebscher, ‘Chemistry of Polydopamine – Scope, Variation, and Limitation’, *European Journal of Organic Chemistry*, vol. 2019, no. 31–32. Wiley-VCH Verlag, pp. 4976–4994, Sep. 01, 2019. doi: 10.1002/ejoc.201900445.

[92] J. J. Feng, P. P. Zhang, A. J. Wang, Q. C. Liao, J. L. Xi, and J. R. Chen, ‘One-step synthesis of monodisperse polydopamine-coated silver core-shell

nanostructures for enhanced photocatalysis', *New Journal of Chemistry*, vol. 36, no. 1, pp. 148–154, 2012, doi: 10.1039/c1nj20850k.

[93] W. X. Mao *et al.*, 'Core-shell structured TiO2@polydopamine for highly active visible-light photocatalysis', *Chemical Communications*, vol. 52, no. 44, pp. 7122–7125, 2016, doi: 10.1039/c6cc02041k.

[94] X. Huang, Y. Niu, Z. Peng, and W. Hu, 'Core–shell structured BiOCl@polydopamine hierarchical hollow microsphere for highly efficient photocatalysis', *Colloids Surf A Physicochem Eng Asp*, vol. 580, no. July, p. 123747, 2019, doi: 10.1016/j.colsurfa.2019.123747.

[95] V. Ball, D. del Frari, V. Toniazzo, and D. Ruch, 'Kinetics of polydopamine film deposition as a function of pH and dopamine concentration: Insights in the polydopamine deposition mechanism', *J Colloid Interface Sci*, vol. 386, no. 1, pp. 366–372, Nov. 2012, doi: 10.1016/j.jcis.2012.07.030.

[96] Douglas A. Skoog, *Principios de Análisis Instrumental*, Sexta. México, 2008.

[97] J. D. Simon, 'Spectroscopic and dynamic studies of the epidermal chromophores trans- urocanic acid and eumelanin', *Acc Chem Res*, vol. 33, no. 5, pp. 307–313, 2000, doi: 10.1021/ar970250t.

[98] R. Micillo *et al.*, 'Eumelanin broadband absorption develops from aggregation-modulated chromophore interactions under structural and redox control', *Sci Rep*, vol. 7, Feb. 2017, doi: 10.1038/srep41532.

[99] A. Solís-Herrera, C. María del Carmen Arias Esparza, R. I. Solís-Arias, P. E. Solís-Arias, and M. P. Solís-Arias, 'The physical and chemical properties of eumelanin', *Biomedical Research*, vol. 21, no. 2, pp. 224–226, 2010, doi: 10.1111/j.1600-0749.2006.00345.x.

[100] N. F. della Vecchia *et al.*, 'Tris buffer modulates polydopamine growth, aggregation, and paramagnetic properties', *Langmuir*, vol. 30, no. 32, pp. 9811–9818, Aug. 2014, doi: 10.1021/la501560z.

[101] Ira N. Levine, 'Principios de fisicoquímica', 2014. [Online]. Available: https://www.facebook.com/pages/Interfase-

[102] C. Zhao, F. Zuo, Z. Liao, Z. Qin, S. Du, and Z. Zhao, 'Mussel-inspired one-pot synthesis of a fluorescent and water-soluble polydopamine-polyethyleneimine

copolymer', *Macromol Rapid Commun*, vol. 36, no. 10, pp. 909–915, May 2015, doi: 10.1002/marc.201500021.

[103] Z. Wang *et al.*, 'Tunable, Metal-Loaded Polydopamine Nanoparticles Analyzed by Magnetometry', *Chemistry of Materials*, vol. 29, no. 19, pp. 8195–8201, 2017, doi: 10.1021/acs.chemmater.7b02262.

[104] K. Y. Ju, Y. Lee, S. Lee, S. B. Park, and J. K. Lee, 'Bioinspired polymerization of dopamine to generate melanin-like nanoparticles having an excellent free-radical-scavenging property', *Biomacromolecules*, vol. 12, no. 3, pp. 625–632, 2011, doi: 10.1021/bm101281b.

[105] 'Correlation between pre-exponential factor and activation energy of isoamyl alcohol hydrogenolysis on platinum catalysts'.

[106] N. Katada, S. Sota, N. Morishita, K. Okumura, and M. Niwa, 'Relationship between activation energy and pre-exponential factor normalized by the number of Brønsted acid sites in cracking of short chain alkanes on zeolites', *Catal Sci Technol*, vol. 5, no. 3, pp. 1864–1869, Mar. 2015, doi: 10.1039/c4cy01483a.

[107] S. G. Kwon and T. Hyeon, 'Formation mechanisms of uniform nanocrystals via hot-injection and heat-up methods', *Small*, vol. 7, no. 19. pp. 2685–2702, Oct. 04, 2011. doi: 10.1002/smll.201002022.

[108] V. K. Thakur, M. F. Lin, E. J. Tan, and P. S. Lee, 'Green aqueous modification of fluoropolymers for energy storage applications', *J Mater Chem*, vol. 22, no. 13, pp. 5951–5959, Apr. 2012, doi: 10.1039/c2jm15665b.

[109] A. M. Gómez-Marín and C. I. Sánchez, 'Thermal and mass spectroscopic characterization of a sulphur-containing bacterial melanin from Bacillus subtilis', *J Non Cryst Solids*, vol. 356, no. 31–32, pp. 1576–1580, 2010, doi: 10.1016/j.jnoncrysol.2010.05.054.

[110] J. Ribera *et al.*, 'Scalable Biosynthesis of Melanin by the Basidiomycete Armillaria cepistipes', *J Agric Food Chem*, vol. 67, no. 1, pp. 132–139, Jan. 2019, doi: 10.1021/acs.jafc.8b05071.

[111] K. Shanmuganathan, J. H. Cho, P. Iyer, S. Baranowitz, and C. J. Ellison, 'Thermooxidative stabilization of polymers using natural and synthetic

melanins', *Macromolecules*, vol. 44, no. 24, pp. 9499–9507, Dec. 2011, doi: 10.1021/ma202170n.

[112] B. Tawiah, B. Yu, A. C. Y. Yuen, and B. Fei, 'Facile preparation of uniform polydopamine particles and its application as an environmentally friendly flame retardant for biodegradable polylactic acid', *J Fire Sci*, vol. 38, no. 6, pp. 485–503, Nov. 2020, doi: 10.1177/0734904120932479.

[113] H. Li *et al.*, 'Structure Evolution and Thermoelectric Properties of Carbonized Polydopamine Thin Films', *ACS Appl Mater Interfaces*, vol. 9, no. 8, pp. 6655–6660, Mar. 2017, doi: 10.1021/acsami.6b15601.

[114] E. Coy, I. Iatsunskyi, J. C. Colmenares, Y. Kim, and R. Mrówczyński, 'Polydopamine Films with 2D-like Layered Structure and High Mechanical Resilience', *ACS Appl Mater Interfaces*, vol. 13, no. 19, pp. 23113–23120, May 2021, doi: 10.1021/acsami.1c02483.

[115] Y. Kim and J. Kim, 'Carbonization of polydopamine-coating layers on boron nitride for thermal conductivity enhancement in hybrid polyvinyl alcohol (PVA) composites', *Polymers (Basel)*, vol. 12, no. 6, Jun. 2020, doi: 10.3390/polym12061410.

[116] F. J. Lanyi, N. Wenzke, J. Kaschta, and D. W. Schubert, 'On the Determination of the Enthalpy of Fusion of α-Crystalline Isotactic Polypropylene Using Differential Scanning Calorimetry, X-Ray Diffraction, and Fourier-Transform Infrared Spectroscopy: An Old Story Revisited', *Adv Eng Mater*, vol. 22, no. 9, Sep. 2020, doi: 10.1002/adem.201900796.

[117] Y. Kong and J. N. Hay, 'The enthalpy of fusion and degree of crystallinity of polymers as measured by DSC', *Eur Polym J*, vol. 39, no. 8, pp. 1721–1727, Aug. 2003, doi: 10.1016/S0014-3057(03)00054-5.

[118] P. K. Gallagher, *Handbook of thermal analysis and calorimetry*, vol. 3. 2002.

[119] B. Simonovic *et al.*, 'THERMOGRAVIMETRY AND DIFFERENTIAL SCANNING CALORIMETRY OF NATURAL AND SYNTHETIC MELANINS', *Journal of Thermal Analysis*, vol. 36, pp. 2475–2482, 1990.

[120] X. Yu, H. Fan, Y. Liu, Z. Shi, and Z. Jin, 'Characterization of carbonized polydopamine nanoparticles suggests ordered supramolecular structure of

polydopamine', *Langmuir*, vol. 30, no. 19, pp. 5497–5505, May 2014, doi: 10.1021/la500225v.

[121] Groenewoud W., 'Characterisation of Polymers by Thermal Analysis', Amsterdam, 2001.

[122] I. E. Pralea *et al.*, 'From extraction to advanced analytical methods: The challenges of melanin analysis', *International Journal of Molecular Sciences*, vol. 20, no. 16. MDPI AG, Aug. 02, 2019. doi: 10.3390/ijms20163943.

[123] L. F. Wang and J. W. Rhim, 'Isolation and characterization of melanin from black garlic and sepia ink', *LWT*, vol. 99, pp. 17–23, Jan. 2019, doi: 10.1016/j.lwt.2018.09.033.

[124] C. Marín-Sanhueza, A. Echeverría-Vega, A. Gómez, G. Cabrera-Barjas, R. Romero, and A. Banerjee, 'Stress Dependent Biofilm Formation and Bioactive Melanin Pigment Production by a Thermophilic Bacillus Species from Chilean Hot Spring', *Polymers (Basel)*, vol. 14, no. 4, Feb. 2022, doi: 10.3390/polym14040680.

[125] V. A. E. Barrios, J. R. Rangel Méndez, N. v Pérez Aguilar, G. A. Espinosa, and J. L. Dávila Rodríguez, 'FTIR-An Essential Characterization Technique for Polymeric Materials'. [Online]. Available: www.intechopen.com

[126] J. M. G. Cowie and V. Arrighi, *Polymers: Chemistry and Physics of Modern Materials*, Third edition. Scotland, UK: CRC Press, 2007.

[127] J. C. Markwart, A. Battig, M. M. Velencoso, D. Pollok, B. Schartel, and F. R. Wurm, 'Aromatic vs. aliphatic hyperbranched polyphosphoesters as flame retardants in epoxy resins', *Molecules*, vol. 24, no. 21, 2019, doi: 10.3390/molecules24213901.

[128] T. Wang, M. Xia, and X. Kong, 'The pros and cons of polydopamine-sensitized titanium oxide for the photoreduction of CO2', *Catalysts*, vol. 8, no. 5, 2018, doi: 10.3390/catal8050215.

[129] A. C. Ferrari and J. Robertson, 'Interpretation of Raman spectra of disordered and amorphous carbon', *Physical Review B: Covering condensed matter and materials physics*, pp. 14095–14107, May 2000, doi: https://doi.org/10.1103/PhysRevB.61.14095.

[130] H. Fan *et al.*, ‘Folic acid-polydopamine nanofibers show enhanced ordered-stacking via π-π Interactions’, *Soft Matter*, vol. 11, no. 23, pp. 4621–4629, 2015, doi: 10.1039/c5sm00732a.

[131] J. Liebscher *et al.*, ‘Structure of polydopamine: A never-ending story?’, *Langmuir*, vol. 29, no. 33, pp. 10539–10548, Aug. 2013, doi: 10.1021/la4020288.

[132] P. Delparastan, K. G. Malollari, H. Lee, and P. B. Messersmith, ‘Direct Evidence for the Polymeric Nature of Polydopamine’, *Angewandte Chemie - International Edition*, vol. 58, no. 4, pp. 1077–1082, Jan. 2019, doi: 10.1002/anie.201811763.

[133] H. Regan, ‘Our colorful clothes are killing the environment - CNN Style’, *Asian rivers are turning black. And our colorful closets are to blame*, Sep. 28, 2020. https://www.cnn.com/style/article/dyeing-pollution-fashion-intl-hnk-dst-sept/index.html (accessed Nov. 27, 2022).

[134] B. Lellis, C. Z. Fávaro-Polonio, J. A. Pamphile, and J. C. Polonio, ‘Effects of textile dyes on health and the environment and bioremediation potential of living organisms’, *Biotechnology Research and Innovation*, vol. 3, no. 2, pp. 275–290, Jul. 2019, doi: 10.1016/j.biori.2019.09.001.

[135] W. Xiong, Q. Zhao, X. Li, and L. Wang, ‘Multifunctional Plasmonic Co-Doped Fe2O3@polydopamine-Au for Adsorption, Photocatalysis, and SERS-based Sensing’, *Particle and Particle Systems Characterization*, vol. 33, no. 9, pp. 602–609, Sep. 2016, doi: 10.1002/ppsc.201600085.

[136] Q. U. Ain, U. Rasheed, M. Yaseen, H. Zhang, and Z. Tong, ‘Superior dye degradation and adsorption capability of polydopaminemodified Fe3O4-pillared bentonite composite’, *J Hazard Mater*, vol. 397, no. April, p. 122758, 2020, doi: 10.1016/j.jhazmat.2020.122758.

[137] E. Climent, M. Hecht, and K. Rurack, ‘Loading and release of charged and neutral fluorescent dyes into and from mesoporous materials: A key role for sensing applications’, *Micromachines (Basel)*, vol. 12, no. 3, pp. 1–18, Mar. 2021, doi: 10.3390/mi12030249.

[138] M. Duan *et al.*, ‘Preparation of poly-dopamine-silk fibroin sponge and its dye molecular adsorption’, *Water Science and Technology*, vol. 82, no. 11, pp. 2353–2365, Dec. 2020, doi: 10.2166/wst.2020.502.

[139] W. A. Henderson and C. J. Schultz, ‘The Nucleophilicity of Amines’, *Journal of Organic Chemistry*, vol. 27, no. 12, pp. 4643–4646, Dec. 1962, doi: 10.1021/jo01059a507.

[140] F. Brotzel, C. C. Ying, and H. Mayr, ‘Nucleophilicities of primary and secondary amines in water’, *Journal of Organic Chemistry*, vol. 72, no. 10, pp. 3679–3688, May 2007, doi: 10.1021/jo062586z.

[141] J. E. McGinness, ‘Mobility Gaps: A Mechanism For Band Gaps in Melanins’, *Science (1979)*, vol. 177, no. 4052, pp. 896–897, 1972, [Online]. Available: http://cyber.sci-hub.tw/MTAuMTEyNi9zY2llbmNlLjE3Ny40MDUyLjg5Ng==/10.1126%40science.177.4052.896.pdf

[142] P. R. Crippa, V. Cristofoletti, and N. Romeo, ‘A band model for melanin deduced from optical absorption and photoconductivity experiments’, *BBA - General Subjects*, vol. 538, no. 1, pp. 164–170, 1978, doi: 10.1016/0304-4165(78)90260-X.

[143] G. Han, F. Xu, B. Cheng, Y. Li, J. Yu, and L. Zhang, ‘Enhanced Photocatalytic H_2O_2 Production over Inverse Opal ZnO@ Polydopamine S-scheme Heterojunctions’, *Acta Physico Chimica Sinica*, vol. 0, no. 0, pp. 2112037–0, 2022, doi: 10.3866/pku.whxb202112037.

[144] J. Zhao, J. Chen, Z. Chen, Y. Zhang, D. Xia, and Q. Wang, ‘Flexible cotton fabrics/PDA/BiOBr composite photocatalyst using bioinspired polydopamine as electron transfer mediators for dye degradation and Cr(VI) reduction under visible light’, *Colloids Surf A Physicochem Eng Asp*, vol. 593, no. February, p. 124623, 2020, doi: 10.1016/j.colsurfa.2020.124623.

[145] J. E. de Albuquerque, C. Giacomantonio, A. G. White, and P. Meredith, ‘Study of optical properties of electropolymerized melanin films by photopyroelectric spectroscopy’, *European Biophysics Journal*, vol. 35, no. 3, pp. 190–195, 2006, doi: 10.1007/s00249-005-0020-z.

[146] N. Çelebi, F. Soysal, and K. Salimi, 'Well-defined core/shell pDA@Ni-MOF heterostructures with photostable polydopamine as electron-transfer-template for efficient photoelectrochemical H2 evolution', *Int J Hydrogen Energy*, vol. 47, no. 29, pp. 13828–13837, Apr. 2022, doi: 10.1016/j.ijhydene.2022.02.111.

[147] S. Kim, G. hee Moon, G. Kim, U. Kang, H. Park, and W. Choi, 'TiO2 complexed with dopamine-derived polymers and the visible light photocatalytic activities for water pollutants', *J Catal*, vol. 346, pp. 92–100, 2017, doi: 10.1016/j.jcat.2016.11.027.

[148] U. Pal, 'Use of diffuse reflectance spectroscopy for optical characterization of un-supported nanostructures', *Revista Mexicana de Física*, vol. 53, no. 5, pp. 18–22, 2007.

[149] P. M. Wood, 'The potential diagram for oxygen at pH 7', 1988.

[150] B. Gun Kwon and J. Yoon, 'Superoxide Anion Radical: Principle and Application', 2009.

[151] R. Chen, B. Lin, and R. Luo, 'Recent progress in polydopamine-based composites for the adsorption and degradation of industrial wastewater treatment', *Heliyon*, vol. 8, no. 12. Elsevier Ltd, Dec. 01, 2022. doi: 10.1016/j.heliyon.2022.e12105.

[152] X. Zhou, B. Jin, J. Luo, X. Gu, and S. Zhang, 'Photoreduction preparation of Cu2O@polydopamine nanospheres with enhanced photocatalytic activity under visible light irradiation', *J Solid State Chem*, vol. 254, no. June, pp. 55–61, 2017, doi: 10.1016/j.jssc.2017.07.007.

[153] A. Pullman and B. Pullman, 'The band structure of melanins', *BBA - Biochimica et Biophysica Acta*, vol. 54, no. 2, pp. 384–385, 1961, doi: 10.1016/0006-3002(61)90389-4.

[154] D. S. Galvão and M. J. Caldas, 'Polymerization of 5,6-indolequinone: A view into the band structure of melanins', *J Chem Phys*, vol. 88, no. 6, pp. 4088–4091, 1988, doi: 10.1063/1.453810.

[155] H. Mohammad-Shiri, M. Ghaemi, S. Riahi, and A. Akbari-Sehat, 'Computational and Electrochemical Studies on the Redox Reaction of

Dopamine in Aqueous Solution', 2011. [Online]. Available: www.electrochemsci.org

[156] P. Meredith, B. J. Powell, J. Riesz, S. P. Nighswander-Rempel, M. R. Pederson, and E. G. Moore, 'Towards structure-property-function relationships for eumelanin', *Soft Matter*, vol. 2, no. 1. pp. 37–44, 2006. doi: 10.1039/b511922g.

[157] A. F. Collings and Christa. Critchley, 'Broadband photon-harvesting biomolecules for photovoltaics', in *Artificial photosynthesis: from basic biology to industrial application*, A. Collings and C. Critchley, Eds. Wiley-VCH, 2005, pp. 37–65.

[158] Y. Zou *et al.*, 'Regulating the absorption spectrum of polydopamine', 2020. [Online]. Available: http://advances.sciencemag.org/

[159] A. Alavi, 'A4: Theoretical techniques and ideas', 2006.

[160] M. Fakhrul Ridhwan Samsudin, L. Tau Siang, S. Sufian, R. Bashiri, N. Muti Mohamed, and R. Mahirah Ramli, 'Exploring the role of electron-hole scavengers on optimizing the photocatalytic performance of BiVO4', in *Materials Today: Proceedings*, 2018, vol. 5, no. 10, pp. 21703–21709. doi: 10.1016/j.matpr.2018.07.022.

[161] B. Abramovic, V. Despotovic, D. Šojic, and N. Fincur, 'Mechanism of clomazone photocatalytic degradation: Hydroxyl radical, electron and hole scavengers', *Reaction Kinetics, Mechanisms and Catalysis*, vol. 115, no. 1, pp. 67–79, Jun. 2015, doi: 10.1007/s11144-014-0814-z.

[162] R. Overend and G. Paraskevopoulos, 'Rates of OH radical reactions. 4. Reactions with methanol, ethanol, 1-propanol, and 2-propanol at 296 K', *Journal of Physical Chemistry*, vol. 82, no. 12, pp. 1329–1333, 1978, doi: 10.1021/j100501a001.

[163] Y. Li *et al.*, 'Structure and Function of Iron-Loaded Synthetic Melanin', *ACS Nano*, vol. 10, no. 11, pp. 10186–10194, Nov. 2016, doi: 10.1021/acsnano.6b05502.

[164] V. Ball *et al.*, 'The reduction of Ag + in metallic silver on pseudomelanin films allows for antibacterial activity but does not imply unpaired electrons', *J Colloid*

Interface Sci, vol. 364, no. 2, pp. 359–365, Dec. 2011, doi: 10.1016/j.jcis.2011.08.038.

[165] K. Hamamoto, H. Kawakita, K. Ohto, and K. Inoue, ‘Polymerization of phenol derivatives by the reduction of gold ions to gold metal’, *React Funct Polym*, vol. 69, no. 9, pp. 694–697, Sep. 2009, doi: 10.1016/j.reactfunctpolym.2009.05.003.

[166] H. W. Chien, W. H. Kuo, M. J. Wang, S. W. Tsai, and W. B. Tsai, ‘Tunable micropatterned substrates based on poly(dopamine) deposition via microcontact printing’, *Langmuir*, vol. 28, no. 13, pp. 5775–5782, Apr. 2012, doi: 10.1021/la300147p.

[167] A. B. Jasso-Salcedo, G. Palestino, and V. A. Escobar-Barrios, ‘Effect of Ag, pH, and time on the preparation of Ag-functionalized zinc oxide nanoagglomerates as photocatalysts’, *J Catal*, vol. 318, pp. 170–178, 2014, doi: 10.1016/j.jcat.2014.06.008.

[168] A. M. Awwad, N. M. Salem, and A. O. Abdeen, ‘Green synthesis of silver nanoparticles using carob leaf extract and its antibacterial activity’, *International Journal of Industrial Chemistry*, vol. 4, no. 1, p. 29, 2013, doi: 10.1186/2228-5547-4-29.